Title
Application of Proprioception Quasi-Direct Drive Actuators on Dynamic Robotic Systems

Author
Zhang, Xiaoguang

Publication Date
2019

UNIVERSITY OF CALIFORNIA

Los Angeles

Application of Proprioception Quasi-Direct Drive Actuators on Dynamic Robotic Systems

A dissertation submitted in partial satisfaction

of the requirements for the degree

Doctor of Philosophy in Mechanical Engineering

by

Xiaoguang Zhang

2019

ABSTRACT OF THE DISSERTATION

Application of Proprioception Quasi-Direct Drive Actuators on Dynamic Robotic Systems

by

Xiaoguang Zhang

Doctor of Philosophy in Mechanical Engineering

University of California, Los Angeles, 2019

Professor Dennis W. Hong, Chair

The properties of actuation is absolutely the basic and foundation among all factors that determine the overall performance of a system, and this has been true for all living creatures, and other machines as well. Ever since the first industry robot being invented half a century ago, the robotics field have been developed rapidly, and all sorts of robots are playing more and more important roles in all human production and daily life activities.

The main requirements for robots have been focused on rigidity, high torque and precision motion until recently, as traditionally the major application of robots are along factory production lines, with their working environment well known and controlled, performing jobs that are highly repetitive. To ensure the consistency of production, rigid robots that provides precise motion with high payload capacity are preferred. Thus, position controlled high torque servos have been dominating the industry. These actuators are also combined with force/torque sensors to enable force control capability on robotic systems, but due to

various limitations of such setup, it is difficult to realize dynamic motions where impulsive loading is frequently recurrent. During the recent decade, research efforts in the robotics field have been made in the development of Series Elastic Actuators (SEA), seeking for alternative actuation solutions to meet the requirements for dynamic robotic systems. Although there are a hand full of successful cases, the complicity and difficulty down the route is quite obvious. Besides, the respond bandwidth of any SEA is strictly limited by the property of its elastic component, resulting in customization that is very application specific.

The recent rapid development of Proprioceptive Actuators, also know as Quasi-Direct Drive Actuators (or QDD for abbreviation), provides a simple actuation solution that not only features torque control capability, but also provides a very wide response bandwidth as well as inherent compliance. Thus its application on various robotic systems is definitely intriguing and worth of exploration.

The work presented in this dissertation involves the development and discussion of the application of Proprioceptive Actuators on several different dynamic robotic systems, including a three-finger robotic hand called DAnTE, a non-anthropomorphic bipedal robot called NABi-2 and a quadruped robot with very unique kinematics configuration, called ALPHRED-2. Underactuated anthropomorphic fingers are developed and applied on DAnTE, and a potential energy flow theory is developed to assist the development of the mechanical intelligence in these underactuated fingers to realize gesture dexterity. Along with the application of Proprioceptive Actuators on legged robots, an Impact Transfer Factor theory is proposed to quantify the response of a robotic limb to a impact in terms of impact sensing from a whole-system point of view. As outlook of the presented work, an upgraded version

of DAnTE as well as an open source kid-size humanoid robot platform are introduced. Both systems are driven by well-packaged Proprioceptive Actuator modules and are expected to possess dexterous force control and high dynamic performance capabilities, and both of them are designed to serve as reliable robot platforms to carry further research in related topics.

The dissertation of Xiaoguang Zhang is approved.

Jonathan B. Hopkins

Veronica Santos

Xiaochun Li

Dennis W. Hong, Committee Chair

University of California, Los Angeles

2019

To my grandfather . . .

who inspired and encouraged

my curiosity and passion in mechanisms

throughout my childhood

Table of Contents

List of Figures

List of Tables

PREFACE

First of all, I'd like to sincerely thank my adviser, Dr. Dennis Hong, for his attentive guidance and generous support throughout my entire Ph.D. career. He has been an wise mentor in research as well as a true friend in life. I have been and will always appreciate the opportunity to join RoMeLa and become one of the big family. I have been and will always be proud of it. RoMeLa has always been my wonderland and I enjoyed every minute spent here.

I'd also like to thank my Committee members, Dr. Jonathan Hopkins, Dr. Xiaochun Li and Dr. Veronica Santos for their wisdom and support, as well as all the amazing knowledge I've learned from them.

Special thanks go to all my lab mates for their help and companion, for all the projects we have worked on together and for all the fun we had. I especially want to thank Joshua Hooks, Jeffery Yu, Min Sung Ahn, and Taoyuanmin Zhu for all the journeys and adventure we had together.

I'd also like to thank Shengxin Jia for being a wonderful friend during the past 5 years.

Finally, I'd like to thank my family for their love, patience and endless support. Thanks to my father who encouraged me to go abroad since I was in high school as well as my mother who supports all my choices and decisions, I was then able to knock open the gate of a Ph.D. career. And without the support from my family, I could never finish it. I wish to thank Min Wang, who became my girlfriend back in 2014 when I entered graduate school and then became my wife recently in the summer of 2019. She has always been a great companion

for my life and supportive for my career. I also wish to thank my little one to-be, who is definitely a gift to me.

I acknowledge that the work presented in Section.4.2.1 and Section.3.2.1 contains a version of [74], and my co-authors contributed to the actuator driver and system control algorithms. The project was partially supported by the ONR through grant N00014-15-1-2064. I also acknowledge that the work presented in Section.4.3.1 contains partially a version of [72], and the project was supported by the ONR through grant N00014-15-1-2064, and Section.4.3.2 contains partially a version of [30](submitted), and the projects were supported by a grant (code R2016001) from Gyeonggi Technology Development Program Funded by Gyeonggi Province as well as the ONR through grant N00014-15-1-2064. The co-authors in both papers contributed to the control of the robot. Work presented in Section.3.3.3 contains a version of [67](submitted), and my co-authors contributed in the simulation and experiments. This work is also supported by ONR through grant N00014-15-1-2064.

Curriculum Vitae

2010 – 2014	B.S. in Mechanical Engineering, University of Science and Technology of China (USTC), Hefei, China.
2014 – Present	Ph.D. student in Mechanical Engineering, University of California, Los Angeles (UCLA).

Publications

Zhang, Xiaoguang, Jinhong Hu, Shixin Mao, Erbao Dong, and Jie Yang. “Design and property analysis of a hybrid linear actuator based on shape memory alloy.” Smart Materials and Structures 23, no. 12 (2014): 125004.

Zhang, Xiaoguang, Yi Zeng, and Dennis Hong. ”A novel and efficient compact propulsion mechanism with high response speed for robotic applications.” In 2016 13th International Conference on Ubiquitous Robots and Ambient Intelligence (URAI), pp. 314-320.

Zhang, Xiaoguang, and Dennis W. Hong. ”Micro Power Multiplexer, a Compact Device That Controls Mechanical Power Flow.” In ASME 2017 International Design Engineering Technical Conferences and Computers and Information in Engineering Conference.

Yu, Jeffrey, Joshua Hooks, Xiaoguang Zhang, Min Sung Ahn, and Dennis Hong. ”A proprioceptive, force-controlled, non-anthropomorphic biped for dynamic locomotion.” In 2018

IEEE-RAS 18th International Conference on Humanoid Robots (Humanoids), pp. 1-9.

Zhang, Xiaoguang, Taoyuanmin Zhu, Itsui Yamayoshi, and Dennis Hong. ”A Force Controlled Under Actuated Robotic Hand with Mechanical Intelligence and Proprioceptive Compliant Actuation.” In 2018 IEEE-RAS 18th International Conference on Humanoid Robots (Humanoids), pp. 1-8.

Xiaoguang Zhang, Taoyuanmin Zhu, Isui Yamayoshi and Dennis Hong. ”Dexterity, Sensitivity And Versatility: An Under Actuated Robotic Hand With Mechanical Intelligence And Proprioceptive Actuation.” Accepted by Iternational Journal of Humanoid Robotics(IJHR) on Dec. 3, 2019.

Xiaoguang Zhang, Min Sung Ahn, Taoyuanmin Zhu, and Dennis Hong. ”Impact Transfer Factors: An Approach to Quantitatively Analyze Impacts for Dynamic Robotic Systems.”(Under review). Submitted to 2020 IEEE International Conference on Robotics and Automation.

Joshua Hooks, Min Sung Ahn, Jeffrey Yu, Xiaoguang Zhang, Taoyuanmin Zhu, Hosik Chae, and Dennis Hong. ”ALPHRED: A Multi-Modal Operations Quadruped Robot for Package Delivery Applications.”(Under review). Submitted to 2020 IEEE International Conference on Robotics and Automation.

CHAPTER 1

Introduction

1.1 Background and Motivation

Traditionally the operating environment of robots is separated from human with very clear boundaries. However, with the rapid development of robotics technology during the past decades, these boundaries are fading and getting blurrier. With the advancement in the quality of the design and fabrication quality of robotic components, control theories, sensors, computers and artificial intelligence, robots are entering the world that humans work and live. It is gradually happening that robots are expected to not just free human workers from heavy-load, repetitive works, but also become co-workers or assistant in complicated jobs or even provide service in people's daily life, examples being co-bots, delivery robots and vacuum robots. In another word, robots are no longer kept in precisely controller environment and start to interact with the real world which is an unknown environment always full of changes and uncertainty.

At the same time, robots are now expected to provide better dynamic performance thus to become capable of handling various jobs efficiently. Despite how challenging it is, frequent and repetitive impact loading becomes inherent to the tasks robots nowadays are expected to carry out. Traditional solutions as force/torque sensors combined with position control servo actuators comprising of high speed motor and high gear ratio transmission. However, they can not meet such impact bearing and mitigation requirements since neither the force/toque sensors or the transmission can survive impacts and dynamic loading with frequent substantial changes. To overcome this issue, elastic components are integrated into the traditional servo actuators providing mechanical compliance, thus Series Elastic Actuators (SEA) have been developed. Yet SEA is not a perfect solution despite its capability of handling impacts to a certain degree. Due to the natural frequency and deformation limitation of the applied elastic component, the response bandwidth of an SEA is limited to a very narrow range. It also makes it hard to achieve a fine control of the SEA because of the difficulty in creating accurate models of the actuator. Besides, the difficulty of fabrication and the high cost of SEA modules also made non-negligible negative contributed.

The recent burst of development on Proprioceptive Quasi-Direct Drive Actuators provides a great solution to dynamic robotic systems. The rapid development of the drone industry makes a variety of selections on high torque BLDC motors commercially available. Proprioceptive Quasi-Direct Drive Actuators (also called Proprioceptive Actuators or Quasi-Direct Drive Actuators), are built by simply combining such high torque BLDC motors with a low gear ratio transmission. Featuring high actuation transparency, accurate and reliable force control capability can be achieved by current sensing, thus no external force/torque sensors are needed.

Proprioceptive Quasi-Direct Drive Actuators open up a new approach to dynamic robotic solutions. The high actuation transparency and compliance inherent to these actuators is unprecedented and so are some new features on the robots that the actuators are applied to. Thus, the application of this new type of actuator on dynamic robotic systems is very worth of deep exploration.

With a firm belief in worthy new discoveries and knowledge to generate around the application of Proprioceptive Quasi-Direct Drive Actuators, the work presented in this dissertation is dedicated in exploring the application of this type of actuator on various dynamic robotic systems. Several basic mechanical concepts are revisited and some new theories and extension of current theories are created to help with understanding and better assist the application development.

1.2 Research Objective

The objectives of this research is to explore the application of Proprioceptive Quasi-Direct Drive Actuators in various types of dynamic robotic systems. Thus, contribution in this research involve development in both theories and physical systems.

Instead of focused on a very specific issue or topic, the work in this research covers various different yet tightly related topics, as it appears to be necessary in order to comprehensively study the application of Proprioceptive Actuators. The application of the actuators are mainly explored in compact and small systems using a robotic hand as experimental example and in various dynamic legged robots.

As part of the theoretical study, The physical and electrical characteristics of Proprioceptive Actuators are derived from those of normal BLDC motors. The reflective inertia of gear trains as well as planetary setup is reviewed to reveal the basic guidelines to the actuation transparency of this type of actuators. To better understand and implement underactuated mechanism with embedded mechanical intelligence, further apply it onto a compact robotic hand, a potential energy flow theory that can be used to explain mechanical intelligence in underactuated mechanisms has been developed. Meanwhile, as impacts are inherent to the tasks that the robots actuated with Proprioceptive Actuators are supposed to carry out, an Impact Transfer Factor theory has been developed to fill the gaps that current theories on impacts have not covered. With the help of the Impact Transfer Factor theory, one can easily analyze or predict the response of a robotic system upon impacts from a system level point of view. The robot join configuration and actuation chain configuration as the basic to a robot design is also reviewed, with evaluation and conclusion specifically made for applications with Proprioceptive Actuators.

The robotic systems developed during the research includes a robotic hand called DAnTE-1(Dynamic Anthropomorphic Tactile End-effector, version 1), a non-anthropomorphic bipedal robot NABi-2, and a quadrupedal robot called ALPHRED-2 (Autonomous Legged Personal Helper Robot with Enhanced Dynamics version 2). All these systems are actuated by the Proprioceptive Actuators called BEAR, Backdrivable Electromagnetic Actuators for Robots, and there are two sizes of BEAR developed, with distinguished capabilities covering different ranges of applications. DAnTE is an experimental system to explore the application of Proprioceptive Actuators onto a compact and dynamic robotic hand with outstanding dexterity and force control capability, with the implementation of mechanical intelligence under the guidance of the Potential Energy Flow theory for underactuated mechanisms. NABi-2 and

ALPHRED-2 are developed to experiment the application of Proprioceptive Actuators in fully actuated dynamic legged robots. The theories are applied to guide the development of the systems, while the experimental results support, validate and improve the development of the theories.

On top of all above, the experimental prototype system DAnTE-1 is upgraded into a more mutual and reliable version called DAnTE-2. With experience and lessons learned from NABi-2 and ALPHRED-2, a new kid-size humanoid legged robot platform that is supposed to be dynamic, robust, reliable and optimal in performance is also proposed. These two new platforms are meant to efficiently help the current researchers with further exploration in various other topics related to the operation of dynamic robots.

1.3 Document Organization

This dissertation discusses the implementations of Proprioceptive Actuators in several different dynamic robotic systems, along with a couple of theoretical innovation and contribution to the robotics subject in relation with such implementations. The document is organized as follows:

In Chapter.2, the background of actuators previously and currently used on various robotic systems are reviewed, with a focus on electromagnetic actuators, which are the current major solutions in the field of robotics. As the basic setup, position controlled actuators are reviewed first, followed by Series Elastic Actuators. And the Proprioceptive Actuators are introduced as last. For each type of actuator, its basic concept is explained in detail, and the pros and cons are listed for comparison. Existing representative examples of each type are also briefly mentioned.

The theoretical development is covered in Chapter.3, starting with reviewing the properties and characteristics of BLDC motors to derive those of Proprioceptive Actuators. The reflective inertia of plain geartrain as well as planetary gear set is also reviewed in the chapter, as it directly influence the actuation transparency of a actuator, which is the main benefit of Proprioceptive Quasi-Direct Drive Actuators. In compact robotic systems, underactuated mechanisms are often adopt to reduce the size, weight and complexity of the system, such as robotic hands, soft robots and tendon driven robots. To better assist the implementation of mechanical intelligence in underactuated robotic systems, a Potential Energy Flow theory is introduced in section.3.2.1. In the last section of Chapter.3, the response of a robotic system to impacts is reviewed, as well as an Impact Mitigation Factor theory provided by other researchers to quantify the mitigation capability of Proprioceptive Actuators and the robotic system that utilize such actuators. Then an Impact Transfer Factor theory developed during the work covered in this dissertation is illustrated. The theory is meant to cover the gap that other theories did not consider, and it provides some evaluation matrices to quantify impact sensitivity of any robotic system.

In Chapter.4, the physical robotic systems developed are presented. Sections go through from a robotic hand system DAnTE-1 and its updated version DAnTE-2, to legged robot platforms including an non-anthropomorphic bipedal robot NABi-2, a quadruped robot ALPHRED-3 and the lower body platform of a kid-sized humanoid robot called BRUCE. The design of each system is illustrated in detail followed by their performance presentation as experimental results.

In the last Chapter, the conclusion of the dissertation is provided. The contribution from the theories generated in this work is summarized, with outlook for their potential use cases in the future development of related topics. The actuators and physical robotic systems developed are reviewed, with their performance, capability and potential impacts that they can bring to the robotics field evaluated.

CHAPTER 2

Background of Actuators

Actuators are one of the most critical core components determining the performance of an actuated system, and this is true for robots and all other actuated systems including the amazing creatures of the great nature. Thus research and development of actuators have always been the hot topic since robotics first came into shape. And as nowadays robotic systems become more and more dynamic in performance, the demands on actuators also become more comprehensive. Thus for modern robotic systems, although the power and power-weight ratio has been always the major characteristics when evaluating an actuator, nevertheless, control accuracy, speed, impact resistance and response bandwidth are equally critical.

Classified by actuation power source, there are generally three categories of actuators used on robotic systems: hydraulic, pneumatic, and electronic.

For every hydraulic actuated system, there will be a hydraulic pressure pump providing pressurized hydraulic fluid, and the pump can be either on board or, as it often times is, located externally. Pressured hydraulic fluid is then feed into hydraulic actuators which consist of cylinder or fluid motor that uses hydraulic power to facilitate mechanical operation. The mechanical motion gives an output in terms of linear, rotatory or oscillatory motion.

Figure 2.1: The first industrial robot, Unimate

For robotics application in particular, relatively low speed but high force output is needed, and in most cases the joints do not need a full revolution. Thus, almost all application of hydraulic actuators on robots are linear hydraulic actuators that are basically pistons and cylinders. One compelling reason to use hydraulics, especially for high degree-of-freedom machines, is the relative ease of adding high force degrees of freedom. For an electric motor driven robots, each actuator needs to be sized for its peak performance, which makes building systems with many degrees of freedom needing high peak power and force at all the joints (and especially at distal joints) very challenging. With a hydraulic system, it is easier to build high force distal links (ankles, wrists, fingers, etc) without adding significant mass and inertia to the limbs. As liquids are nearly impossible to compress, a hydraulic actuator can exert a large force, thus actuators tend to have high force density. Since impact loads are distributed over the large surface area of the hydraulic channels, rather than, for example several small gear teeth, hydraulic actuators also posses high robustness to impacts.

The first industrial robot[47] was created by George Devol and Joseph Engelberger. It was driven by hydraulic actuator and weights about 2 tons. Ever since then hydraulic actuators have become much lighter and efficient, and have been favored by stationary robotic systems, especially industrial robotic arms. The hydraulic legged robots from Boston Dynamics[52], starting with Big Dog, have set the standard for the performance capabilities of modern legged robots. However, hydraulic actuators tend to have poor efficiency, from viscous losses in the moving fluid, servo valve internal leakage and pressure drop[44]. Another key drawback of this approach is its limited acceleration, which is in significant conflict with the demand for dynamic limb motions. Thus for mobile robots where the pressure pump has to be carried on board, hydraulic actuators appears to be less advantageous, especially for robotic systems with high force, high power, low inertia limbs design such that the actuators are all located close to each other.

Pneumatic systems share many points in common with hydraulic systems, in both mechanical concept and system architecture, but instead of fluid, compressed air was used. However, pneumatic systems overcome almost all of those drawbacks of hydraulic systems. Although there might be some servo valve internal leakage and pressure drop that can cause some loss in efficiency, there is no viscous loss at all. What's more, since compressed air has little mass, the acceleration of pneumatic systems is very high in general. Since air is very easy to compress, pneumatic actuators are excellent in impact resistance but this also lead to the major downside-they are only suitable for low force applications, which makes it very unsuitable for mobile dynamic robots. Pneumatic actuators are currently widely used on industrial end-effectors like two finger grippers (2.2a) or soft robot hand (2.2b). Robotic hands

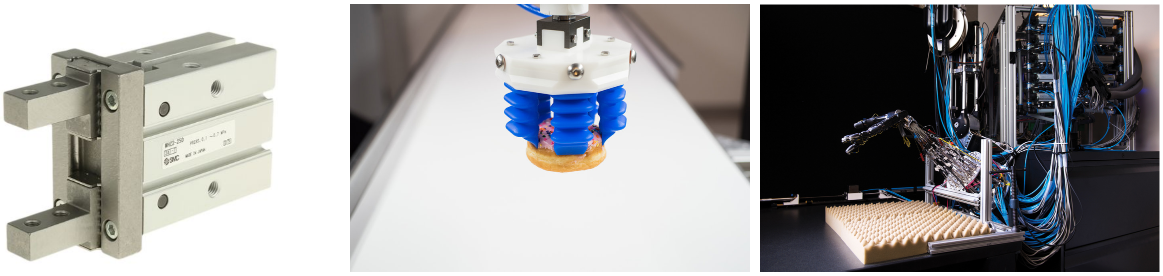

(a) (b) (c)

Figure 2.2: Pneumatic actuators are currently widely used on industrial end-effectors like two finger grippers (2.2a) or soft robot hand (2.2b). Robotic hands with high DoF like the ADROIT ROBOT HAND[34](2.2c) also uses pneumatic systems.

with high DoF like the ADROIT ROBOT HAND[34](2.2c) also uses pneumatic systems.

As discussed above, neither hydraulic or pneumatic actuation systems is a good choice for mobile or portable dynamic robotic systems, like legged robots or dexterous robot hands. Electric actuators however, with their high modularity and relatively balanced characteristics, appear to be better choices. Development of Series Elastic Actuators and Proprioceptive Quasi-Direct Drive Actuators in the recent decades have even further mined the potential of electric actuators, which will be discussed in the following sections.

2.1 Position Controlled Actuators

Position controlled actuators are by far the most widely used actuators on all sorts of different robotic systems, for their robustness, reliability modularity and being relatively easy to control and use. Depending on how the actuator is driven and how the control loop is closed, there are mainly two categories of position controlled actuators that are traditionally used in the field of robotics, which are the stepper motors and the servomotors.

2.1.1 Stepper Motors

A stepper motor, also known as step motor or stepping motor, is a brushless DC electric motor that divides a full rotation into a number of equal steps. The motor's position can then be commanded to move and hold at one of these steps without any position sensor for feedback, as long as the motor is carefully sized to the application in respect to torque and speed. Stepper motors are controlled by open-loop controllers. They effectively have multiple ”toothed” electromagnets arranged around a central gear-shaped piece of iron, and the electromagnets are energized by an external driver circuit or a micro controller. To make the motor shaft turn, first, one electromagnet is given power, which magnetically attracts the gear's teeth. When the gear's teeth are aligned to the first electromagnet, they are slightly offset from the next electromagnet. This means that when the next electromagnet is turned on and the first is turned off, the gear rotates slightly to align with the next one. From there the process is repeated. Each of those rotations is called a ”step”, with an integer number of steps making a full rotation. In that way, the motor can be turned by a precise angle.

However, due to the way that stepper motors function, although precise, the output position has to be increments of the angle that a step produces. The output torque and speed of stepper motors are very limited, thus they must be carefully sized to the application in respect to torque and speed, otherwise either the demanded output speed can never be provided, or a stepper motor may miss steps or even stall when the load exceeds the capacity of the motor, resulting in defective output position. Neither are stepper motors impact-resist, as impulsive loads would likely cause the motor to miss steps. Sometimes stepper motors are combined with transmission mechanisms with a reduction, like gearboxes or lead-screw mechanisms. As the output speed is reduced, the maximum output torque (or force in linear motion) is increased. When a stepper motor is combined with a reduction transmission mechanism, the torque/force density of the actuator is increased, but is then only suitable for application with very low speed, where there is no dynamic motions. And stepper motor torque generally decreases rapidly as speed increases,(Fig.2.3) due to cogging torque[37] and other losses.[12] This inverse relationship between speed and torque means it's only practical to increase speed by a certain amount before the motor is unable to deliver the required torque, even when multiplied by the reduction ratio.

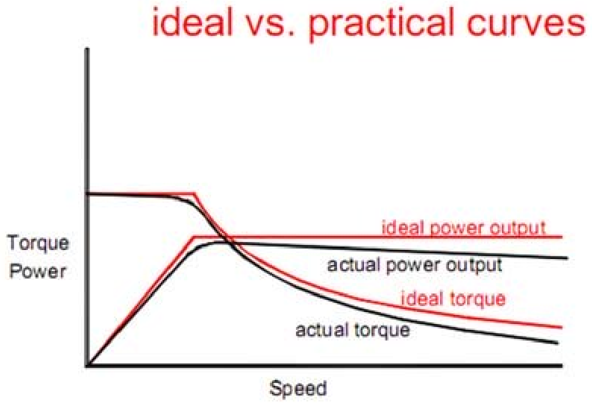

Figure 2.3: Cogging torque reduces the ideal torque (and power) that the motor could produce, with the effect becoming larger as speed increases.

Stepper motors are not suitable for dynamic robotic systems but applications where low speed high torque motion is needed, or where precise position control needs to be achieved with relatively simple control system like an open-loop system. Stepper motors can also provide high holding torque. Besides, they are also cheaper than other type of actuators. Thus, stepper motors can be seen on some small industrial robotic systems or planner machine platforms like CNC milling machines.

2.1.2 Servomotors

Although they are all position controlled actuators and the electromagnetic principle for the motors to be moving seems to be the same, servomotors are very different from stepper motors. A servomotor contains three components: a motor, a position sensor that couples with the motor and a transmission mechanism. The motor can be an AC motor, a brushed DC motor or a brushless DC motor, generating high speed rotary motion. The position sensor, called an encoder, is coupled with the motor shaft for position feedback. Finally the transmission mechanism transforms the high speed rotary motion from the motor to a rotary output with lower speed but higher torque or a linear motion output, depending on the form of the transmission mechanism applied to the servomotor.

The simplest servomotor uses position-only sensing via a potentiometer. The measured position of the output is compared to the command position, which is the external input to the controller. An error signal is generated which then causes the motor to rotate in either direction, as needed to bring the output shaft to the appropriate position. As the positions approach, the error signal reduces to zero and the motor stops. This type of servomotor is not widely used in industrial motion control, but it forms the basis of the simple and cheap servos used for radio-controlled models. On more sophisticated servomotors, optical or magnetic rotary encoders with high resolution are used to measure not only the position but also the speed and acceleration of the output shaft, and the motor speed is controlled by a variable-speed drive. With a PID control algorithm, the servomotor can be brought to its commanded position more quickly and more precisely, with less overshooting.

The type of motor is not critical to a servomotor and different types may be used. At the simplest, brushed permanent magnet DC motors are used, owing to their simplicity and low cost. Small servomotors for research and industrial applications are typically brushless DC motors. For large industrial servomotors, AC induction motors or brushless AC motors are typically used, often with variable frequency drives to allow control of their speed. Drive modules for servomotors are mostly standard component, such as a branch of power electronics based on a three-phase MOSFET or IGBT H bridge. They may also include over-temperature monitoring, over-torque and stall detection features. As the encoder type, gearhead ratio and overall system dynamics are application specific, it is more difficult to produce the overall controller as an off-the-shelf module and so these are often implemented as part of the main controller, integrated into the whole servomotor package.

Servomotors are generally used as a high-performance alternative to the stepper motor. Stepper motors have some inherent ability to control position, as they have built-in output steps. This often allows them to be used as an open-loop position control, without any feedback encoder, as their drive signal specifies the number of steps of movement to rotate, but for this the controller needs to 'know' the position of the stepper motor on power up. Therefore, on first power up, the controller will have to activate the stepper motor and turn it to a known position, e.g. until it activates an end limit switch. The lack of feedback of a stepper motor limits its performance, as the stepper motor can only drive a load that is well within its capacity, otherwise missed steps under load may lead to positioning errors and the system may have to be restarted or recalibrated. The encoder and controller of a servomotor are an additional cost, but they optimise the performance of the overall system (for all of speed, power and accuracy) relative to the capacity of the basic motor.

Servomotors have been dominating in robotics applications as when well designed, servomotors can provide reliable output with adequate speed, torque and accuracy. They are also relatively robust and power efficient. Various of servomotors have been developed and they covers a wide range of applications. Most of current industrial robots use servomotors in their joints and sometimes force/torque sensors are coupled with servomotors to achieve force controlled systems. Servomotor modules covering a wide range of performance requirements are also commercially available2.4, which makes it easier to develop robotic systems with servomotors.

Figure 2.4: Dynamixel servo actuators from Robotis covers a wide range of robotics application.

Servomotors can satisfy some basic dynamic motion requirements when applied on small robotic systems due to scaling effect. Two very good examples are DARwIn (Fig.2.5a)[22] and Nao (Fig.2.5b)[20]. On these small robotics systems, the servomotors are robust enough

(a) DARwIn-OP (b) NAO (c) THOR-RD

Figure 2.5: Humanoid robots with position control servo actuators

to impacts generated when the robots are interacting with the environment or even falling down to the ground. The servomotors are powerful enough for such small systems to perform some basic motions in a dynamic manner, such as walking. However, the torque demand on the joints increases exponentially as the size of the robot gets bigger. To provide enough torque, but still maintain relatively low in weight and small in size, larger gearboxes with bigger reduction ratios are used in the servomotors. Though theses servomotors can provide high enough torque, the output speed is sacrificed. Traditionally the motions of the robotic systems using these servomotors are considered quasi-static, such as a full-size humanoid robot like THOR (Fig.2.5c).[68]

Besides the increased requirement for torque, the difficulty also involves the fact that control algorithms based on only position and velocity does not work as well as they do on smaller systems, as the inertia of the robot limbs can no longer be ignored, and force feedback becomes critical. In many systems, especially industrial robot arms, force/torque sensors are coupled with servomotors on the joints, closing the loop with torque feedback from the joints.

With the help of a good model estimation of the physical system, a decent control algorithm can yield reliable and smooth dynamic motions. However, this is extremely hard with legged robots since the environment that the robot is dealing with is far more complicated than that the industrial robotic arms are, as the latter ones are doing repeated motions in controlled and well-know environment. Despite the fact that force/torque sensors are very expensive in most cases, neither the gearbox of a servomotor or the force/torque sensor is robust enough to resist the impulsive loads that large legged robots and other robotic systems with high dynamic motions often have on their joints, not to mention the impact caused by robot falling down to the ground.

2.2 Series Elastic Actuators

2.2.0.1 Basic Concept And Principle Design

Series Elastic Actuator(SEA) is developed to overcome the disadvantages of the setup with a servomotor and a force/torque sensor (Fig.2.6a), and enhance the dynamics of robotic systems. SEA takes a conventional highly-geared servomotor, and add a spring and spring displacement sensors at the output, as shown in Figure.2.6b Output torque or force can be monitored and controlled by measuring and controlling the amount of spring deflection. In addition to allowing closed-loop output torque control, the spring serves to decouple the gearbox from impacts seen at the output of the actuator. This allows high gear ratios to be used without the risk of damaging the gears upon impact. This feature is perhaps even more importantly than close-loop force/torque control capability for dynamic applications where

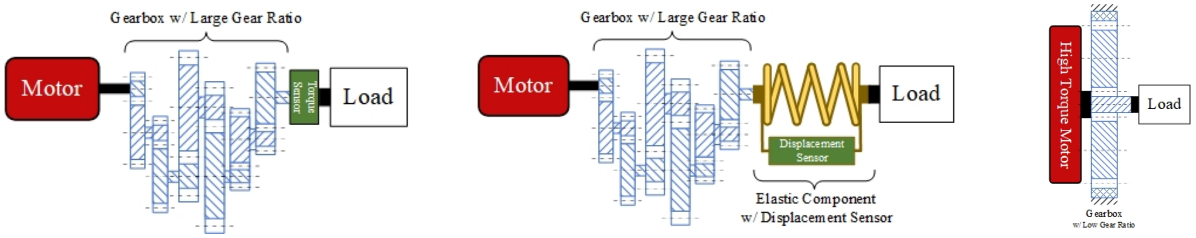

(a) (b) (c)

Figure 2.6: Schematic drawings of different actuators

impulsive loads are inherent.

The spring, or more precisely, the elastic member in an SEA, can be either a conventional metal spring or other elastic component made out of certain elastic material like rubber. Torsional and linear springs are widely applied on SEA actuators, but the SEA modules developed by RoMeLa and used on humanoid bipedal robot platform THOR and SAFFiR as well as the bipedal robot ATRIAS developed by the Oregon State University Dynamic Robotics Laboratory use carbon fiber plates as the elastic members; while some other modules such as those developed by Biorobotics Lab of CMU use a nonlinear rubber piece as the elastic component.

The output of an SEA can be in either linear or rotational form, and the elastic member can also be in either linear or rotational correspondingly, depending on the specific application of the SEA. Linear SEA are mostly seen on legged robots, where biomimetic designs are adopted, such as THOR and Mercury, while on robotic manipulators and SEA modules that are designed for general purpose, rotational design is more favorable for better versatility and compactness, such as the recently announced xMate co-bot arms by Rokae and the SEA modules from ANYBotics and HEBI.

In some SEA implementations, the spring serves to store significant energy, increasing the peak power output of the actuator when the spring and electric motor do work in the same direction. Spring deflection control turns the torque control problem into a position control problem, so SEAs often use expensive, low-backlash, high accuracy transmissions like harmonic drives. And because of transmission backlash and compliance, many SEA implementations use three position sensors: One at the electric motor for commutation; one after the transmission, on the input of the spring; and one on the output of the spring. The addition of a spring and two additional position sensors substantially increases both the mechanical complexity and the cost of the actuator, and sacrifices weight and volume of the actuator to non-power and torque producing components.

2.2.0.2 Representative Modular SEAs

Perhaps the best examples of SEA application in legged robots are the quadruped robot StarlETH[28], and its successor, ANYMal[29], from the Robotic Systems Lab at ETH Zurich. The modular actuator used on ANYMal is ANYdrive, also developed by ETH Zurich, commercialized by ANYbotics. While impressive work has been done on these robots in terms of control of quadruped locomotion, planning, and navigation, the work on getting an accurate model of the actuator and the robot system is tremendous.

Modular SEAs developed by researchers at CMU and commercialized by HEBI robotics are also getting more public attention. These SEAs uses nonlinear rotational elastic members, and the whole module is well packaged in both mechanical and software aspects, making it very easy to be integrated onto a robotic system.

Another outstanding commercially available SEA module is developed by HCRL at UT Austin, commercialized by Apptronik. This SEA is a linear type SEA, with a belt transmission and a combination of ball-screw and linear compression springs. The motor is surrounded by a liquid cooling sleeve to enhance the performance under extreme conditions.

2.3 Proprioceptive Quasi-Direct Drive Actuators

2.3.1 Basic Concept

As mentioned in the previous sections on other type of actuators, despite their advantages, none of them is a good enough choice to drive a robotic limb to perform highly dynamic motions. Even though the traditional position controlled actuators are currently dominating the robotic field, they are not built to take impulsive loading. SEA modules is proven to be a feasible solution, but the limitation on response bandwidth is constitutional to the concept of SEA. Not to mention the difficulty in manufacturing and consistency control as well as the high cost.

Under the demand for cheaper actuator module that can cover a wide bandwidth of dynamic response with outstanding impact mitigation capability, Proprioceptive Quasi-Direct Drive Actuators have been recently developed by researchers in many different robotics subareas all around the world. This new type of actuator is also referred to as Proprioceptive Actuators or Quasi-Direct Drive Actuators (QDD for abbreviation.) The former name expresses its proprioception in torque control and sensing capability, while the latter name comes from its mechanical structure. As preferred, the name Proprioceptive Actuators is adopted to refer to this type of actuator in the following content of this dissertation.

The general concept of Proprioceptive Actuators is pretty straight forward. A schematic drawing of this concept is as shown in Figure.2.6c in comparison with the concept of the combination of a servo motor and a force/torque sensor (Fig.2.6a) and SEA (Fig.2.6b).

The paradigm of Proprioceptive Actuation has had success in low force haptic devices such as the PHANTOM[43], but it was never introduced onto high force applications until recently. With the rapid development of the drone industry, high torque BLDC motors have sprout into the market. By using such high torque motors with a small gear ratio transmission, proprioceptive actuators nowadays can deliver much higher torque. On the other hand, the inertia of Proprioceptive Actuators is significantly much lower than other type of actuators, due to the low gear ratio in the actuator. Advantage being that the actuation transparency of the actuator is inherently excellent, and the response bandwidth it can cover is naturally wider than any other electromagnetic actuator.

2.3.2 Representative Examples

The most famous application of Proprioceptive Actuators is the MIT Cheetah series robots. (Fig.2.7). With the impact mitigating capability, the MIT Cheetah 2 robot can withstand the recurrent impact loading when running at a speed of 13.5m/s.

Proprioceptive Actuators have been very trendy in legged robots, especially after the success of the MIT Cheetah 2. Some of them are already commercially avaliable, such as Laikago and Aliengo from Unitree.

Development of Proprioceptive Actuators have been actively going on in RoMeLa. A

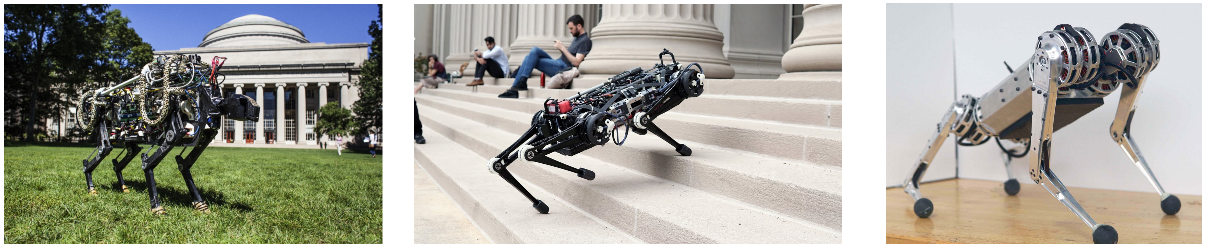

(a) Cheetah 2 (b) Cheetah 3 (c) Mini Cheetah

Figure 2.7: Cheetah series robots developed by MIT Biomimetics Robotics Lab

series of this type of actuators, named BEAR (Backdrivable Electromagnetic Actuator for Robots), have been developed and applied onto multiple robotic systems, such as quadruped robot ALPHRED-2, bipedal robot NABi-2, robotic hand system DAnTE and a small humanoid robot BRUCE. Details of such applications are presented in Chapter.4

CHAPTER 3

Theoretical Development

3.1 Properties of Proprioception Quasi-Direct Drive Actuators

3.1.1 Introduction to BLDC Motors

Brushless DC electric motors (BLDC motor or BL motor) are typically similar to brushed DC permanent magnet synchronous motor in construction, but they are powered by direct current (DC) electricity via an inverter or switching power supply which produces an alternating current (AC) electric current to drive each phase of the motor via a closed loop controller. The controller provides pulses of current to the motor windings that control the speed and torque of the motor.

In brushless DC motors, an electronic servo system replaces the mechanical commutator contacts.[14, 45, 66] An electronic sensor detects the angle of the rotor, and controls semiconductor switches such as transistors which switch current through the windings, either reversing the direction of the current, or in some motors turning it off, at the correct time each 180° shaft rotation so the electromagnets create a torque in one direction. The elimination of the sliding contact allows brushless motors to have less friction and longer life; their working life is only limited by the lifetime of their bearings.

Brushless motors offer several advantages over brushed DC motors, including high torque to weight ratio, better efficiency, increased reliability, reduced noise, longer lifetime (no brush and commutator erosion), elimination of ionizing sparks from the commutator, easy maintenance and overall reduction of electromagnetic interference (EMI). What's more, higher level of electronic control can be applied to BLDC motors. They are also very similar to the construction of stepper motors, thus with the help of a position sensor coupled with the shaft, greater capabilities that are no available with brushed DC motors are allowed. With the help of field-oriented control (FOC, also called vector control), not only the speed and power of the applied BLDC motor system can be controlled, it can also be held at a desired position with controllable finite torque. This is one of the fundamentals that make Proprioceptive Quasi-Direct Drive Actuators possible.

3.1.2 Actuator Characteristics Representation

To better study the characteristics of Proprioceptive Actuators, it is necessary to revisit the basics of the electrical and mechanical characteristics of BLDC motors.

3.1.2.1 Characteristics of BLDC motors

Same as all other electrical motors, the characteristics of BLDC motor are also described with motor constants: the motor velocity constant K_V (or alternatively the back EMF constant denoted as K_e or K_b), the motor torque constant K_T, which can be calculated from the motor velocity constant K_V and the motor size constant K_M.

By Lenz's law, a running motor generates a back-EMF proportional to the speed. Back-

EMF, stands for back electromotive force, more formally known as counter-electromotive force (abbreviated counter EMF or simply CEMF), is the electromotive force or ”voltage” that opposes the change in current which induced it.

Once the motor's rotational velocity is such that the back-EMF is equal to the battery voltage (also called DC line voltage), the motor reaches its limit speed under load-free condition. This is expressed in 3.1

$$E_b = K_\omega \phi \omega \tag{3.1}$$

where E_b is back-EMF and equals to the supply voltage on the wires connected to the coils (SI unit: volt $[V]$). K_ω is a defined constant, ϕ is the filed flux (SI unit: weber $[Wb]$, or in derived units: volt seconds $[V \cdot s]$), and ω is the angular velocity (SI unit: radians per second rad/s).

Since the filed flux ϕ is also a constant with given rotor design, a term K_e (or sometimes denoted as K_b) is further defined as 3.2:

$$K_e = K_\omega \cdot \phi \tag{3.2}$$

K_e represents the back EMF constant or the generic electrical constant, and is often expressed in SI units volt seconds per radian ($V \cdot s/rad$).

$$K_e = \frac{U_{max}}{\omega} \tag{3.3}$$

where U_{max} is the maximum supply voltage on the wires connected to the coils.

The inverse measure of K_e is more frequently used, which may be referred to as the speed constant or the motor velocity constant, denoted as K_V.

K_V is measured in revolutions per minute per volt (RPM/V) or radians per volt second $[rad/(V \cdot s)]$ with the motor at no load condition:

$$K_V = \frac{\omega_{\text{no-load}}}{U_{max}} \tag{3.4}$$

where $\omega_{\text{no-load}}$ is the load-free rotational speed of the motor (SI unit: revolutions per minute $[RPM]$ or radians per second $[rad/s]$). For example, an unloaded motor of $K_V = 1000 RPM/V$ supplied with $11.1V$ will run at a nominal speed of $11100 RPM (1000 RPM/V \times 11.1V)$.

Actually, the motor may not reach this theoretical speed because there are non-linear mechanical losses. On the other hand, if the motor is driven as a generator, the no-load voltage between terminals is perfectly proportional to the RPM and true to the K_V of the motor/generator.

The motor torque constant denoted as K_T is measured as the torque produced divided by armature current and it can be calculated from the motor velocity constant K_v, as follow:

Denote the mechanical power P produced by a motor as:

$$P = UI \tag{3.5}$$

where I is the armature current (SI unit: ampere $[A]$) and U is the "useful" voltage, the applied voltage minus back-EMF voltage (SI unit: volt $[A]$).

P can also be expressed as the production of torque and rotational speed:

$$P = \tau\omega \tag{3.6}$$

where τ is the torque of the motor (SI unit: newton meter $[N \cdot m]$) and ω is the rotational velocity (SI unit: radians per second $[rad/s]$).

While on the other hand, ω can also be expressed with K_V and U, using 3.4:

$$\omega = U \cdot K_V \tag{3.7}$$

Here K_V is in SI unit: radians per volt second $[rad/(V \cdot s)]$ Note that this is true because when the motor is working under load at a steady state, the "useful" voltage is the maximum supplied voltage. And by using 3.5, 3.6 and 3.7, τ can be expressed as:

$$\tau = \frac{P}{\omega} = \frac{P}{U \cdot K_V} = \frac{U \cdot I}{U \cdot K_V} = \frac{I}{K_V} \tag{3.8}$$

As the motor torque constant K_T is defined as:

$$K_T = \frac{I}{\tau} \tag{3.9}$$

the motor torque constant is derived from 3.8 as:

$$\begin{aligned} &K_T = \frac{1}{K_V},\ where\ K_V\ unit\ is\ rad/(V \cdot s) \\ &or \\ &K_T = \frac{60}{2\pi \cdot K_V},\ where\ K_V\ unit\ is\ RPM/s \end{aligned} \tag{3.10}$$

And the SI units for the torque constant K_T are newton metres per ampere $(N \cdot m/A)$.

K_M denotes the motor size constant, and it is sometimes referred to as the motor constant. In SI units, K_M is expressed in newton metres per square root watt ($N \cdot m/\sqrt{W}$):

$$K_M = \frac{\tau}{\sqrt{P_R}} \tag{3.11}$$

where τ is the motor torque SI unit: newton meter $[N \cdot m]$), P_R is the resistive power loss (SI unit: watt$[W]$). The motor size constant only depends on the material and geometry of the stator armature core and is winding independent (as long as the same conductive material is used for wires). For instance, same motor wound with 6 turns using 2 parallel wires instead of 12 turns single wire will double the velocity constant K_V, but K_M remains unchanged. K_M can be used for selecting the size of a motor to use in an application, well K_V can be used for selecting the winding to use in the motor.

By substituting τ in 3.11 using 3.10, the relationship between K_M and K_T can be derived:

$$K_M = \frac{K_T \cdot I}{\sqrt{P_R}} = \frac{K_T \cdot I}{\sqrt{I^2 \cdot R}} = \frac{K_T}{\sqrt{R}} \tag{3.12}$$

where I is the armature current (SI unit: ampere $[A]$) and R is the resistance (SI unit: ohm $[\Omega]$).

To visualize the performance characteristics of BLDC motors, let's take the BLDC motor that is used on small Proprioceptive Quasi-Direct Drive actuator Koala BEAR as introduced in the later section 4.1.2 as an example. The BLDC motor is the Anti-gravity 4006 from T-Motor, with a K_V number of $100 RPM/V$, internal resistance of 0.194Ω. Supplied with $32V$ and maximum current $20A$. Using 3.10, the K_T value of this BLDC motor is $0.0955 N \cdot m/A$.

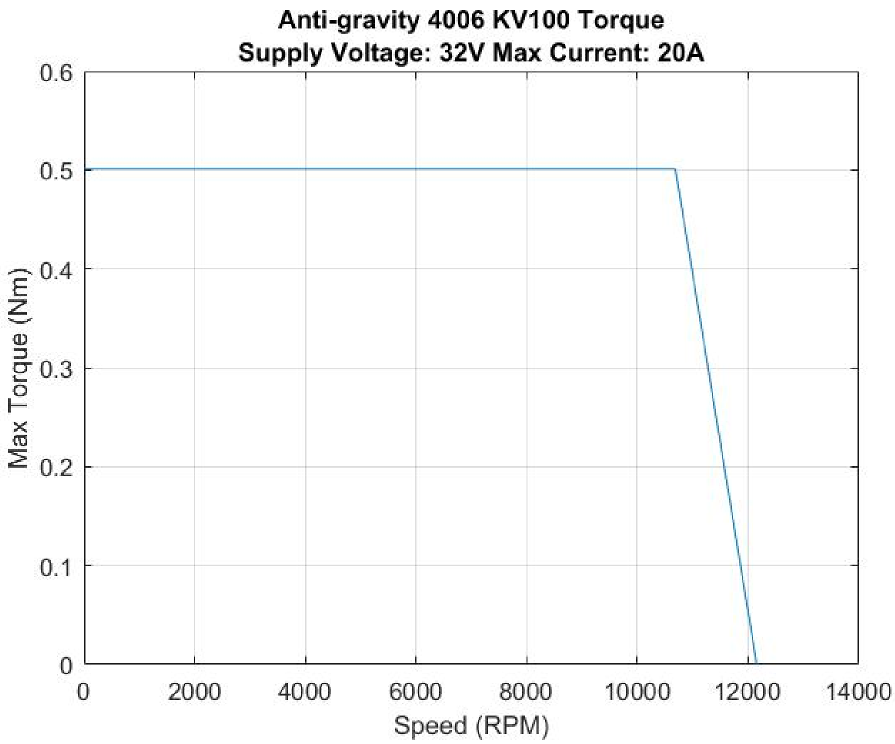

Figure 3.1: The theoretical maximum torque output curve of T-Motor Anti-gravity 4006 KV100 BLDC motor supplied with 32V voltage and maximum 20A current.

Using 3.4, the theoretical maximum speed under the condition above yields $48000 RPM$, and the current I drawn by the motor to produce maximum torque at speed ω can be calculated as below:

$$I = \begin{cases} I_{max}, & when\ \omega \leq 2812\ RPM \\ (U - \omega K_V)/R, & when\ \omega > 2812\ RPM \end{cases} \tag{3.13}$$

In 3.13, I_{max} is maximum current supplied, U is the supplied voltage and R is the internal resistance. Then the output torque of the motor can be simply calculated with 3.9

The theoretical maximum torque output under the given condition above is as shown in Figure.3.1.

The efficiency of the motor when running at speed ω producing torque T can be derived

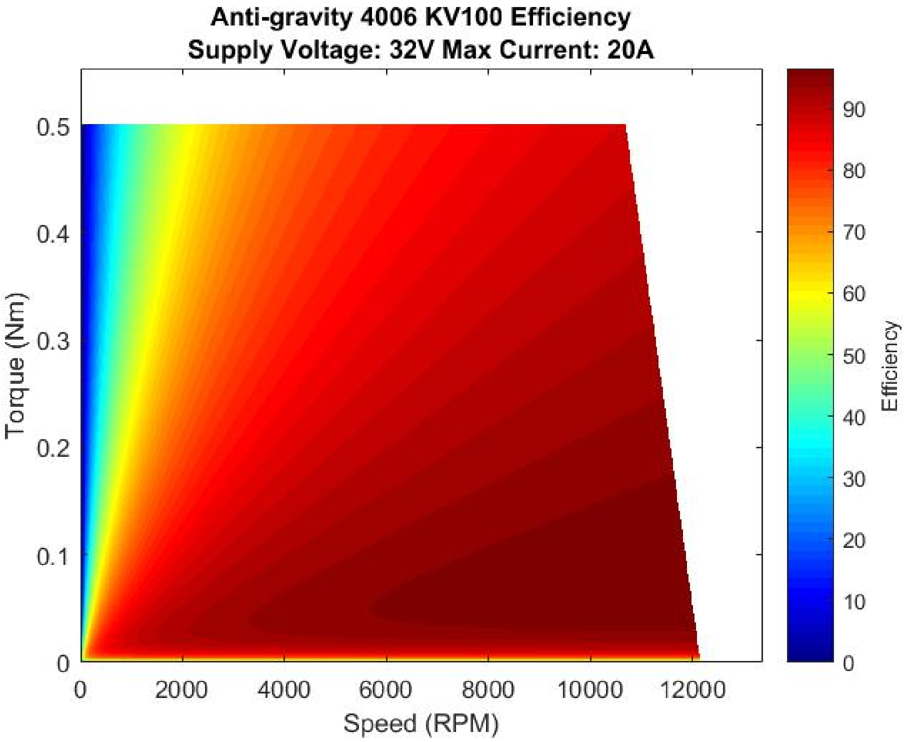

Figure 3.2: The theoretical output efficiency of T-Motor Anti-gravity 4006 KV100 BLDC motor supplied with 32V voltage and maximum 20A current.

as:

$$Efficiency = \frac{T \cdot \omega}{U \cdot I} \tag{3.14}$$

And the theoretical efficiency of this motor under above conditions is as presented in Figure.3.2.

3.1.2.2 Characteristics of Proprioceptive Quasi-Direct Drive Actuators

With all performance properties of BLDC motors explained in detail in the section above, it is very straight forward to find the characteristics of Proprioceptive Quasi-Direct Drive Actuators.

Denote the gear radio of a Proprioceptive Quasi-Direct Drive actuator is N, then in the perfect condition:

$$T_a = T_m \times N, \quad v_a = v_m/N \tag{3.15}$$

where T_a and v_a are the output torque and velocity of the Proprioceptive Actuator, T_m and v_m are the corresponding torque and velocity generated by the BLDC motor inside. However, there is always some power loss in all kinds of transmission, thus in reality:

$$T_a = T_m \times N \times \eta \tag{3.16}$$

where η is the overall mechanical efficiency of the transmission mechanism.

By combining 3.15 and 3.16 with 3.4 and 3.10, one can easily derive the constants for a Proprioceptive Actuator:

$$Ka_T = K_T \times N \times \eta, \quad Ka_V = K_V/N \tag{3.17}$$

where Ka_T and Ka_V are the torque constant and velocity constant for the Proprioceptive Actuator, K_T and K_V are the torque constant and velocity constant of the BLDC motor inside.

Since the transmission will only linearly scale down the output velocity while scale up the torque by the same magnification of the BLDC motor used on a Proprioceptive Actuator, the torque output curve of a Proprioceptive Actuator will just be a scaled version of the BLDC motor and shows the same trend as 3.1, and the efficiency of a Proprioceptive Actuator simply equals to the efficiency of the BLDC motor inside multiplied by η which is a constant that is only dependent to the transmission mechanism. Thus selecting a proper combination of BLDC motor and transmission according to the anticipated working condition of the

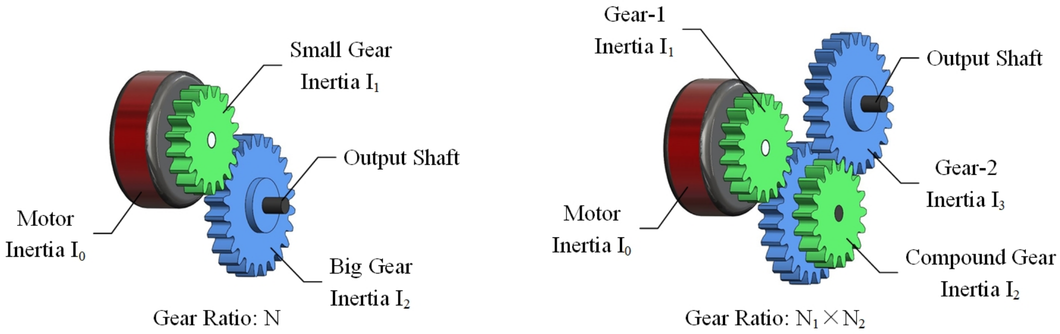

(a) (b)

Figure 3.3: Schematic drawing of motor with one stage gear train and two stage gear train.

Proprioceptive Actuator, so that the BLDC can be mostly working at a higher efficiency condition is very critical to the overall application efficiency of the Proprioceptive Actuator.

As discussed in Section.2.3, in contrast to position controlled servo motors with a very high gear ratio, the basic idea of Proprioceptive Actuators is to combine high-torque, low speed BLDC motors with low reduction ratio transmission so that compliance is inherent and high actuation transparency is achieved and permits accurate torque sensing and control directly based the current in the BLDC motor. And the key to dynamic actuation transparency is significantly reduced reflective inertia of the actuator.

When a motor with inertia I_0 is connected with a one-stage gear transmission with a gear ratio of N, as shown in Figure.3.3a, the inertia of the small gear of its rotation axis is denoted as I_1 and respectively I_2 for the big gear, then the reflected inertia of this actuation system at the output shaft is:

$$I_{out} = I_2 + N^2(I_1 + I_0) \tag{3.18}$$

If the same motor is combined with a two-stage gear transmission as shown in Figure.3.3b with gear ratio of each stage being N_1 and N_2, denote the inertia of the first small gear of its rotation axis as I_1 and respectively I_2 for the compound gear in the middle and I_3 for the big gear at output, then the reflected inertia of this actuation system at the output shaft is:

$$I_{out} = I_3 + {N_2}^2 I_2 + (N_2 N_1)^2 (I_1 + I_0) \tag{3.19}$$

In fact, when the transmission is an n-stage geartrain with gear ratio of N_i for the i-th stage, and denote the inertia of the first small gear of its rotation axis as I_1 respectively I_{n+1} for the last gear at output and I_i for the compound gear in the i-th stage, the reflected inertia of this actuation system at the output shaft can be expressed as:

$$I_{out} = I_{n+1} + {N_n}^2 I_n + ... + (N_n N_{n-1} ... N_i)^2 I_i + ... + (N_n N_{n-1} ... N_1)^2 (I_1 + I_0) \tag{3.20}$$

In the application of Proprioceptive Quasi-Direct Drive actuators, planetary gearing system is highly preferred over standard parallel axis gear trains. This is due to the fact that planetary gear trains provide higher power density in comparison to standard parallel axis gear trains, resulting in a reduction in volume,[41]. On top of that, planetary gearing systems also many other benefits over standard parallel axis gear trains, such as multiple kinematic combinations, purely torsional reactions, and coaxial shafting. A basic planetary gear system consists one or more outer, or planet, gears or pinions, revolving about a central sun gear or sun wheel[23][25], with an outer ring gear or annulus, which meshes with the planet gears. The planet gears in a planetary gearing system are always mounted on a carrier part. Figure.3.4a shows a simplified diagram of a planetary gear set that contains four planet gears. A planetary gear set can be used in three different configurations depending on the choice

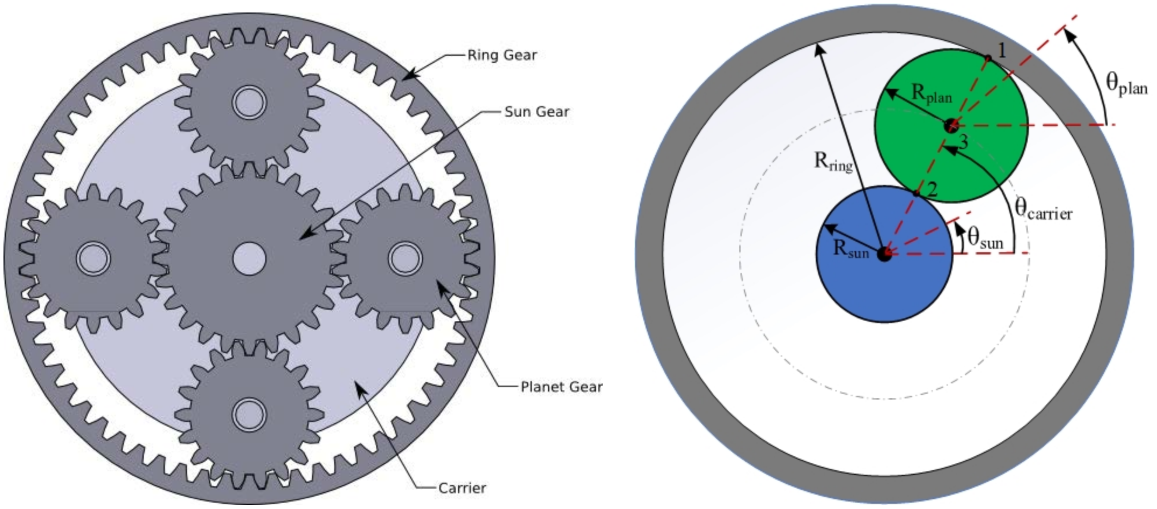

(a) A simplified diagram of a planetary gear set that contains four planet gears.

(b) Schematic drawing of a planetary gearing system.

Figure 3.4: Planetary gearset example.

of the fixed components: a. the carrier, b. the sun gear, and c. the ring gear.

when comes to the case of planetary gearing system, it is never more complicated than several steps of derivation. In connection with the topic of Proprioceptive Quasi-Direct Drive actuators, I'm only deriving the reflected inertia of a planetary gearbox in the case of fixing the ring gear and taking the sun gear is as input while the carrier as output, since this is the most seen configuration which can get the most power density out of a planetary gearbox as well as keeping the design as simple and compact as possible.

Shown in Figure.3.4b is a schematic drawing of a planetary gear set. As gears mesh with each other at their pitch circles, all gears are simplified into their pitch circles and thus they are all tangential to each other at the meshing points. The grey ring is the ring gear, the green disk is a planet gear and the blue disk is the sun gear. The carrier and other planet gears are hidden in the drawing. The ring gear is fixed and the sun gear is the input while the carrier is the output. As labeled in the figure, the planet gear meshes with the ring gear and the sun gear respectively at point 1 and 2. Point 3 indicates the center of the planet gear.

There is no slip in the gearing system under normal working condition thus: the velocity of point 1 is zero, and point 2 on the planet gear has the same velocity as point 2 on the sun gear:

$$\begin{aligned} &v_1 = 0 \\ &v_{2_{sun}} = v_{2_{planet}} = v_2 = R_{sun}\dot{\theta}_{sun} \end{aligned} \tag{3.21}$$

The speed of point 3 on the planet gear equals the average of the speed of point 1 and the speed of point 2:

$$v_3 = \frac{v_1 + v_2}{2} = \frac{1}{2}R_{sun}\dot{\theta}_{sun} \tag{3.22}$$

The speed of point 3 on the planet gear can also be expressed as:

$$v_3 = (R_{sun} + R_{planet})\dot{\theta}_{carrier} \tag{3.23}$$

By combining 3.22 and 3.23, we can derive for the angular velocity of the carrier:

$$(R_{sun} + R_{planet})\dot{\theta}_{carrier} = \frac{1}{2}R_{sun}\dot{\theta}_{sun} \Rightarrow \dot{\theta}_{carrier} = \frac{R_{sun}}{2(R_{sun} + R_{planet})}\dot{\theta}_{sun} \tag{3.24}$$

The speed of point 2 on the planet gear can also be expressed with the angular speed of the planet gear:

$$V_{2_{planet}} = -2R_{planet}\dot{\theta}_{planet} \tag{3.25}$$

By combining 3.21 and 3.25, we can derive for the angular velocity of the planet gear:

$$-2R_{planet}\dot{\theta}_{planet} = R_{sun}\dot{\theta}_{sun} \Rightarrow \dot{\theta}_{planet} = -\frac{R_{sun}}{2R_{planet}}\dot{\theta}_{sun} \tag{3.26}$$

Denote the input torque at the sun gear as T_{in}, the number of planet gears in the system as n_p. Assume that all planet gears share the load evenly, denote the tangential force at the interface between the sun gear and each planet gear as f_{sp}, and denote the momentum of inertia of the sun gear about its rotation axis as J_{sun}. Apply Newton's Second Law in Rotation (NSLR) to the sun gear, we have:

$$T_{in} - R_{sun} n_p f_{sp} = J_{sun} \ddot{\theta}_{sun} \tag{3.27}$$

Denote the

Under the 'even-load among planet gears assumption', denote the tangential force between each planet gear and the fixed ring gear as f_{pr}, and denote the force between each planet gear and the carrier as f_{pc}. Also respectively denote the momentum of inertia of the planet gear about its rotation axis on the carrier and its mass as J_{planet} and m_{planet} Apply NSLR to each planet gear, we have:

$$\begin{aligned} R_{planet} f_{pr} - R_{planet} f_{sp} &= J_{planet} \ddot{\theta}_{planet} \\ f_{sp} + f_{pr} - f_{pc} &= m_{planet} (R_{sun} + R_{planet}) \ddot{\theta}_{carrier} \end{aligned} \tag{3.28}$$

Denote the output torque from the planet carrier as T_{out}, and denote the momentum of inertia of the planet carrier about its rotation axis as $J_{carrier}$. Apply NSLR to the carrier:

$$(R_{sun} + R_{planet}) n_p f_{pc} - T_{out} = J_{carreir} \ddot{\theta}_{carrier} \tag{3.29}$$

Combine 3.24, 3.26, 3.27, 3.28 and 3.29, we can finally express the governing dynamical equation as follows:

$$T_{in} - \frac{R_{sun}}{2(R_{sun}+R_{planet})}T_{out} = \underbrace{\left[J_{sun} + n_p\left((\frac{R_{sun}}{2R_{planet}})^2 J_{planet} + (\frac{R_{sun}}{2})^2 m_{planet}\right) + \left(\frac{R_{sun}}{2(R_{sun}+R_{planet})}\right)^2 J_{carrier}\right]}_{I_{out},\ reflected\ inertia}\ddot{\theta}_{sun} \tag{3.30}$$

Denote the gear reduction ratio of this geartrain as N and further denote the speed ratio of the planet gears to the sun gear as N', then from 3.24 and 3.26:

$$N = \frac{R_{sun}}{2(R_{sun}+R_{planet})}, \quad N' = -\frac{R_{sun}}{2R_{planet}} \tag{3.31}$$

The reflected inertia of this planetary gearing system can be expressed as below with the contributions of the sun gear, planet gears, and planet carrier identified:

$$I_{out} = \underbrace{J_{sun}}_{\text{sun gear}} + \underbrace{n_p\left[N'^2 J_{planet} + \left(\frac{R_{sun}}{2}\right)^2 m_{planet}\right]}_{\text{planet gears}} + \underbrace{N^2 J_{carrier}}_{\text{carrier}} \tag{3.32}$$

An actuator system can be generally taken as a low-pass filter with its cutoff frequency f_0 being expressed as 3.33.

$$f_0 = \frac{1}{2\pi}\sqrt{\frac{k}{I}} \tag{3.33}$$

where k is the angular stiffness of the system and I is the reflective inertia. From 3.20 and 3.32 it is clear that the reflected inertia of the Proprioceptive Actuator increases exponentially as the gear reduction gets bigger, correspondingly, the actuator loses its actuation transparency exponentially. Yet there is no universal critical gear ratio at or beyond which the actuator is no more qualified as a Proprioceptive Actuator as it varies case by case, but it is safe to claim that the lower the gear ratio is, the more transparent the actuator is.

Even though it is very application dependent when discussing if a Proprioceptive Actuator is 'transparent' enough to provide the robotic system with adequate dynamic capabilities, especially when handling impacts, but we can still quantify the transparency of an actuator as well as the impact handling characteristics of a robotic system with the help of several specific metrics. As reviewed in Section.3.3.2, a metric named Impact Mitigation Factor (IMF) proposed by Wensing quantifies the transparency of an actuator by its impact mitigating capability, while in Section.3.3.3, a pair of metrics collectively called Impact Transfer Factors (ITF) proposed in this work start from the whole-system point of view and quantify the impact handling sensitivity of a dynamic robotic system.

3.1.3 Design Flow of Proprioception Quasi-Direct Drive Actuators

With above understanding of the actuator characteristics, the design flow of Proprioceptive Actuators is very straightforward.

Similar with the process of choosing a servo actuator for a certain application, the first step is to determine the basic requirement on the capability of the actuator according to the application. The basic information the designer needs to collect contains: the expected speed and torque range the actuator needs to cover, the size and weight limit from the application, and actuation power supply. The designer also needs to keep in mind that there is a chance that no satisfying solution can be found after applying all criteria, thus a priority order needs to be assigned to the requirements and loosen the low-priority ones when necessary.

With the power supply condition and the speed and torque requirements, the designer can derive the expected range of the constants for the Proprioceptive Actuator. From the size and weight limit, the approximate range for the BLDC motor form factor and size can be found.

The last step before finalizing the actual system design is to fix the BLDC motor and transmission selection. The BLDC motor can either be customized or directly chosen from commercially available options on the market. As discussed before, there is no clear borderline of gear ratio to judge if the actuation transparency of a Proprioceptive Actuator is good enough, but from the exponential relationship between gear ratio and reflective inertia, it is clear that lower the gear ratio is always preferred. On the other end, the recommended maximum gear ratio can be found by estimating the minimum natural frequency requirement of the actuator from the expected working conditions.

3.2 Dynamic Robotic Systems Design Optimization

When it comes to the design of a robotic system, it is never a work that is done at one stroke. The first design of a system can be disappointing, but the results from the first generation never meant that the core concept of the system is not viable. It is always the follow-up of optimization that turns something mediocre into fascinating, and eventually revives the true value of the original concept.

There are numerous aspects when it comes to the design optimization of a system, and most of them are covered by various theories and methods to follow as guidelines proposed by researchers in the field. As far as the work in this dissertation is concerned in terms of optimization related topics, it comes to mechanical intelligence in underactuated mechanisms and actuation configuration of legged robots.

3.2.1 Underactuated Systems And Potential Energy Flow

When applying Proprioceptive Actuators on compact systems, it is a good practice to adopt underactuated mechanisms when applicable, to effectively reduce the complicity, size and weight of a system.

3.2.1.1 Underactuated Mechanisms

Even though with uncertainty, motions of a functional underactuated mechanism should be predictable, as in most cases, underactuated DoF or joints are combined with elastic components, where accurate or active control is not needed and certain elastic behavior is preferred. Applying active compliant actuation onto such DoF or joints apparently becomes unnecessarily complicated, bulky, heavy or costly. When an underactuated mechanism is carefully designed such that it behaves in the exact way that is demanded by the system's application and even out performs activated mechanisms for the same task, it is said that such underactuated mechanism possess mechanical intelligence, or sometimes referred to as embedded intelligence. Underactuated mechanism with mechanical intelligence is often seen application to distal joints or subsystems of a robotic system, such as the ankle of a robot leg[58]. It is very frequently seen in robotic hands that the fingers are biomimetic, resulting a large number of DoF in the system.

3.2.1.2 Potential Energy Flow

As every sword has two blades, despite all the benefits that come along with under-actuation, a significant drawback is that trajectory and behavior uncertainty is introduced into the system. However, this problem can be solved by embedding mechanical intelligence, which reduces the difficulties of controlling such a system with inherent uncertainty by making the uncertainties predictable for light-weight systems whose inertia is too small to effect its behavior even when moving with high speed or for systems with considerable inertia under quasi-static conditions. Mechanical intelligence in under actuated system was first introduced about 30 years ago[63], but still has a relatively blurred definition.

Figure 3.5: The trajectories of a under-actuated system following rapid potential energy drop very much coincident with that of the rivers flowing through the terrain.

Previous researchers have tried to explain the mechanism of mechanical intelligence by embedding it in their specific systems via kinematics and force equations[63] or screw theory[49], but the results are usually limited to their own setups and are generally not scalable or applicable in other under-actuated mechanical systems.

A Potential Energy Flow theory is proposed below to explain the mechanism behind mechanical intelligence, which is believed to have the potential of being scaled or applied on other types of mechanical systems with underactuated DoF.

The actual form of equation can be different from case to case, but the theory can be demonstrated with the general derivation below. Assume an underactuated system with n joints, where $n \in \mathbb{Z}, n > 1$, and its joint space is denoted as $q \in \mathbb{R}^n$. The system has k actuated joints where $k \in \mathbb{Z}, k < n$, resulting in $n - k$ DoF of under-actuation. Denote the joints such that $q(i), 1 \leqslant i \leqslant k$ represents the joint position of the actuated joints.

The energy equality equation of the whole system can be expressed as:

$$E_P(q) + E_\mu(q) + W(q) = \sum_1^k M_i \tag{3.34}$$

where E_P represent the potential energy in the system and E_μ is the friction energy lost. Denote the energy that the system has output to the environment as W and the total energy pumped into the system from actuation on joint i as M_i. The kinematic energy in the system has been ignored under previous assumption of light-weight system or quasi-static condition.

The increase rate of the total potential energy in the system at position q is:

$$E_P(q)' = -\sum_1^n \frac{\partial E_\mu(q)}{\partial q(i)} - \sum_1^n \frac{\partial W(q)}{\partial q(i)} + \sum_1^k \frac{dM_i}{dq(i)} \tag{3.35}$$

Since at each point on the trajectory of the underactuated system with mechanical intelligence is stable, the total potential energy in the system at each point along the trajectory remains is a local minima. Thus the trajectory must be such that along which the increase rate of the total potential energy in the system remains the smallest. If imagine the potential energy of the system at each possible joint position forms a terrain with mountains and valleys, the trajectories of this underactuated system will very much coincident with that of the rivers flowing through the terrain. (Fig.3.5)

The potential energy flow theory is applied on DAnTE to guide the design of the underactuated fingers with mechanical intelligence, and the theory is explained in detail using

DAnTE-1 and DAnTE-2 as examples in Section.4.2

3.2.2 Actuation Configuration

Robots with multi-DoF can be designed in various different ways when it comes to their actuation configuration, but they all comes down to either serial or parallel configuration, or a hybrid combination of the two.

A parallel robot (also called parallel manipulator when used for manipulation, or parallel kinematic machine, when it is used as a machine tool) is a closed-loop kinematic chain mechanism of which the end-effector is connected to the base by several independent kinematic chains (legs) in parallel.[46] Comparing to a serial robot, each limb of a parallel robot (PR) tends to be simpler and shorter therefore more rigid, and the motors are purposely mounted close to the base in order to reduce the moving mass. Therefore, PRs have the following advantages: high stiffness because the external load is shared by multiple legs, high acceleration and high speed is very possible due to low moment of inertia of the moving structure, higher accuracy is also easier to achieve since the joint manufacturing and assembly errors will be even out rather than accumulated at the end-effector, and high force capabilities as the output force is contributed by multiple actuators working in parallel. The disadvantage of a PR lies in its limited workspace volume due to the parallel architecture, and there are often singularities in workspace.

PRs have received wide applications, such as flight simulators, high-precision positioning devices, pick-and-place manipulation, high-speed machining and metrology and coordinate machines. Most PRs provide 2 to 6 rotational or tranlation DoF, or a combination of both.

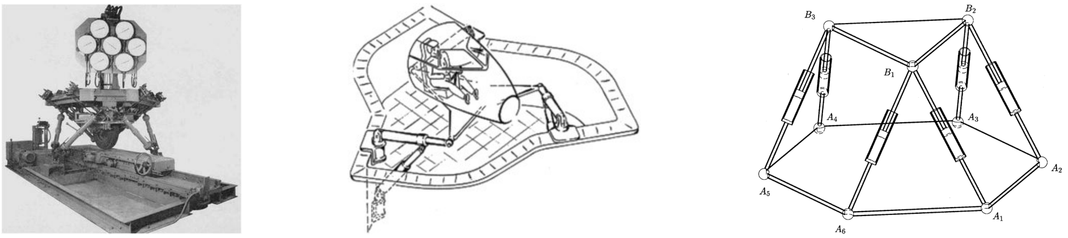

(a) Gough platform (b) Stewart flight simulator (c) Gough-Stewart schematic

Figure 3.6: Origin of parallel robots.

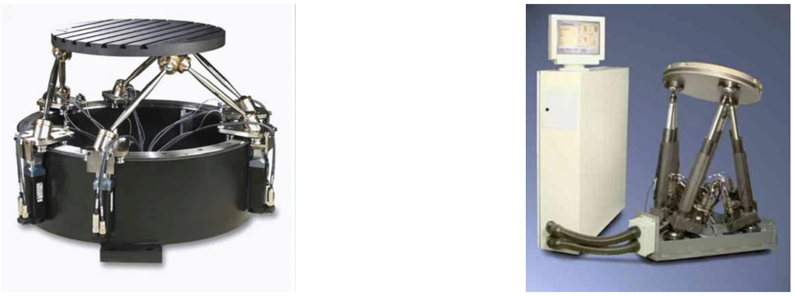

(a) R series (b) P series

Figure 3.7: Gough-Stewart parallel robots from Hexcel Corporation.

In most PRs, since the actuators are all mounted close to or directly on the base, linkages are used to connect the end-effector and the actuators. The earliest parallel manipulator is the Gough platform invented by Gough in 1947, which allows the positioning and the orientation of a moving platform so as to test tire wear and tear (Fig.3.6a). Stewart (1965) designed a parallel manipulator (Fig.3.6b) for use as a flight simulator in 1965. Since the two designs are in principle very similar with each other, this type of 6 DoF PR mechanism has been referred to as the Gough-Stewart mechanism (Fig.3.6c), followed by many design variants, such as the R series robots (Fig.3.7a) and P series robots (Fig.3.7b) developed by the Hexcel Corporation. The R series robots are driven by rotational actuators and

(a) A delta mechanism 3D printer

(b) 2 DoF manipulator

Figure 3.8: Based on the Delta robot, a number of variants of PRs have been designed and developed.

are designed for biomedical applications, while the P series robots are actuated by linear actuators and are aimed for industrial applications, such as welding, deburring, and milling. The groundbreaking Delta robot was patent in 1990[50]. Delta robot has only 3 DoF, allowing the end-effector to move with pure translation within the 3 dimensional space. The mechanism is very robust, simple and light-weight, presenting fast and accurate motions. This made it the go-to choice for pick-and-place motions in factories. As an extension of Delta robots, the IRB340 FlexPicker was introduced by ABB Flexible Automation in 1999. It is equipped with an integrated vacuum system capable of rapid pick-and-place of objects. Based on the Delta robot, a number of variants of PRs have been designed and developed. Two examples are shown in Figure 3.8 shows two examples: a delta mechanism 3D printer (Fig.3.8a) and 2 DoF manipulator for pick and place (Fig.3.8b).

Since linkages are most often used to combine the end-effector of a PR to its actuators, the configuration of these PRs are very friendly to hydraulic and pneumatic linear actuators, which are actuators integrated onto the linkages and thus result in systems that are very compact. As discussed above, This type of design can be seen on many industrial PRs where the robots are stationary and hydraulic or pneumatic power supply is easy to access and adequate, or in the case of electric magnetic motors are applied, the weight of the motors are not of little concern as in most cases they are mounted onto the base. However, the application of parallel mechanisms is not as optimal when it comes to legged robots. Pneumatic actuators are typically not used on legged robots as the output force of pneumatic actuators is not enough. Hydraulic actuators do have significant higher force output and they definitely can satisfy the demand of the joints on legged robots, but carrying a hydraulic pump makes the whole system relatively low on power density, not to mention the complicity of the system and difficulty of design and fabrication process. The workspace of parallel mechanism is inherently relatively limited, and since the whole mechanism takes up a big space due to the geometry, thus when used as legs, their workspace is further limited otherwise there is highly likely to have interference. Another reason why parallel mechanism is not very suitable for the application of legged robots is the difficulty in packaging. As mentioned before, the actuators of parallel mechanisms are mounted closely on the base. On a legged robot, there is at least 3 DoF per leg, while the space in the body is usually very limited, thus it is quite difficult to pack all the actuators. Nevertheless, considerable efforts have been made by researchers at all time to seek for the potential of taking advantage of the benefits of parallel mechanisms on dynamic legged robots. [18]

On the other hand, when a multi-DoF robot limb is designed in serial configurations, the workspace of the end-effector can easily be significantly bigger than what can be achieved with parallel configurations, and it is also much easier to make the limb very compact, especially when the total DoF of the limb gets larger. Thus it is very easy to understand why most robotic manipulators and legged robots are designed in serial configurations.

Compare to parallel configurations, one major drawback on serial configurations is the inertia of the limb tends to be significant larger. This can cause an impact that can not be ignored on the dynamic performance of the robotic system. Besides optimizing the design of the linkages to reduce their weight and inertia, another approach is to dislocate the actuators with the help of transmission mechanisms such that the actuators for distal joints are moved away from the joints they drive and mounted closer to the base, resulting in reduced limb inertia. And depending on the arrangement of the actuation and transmission, the actuation chain can be either in serial or parallel.

Shown in Figure.3.9 are examples of a simple 2DoF planar robot leg with the same serial joint configuration but different actuation configuration on the knee joint. In both Figure.3.9a and 3.9b, the knee joint actuation is in serial with the hip joint. Figure.3.9a shows a simple serial configuration that the knee actuator is co-located with the knee joint while Figure.3.9a shows a scenario where the knee actuator is dislocated from the knee joint to reduce the inertia and mass of the femur link. And the following relationship of the joint angles and actuator angles exists:

$$\theta_{hip} = \theta_{m_1}, \quad \theta_{knee} = \theta_{m_2} \tag{3.36}$$

where θ_{hip} and θ_{knee} respectively represent the angles of the hip and knee joint, while θ_{m_1} and θ_{m_2} are used to denote the angle of hip and knee actuator respectively. In comparison, the legs shown in both Figure.3.9c and 3.9d are the same in joint configuration as those in Figure.3.9a and 3.9b, but instead of serial actuation chain, the knee joint actuator on the

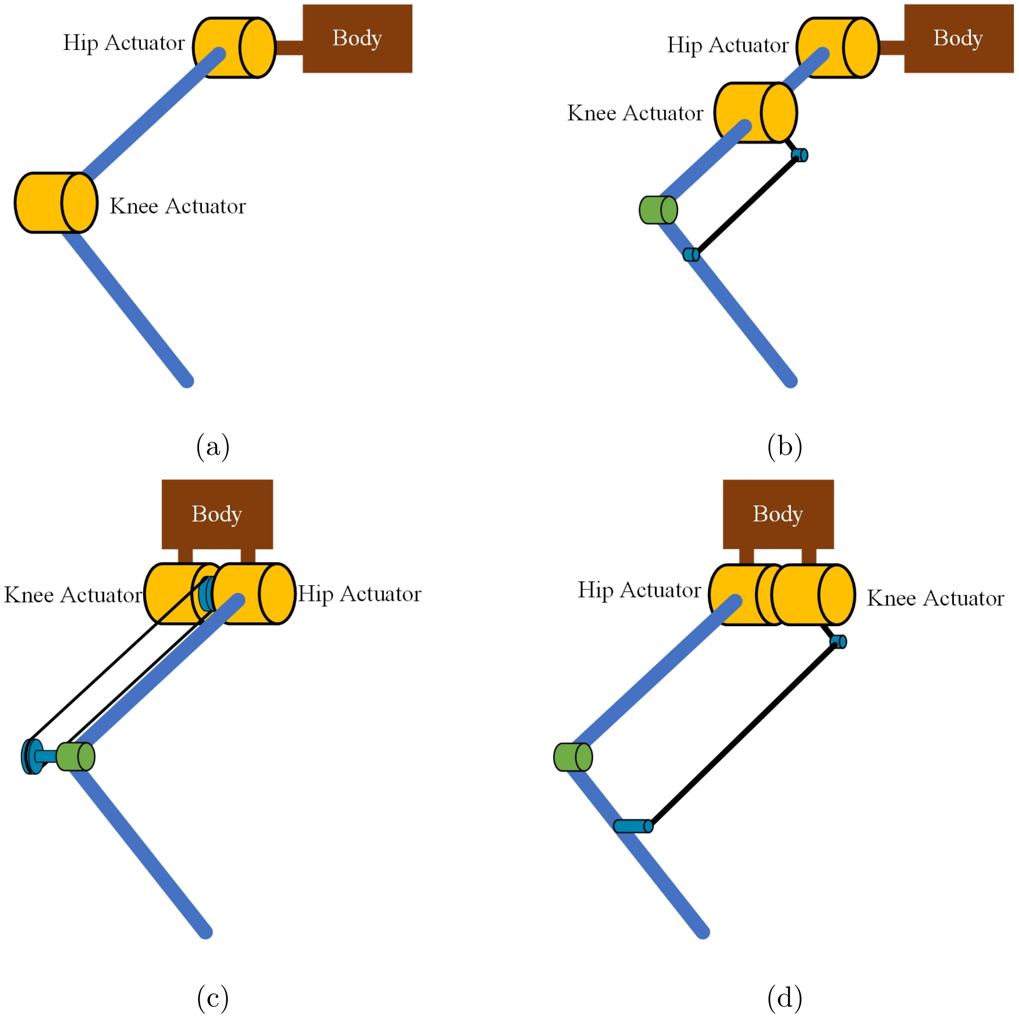

Figure 3.9: Examples of 2DoF serial configuration planar robot leg with serial and parallel actuation chain

legs in these two examples are in parallel with the hip actuators. Similar to the example in Figure.3.9b, the knee actuators are dislocated from the knee joints to reduce the inertia and mass of the femur links, with the help of a belt transmission (Fig.3.9c) or a four-bar linkage mechanism (Fig.3.9d), but the knee actuators in both examples are isolated mechanically from the hip actuator. The relationship of the joint angles and actuator angles changes to the following:

$$\theta_{hip} = \theta_{m_1}, \quad \theta_{knee} = \theta_{m_2} - \theta_{m_1} \tag{3.37}$$

As presented in Figure.3.9, different actuation chain can put the dislocated actuator in contrasting working conditions, and a improper actuation chain can cause serious mechanical antagonism.[1] Thus, it is very critical to carefully select the proper actuation chain to maximize the efficiency and dynamic performance of a robot with serial joint configuration when dislocating distal joint actuators. And a simple example is used below to illustrate this point.

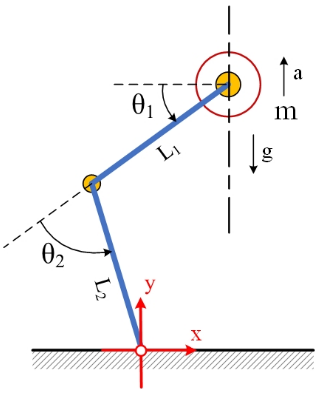

Figure 3.10: 2 DoF leg schematic for actuation chain analysis.

Figure.3.10 is a schematic drawing of a simple planar 2DoF serial hopper robot. Define the foot as origin and put the body on the right hand side of y-axis. The leg has mass less linkages and a body with no inertia but weights m. The body of the robot is represented by the red circle and it is constrained by a rail such that it can only move vertically. The length of the femur link is L_1 and the tibia link is L_2. The position of the hip and knee joints are respectively denoted as θ_1 and θ_2, with the direction of positive marked as in the drawing.

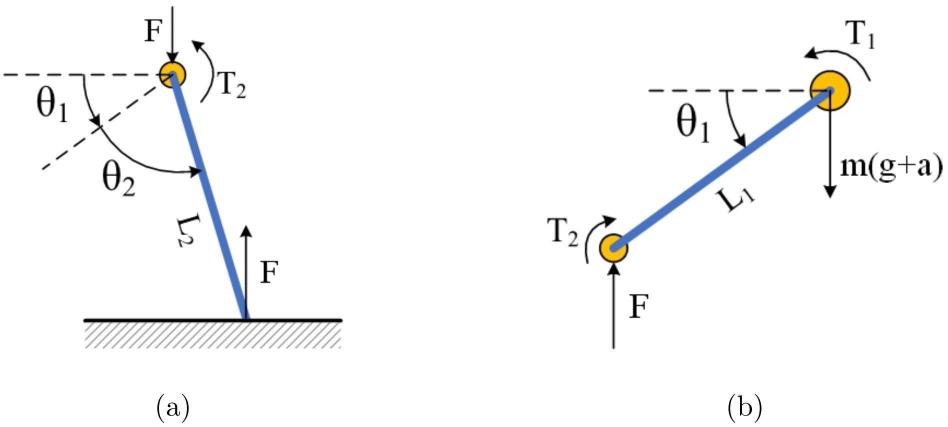

Figure 3.11: Free body diagram of (a) the tibia and (b) the femur of the 2DoF planar hopper robot shown in Figure.3.10 in the case of serial actuation chain configuration.

The body of the robot has an acceleration a pointing upwards going away from the ground. Denote the ground reaction force on the foot of the robot as F, and denote the joint torque on the hip and knee joint as T_1 and T_2.

When the joints on this hopper robot are driven by serial actuation chain, the free body diagrams of the tibia and the femur link are as shown in Figure.3.11. From the free body diagram of the tibia link in Figure.3.11a:

$$T_2 - FL_2cos(\theta_1 + \theta_2) = 0 \tag{3.38}$$

From the free body diagram of the femur link in Figure.3.11b:

$$T_{1_{serial}} = T_2 + m(g+a)L_1cos\theta_1, \quad F = m(g+a) \tag{3.39}$$

Combine 3.38 and 3.39, we can get:

$$\begin{aligned} T_2 &= m(g+a)L_2cos(\theta_1+\theta_2) \\ T_{1_{serial}} &= m(g+a)[L_1cos\theta_1 + L_2cos(\theta_1+\theta_2)] \end{aligned} \tag{3.40}$$

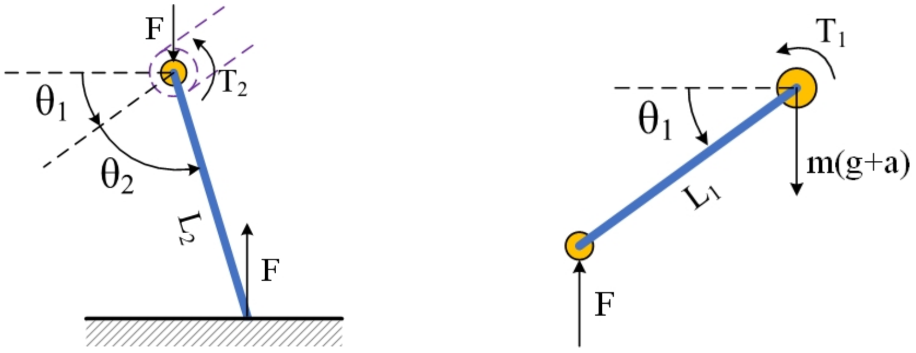

(a) (b)

Figure 3.12: Free body diagram of (a) the tibia and (b) the femur of the 2DoF planar hopper robot shown in Figure.3.10 in the case of parallel actuation chain configuration. Note that different from serial chain, there is no reaction torque on the femur link from the knee joint actuator.

While when the joints on this hopper robot are driven by parallel actuation chain using a belt transmission, the free body diagrams of the tibia and the femur link are as shown in Figure.3.12. From the free body diagram of the tibia link in Figure.3.12a:

$$T_2 - FL_2cos(\theta_1 + \theta_2) = 0 \tag{3.41}$$

When the knee joint actuator is in parallel with the hip joint, there is no reaction torque on the femur link from the knee joint actuator. From the free body diagram of the femur link in Figure.3.12b:

$$T_{1_{parallel}} = FL_1cos\theta_1, \quad F = m(g + a) \tag{3.42}$$

Now combine 3.41 and 3.42, we can get:

$$\begin{gathered} T_2 = m(g + a)L_2cos(\theta_1 + \theta_2) \\ T_{1_{parallel}} = m(g + a)L_1cos\theta_1 \end{gathered} \tag{3.43}$$

As the robot has a positive acceleration upwards going away from the ground, T_1 should be positive in both cases:

$$\begin{gathered} m(g+a)[L_1cos\theta_1 + L_2cos(\theta_1+\theta_2)] > 0 \Rightarrow L_1cos\theta_1 + L_2cos(\theta_1+\theta_2) > 0 \\ m(g+a)L_1cos\theta_1 > 0 \Rightarrow L_1cos\theta_1 > 0 \end{gathered} \tag{3.44}$$

When $\theta_1 + \theta_2 = \left(\frac{\pi}{2},\ \pi\right]$, we have $cos(\theta_1+\theta_2) < 0$. Thus, the following condition holds:

$$\begin{aligned} & L_1cos\theta_1 + L_2cos(\theta_1+\theta_2) < L_1cos\theta_1 \\ \Rightarrow & m(g+a)[L_1cos\theta_1 + L_2cos(\theta_1+\theta_2)] < m(g+a)L_1cos\theta_1 \\ \Rightarrow & T_{1_{serial}} < T_{1_{parallel}} \quad when\ \theta_1+\theta_2 = \left(\frac{\pi}{2},\ \pi\right] \end{aligned} \tag{3.45}$$

It is safe to claim from 3.40, 3.43 and 3.45 that when the leg works in conditions that $\theta_1 + \theta_2 = \left(\frac{\pi}{2},\ \pi\right]$, parallel actuation chain is more beneficial as the torque on the knee joint is the same for both cases but the hip joint torque is smaller than that in serial. In this case, the tibia link falls in the first quadrant, as shown in Figure.3.13a. In converse, serial chain appears to be more favorable when the leg works in conditions that $\theta_1 + \theta_2 = \left[\theta_1,\ \frac{\pi}{2}\right]$, and the tibia link falls in the second quadrant as represented in Figure.3.13b. $\theta_1 + \theta_2 = \frac{\pi}{2}$ is a neutral position where the torque on the knee actuators in both actuation chain are identical.

It is widely seen on legged creatures with sprawling posture to put their tibia link in the first quadrant as shown in Figure.3.13a. This posture is the most primitive, and is the original limb posture from which the others evolved. It is typically associated with trotting gaits, and the body flexes from side-to-side during movement to increase step length. All limbed reptiles and salamanders use this posture, as does the platypus and several species of frogs that walk. This provide great stability as well as low body height, making it easy for the animals to rest

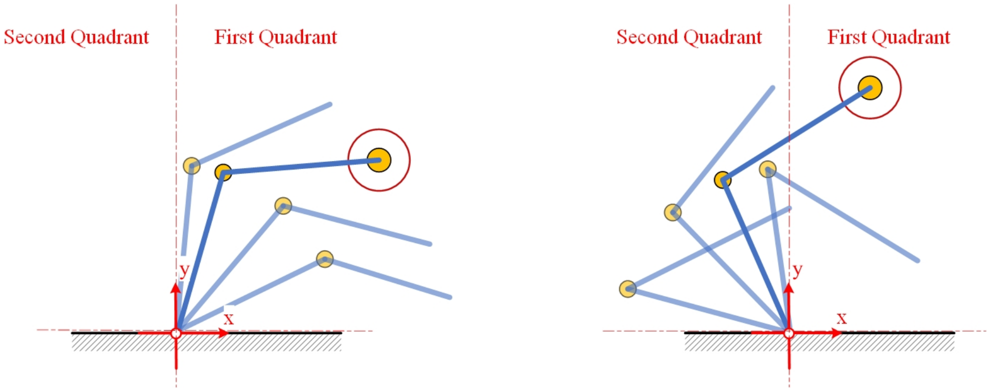

(a) Tibia link in the first quadrant (b) Tibia link in the second quadrant

Figure 3.13: The robot leg benefits from parallel actuation chain when its tibia link falls in the first quadrant as in 3.13a, but serial actuation chain when its tibia link falls in the second quadrant as in 3.13b

on their belly when not moving, but due to the fact that too much momentum change out of the direction of travel is created, it is pessimal for dynamic locomotion. In fact, nature mother only combines sprawling posture with cold-blooded animals, whose bodies naturally are not built for dynamic motions but only to move slow but stable.(Fig.3.14).

On the contrary, It is dynamically preferable for legged robots to adopt the condition as shown in Figure.3.13b where $\left[\frac{\pi}{2},\ \pi\right]$ with the neutral position included, which eventually

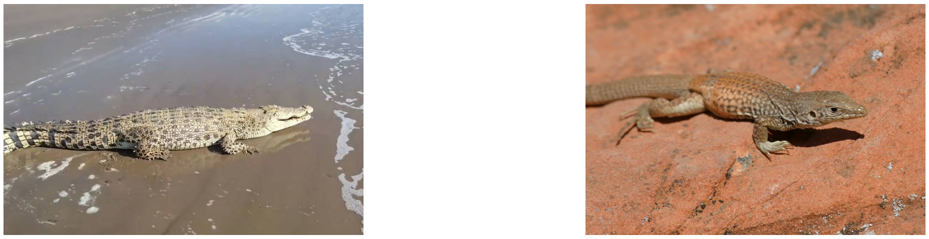

Figure 3.14: Cold-blooded animals like crocodile and lizard use sprawling posture to gain maximum stability.

Figure 3.15: When legged animals are traveling with a fast speed and highly dynamic locomotion, they tends to swing their legs so that their feet almost land where their sagittal planes intersects with the ground to minimize momentum change out of their sagittal plane.

results in a erect posture with the legs swing mostly in the sagittal plane. The momentum caused by leg swing is in line with the direction of travel and there is minimal twisting motion caused to the body. The legs swing with minimal angular momentum and the system is compactly contained, resulting in dynamic, efficient and practical locomotion. When legged animals are traveling with a fast speed and highly dynamic locomotion, they even swing their legs so that their feet almost land where their sagittal planes intersects with the ground to minimize momentum change out of their sagittal plane. See running cheetah and human in Figure.3.15. The effect actuation chain configurations have on dynamic locomotion is extremely critical for robots with Proprioceptive Quasi-Direct Drive actuators. Inappropriate actuation chain not only results in significant higher power cost during locomotion but also sets a demand for higher continuous torque at stance due to the lack of holding torque, which is the trade-off for actuation transparency. All these lead to negative impacts to the robot, such as poor performance, actuator overheating and short run time on battery. This is strongly supported by a joint actuator overheating phenomenon that happens frequently on robot ALPHRED-2.(see Section.4.3.2)

On modern dynamic robots with limbs with high DoF, in order to reduce limb inertia and enhance dynamic performance, it is practical to utilize some parallel mechanism design to dislocate the actuators closer to the body/base for distal joints. While other joints remain in serial configuration to keep the benefits of serial configuration, such as compactness and

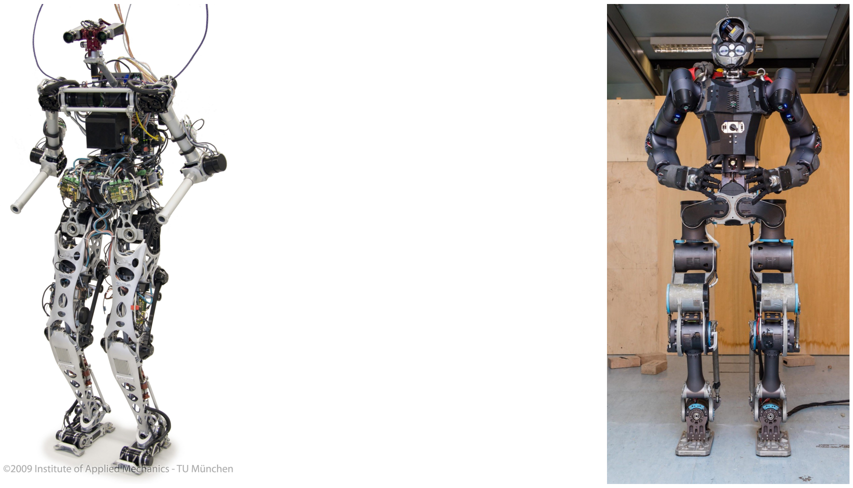

(a) Lola (b) Walkman

Figure 3.16: Parallel mechanisms on the ankle of humanoid robots

(a) (b)

Figure 3.17: Humanoid robot lower body with hybrid legs3.17a and its schematic drawing3.17b.

large workspace. Hybrid mechanism is formed by combining parallel mechanism and serial mechanism. On legged robots, most of hybrid designs apply parallel mechanism to an ankle structure in order to realize compact ankle joint and small leg inertia by bringing the actuator closer to the hip. For example, the leg of humanoid robot LOLA (Fig.3.16a) has a typical 6-DOF serial structure but the 2 DOF ankle joint is actuated by two spatial slider-crank mechanism instead of placing two actuators at the ankle joint [62]. WALKMAN (Fig.3.16b), a humanoid robot developed at IIT, also applied 4-bar transmission to its knee and ankle joints to reduce the inertia and maximize its dynamic performance [39]. A hybrid legged biped robot leg developed by Disney (Fig.3.17a) utilize parallel mechanism to move the actuators for 2DoF among the 3DoF ankle joint plus the knee joint. The hybrid Leg is composed of a pair of 3 DOF chains connected in parallel at the end. Each chain adopts a 5-bar linkage mechanism that realizes the hip pitch and knee pitch motions in order to place the actuators close to the hip [19]. Figure.3.17b shows a schematic of this hybrid leg. A kid size humanoid robot called BRUCE is presented in Section. 4.3.3. BRUCE is a highly dynamic bipedal robot powered by Proprioceptive Actuators. Hybrid configuration is adopted in the design of BRUCE's leg. Different from all mentioned above, the parallel mechanism is achieved by bevel gears and is applied to the hip joint, resulting in a relatively simple and compact hip joint assembly, as well as reduced leg inertia.

3.3 Impact Mitigation, Transfer and Handling

As robotics technology becomes more mature, we are seeing an increasing trend in more dynamic motions generated by the algorithms and executed by the capable hardwares. This trend is most evident in legged robots such as quadrupeds like MIT Cheetah 3 [59] and ALPHRED-2 [27] and bipeds like ATLAS [8] and NABi-2 [72]. However, it can also be observed with manipulators and end-effectors [74] [73]. Compared to the past when robots were more quasi-static [38], these recent systems interact with the environment more dynamically, and impacts that stem from these interactions at the point of contact should no longer be simply ignored as it particularly can expedite failures in the mechanical components.

Consequently, as a first step, it is necessary to understand and quantify how a robotic system reacts upon receiving an impact, and researchers have accordingly studied matters such as finding out how an impulsive load changes the status of a robotic system [75]. Nevertheless, the relationship between impacts and dynamic robotic systems is non-trivial as impact is in essence a collision, and the magnitude differs depending on the task at hand. For example, sometimes the impact can be a soft touch to detect an event such as an end-effector trying to detect contact with a target object, while other times the impact itself can potentially cause mechanical damage to the robot in cases such as a humanoid falling after losing balance. Occasionally, impacts occur repeatedly and frequently, and they are inherent to the tasks and motions the robot is designed for, which is the case with legged robots. Particularly in the last case, it is critical for the robots to be able to effectively mitigate impacts, as otherwise, the impact will damage the robot. Special research emphasis is placed on actuators for these robots because the traditional setups use high gear ratio actuators that would never be able to withstand the repeated impacts from conducting dynamic locomotion. This has sprung research in not just actuators [76], but also in generating metrics that can be used for quantitative analysis on impacts for dynamic quadrupedal systems, and the most developed and useful metric is the Impact Mitigation Factor[64] which is briefly reviewed in Section.3.3.2.

However, there is still a lack of metrics when it comes to quantifying the risk of damaging the robotic system upon collision or equally the sensitivity of a robotic system to impulsive contact. To address this issue, proposed in this work is a pair of metrics called the Impact Force Transfer Factor (IFTF) and the Impact Velocity Transfer Factor (IVTF)—collectively called the Impact Transfer Factors (ITF)—to assist in quantifying and evaluating potential effects impacts and collisions can have on a robotic system. The theory is presented in detail in Section.3.3.3.

3.3.1 System Impact Response

The rigid-body impact dynamics calculation is the basement for the development of both Impact Mitigation Factor and Impact Transfer Factors. It is not much different from [75], and it is briefly presented for completeness purposes.

Given a floating base n-link robot in three-dimensional space, with base coordinates $q_b \in \mathbb{R}^6$ and internal (i.e. joint) coordinates $q_j \in \mathbb{R}^n$, the equation of motion is defined as [40]:

$$D(q)\ddot{q} + H(q, \dot{q}) + G(q) = T \tag{3.46}$$

where $D(q) \in \mathbb{R}^{(6+n)\times(6+n)}$ is the inertia matrix of the robot, $q = [q_b, q_j]^\top \in \mathbb{R}^{6+n}$ is the $(6+n)\times 1$ vector of the generalized coordinates representing joint positions, and $H(q, \dot{q})$ and $G(q)$ includes the Coriolis, nonlinear, and gravity terms. Suppose that the end-effector of this

n-link robotic system collides with the environment, and the position of the collision point on the robot is denoted X_r with respect to the base coordinate system. By transformation, X_r can be expressed in terms of the generalized coordinates q [40]:

$$X_r = f(q) \tag{3.47}$$

We consider the collision as totally inelastic and no deformation of the robotic system or the environment. In association with this constraint, there exists a generalized force F acting on the system [65]:

$$F = \left[\frac{\partial f}{\partial q}\right]^{\top} \boldsymbol{\lambda} = {J_s}^{\top} \boldsymbol{\lambda} \tag{3.48}$$

where $J_s \in \mathbb{R}^{3\times(6+n)}$ is the contact Jacobian matrix and $\boldsymbol{\lambda}$ is a three-dimensional vector of Lagrange multipliers. The equation of motion now can be expressed as:

$$D(q)\ddot{q} + H(q, \dot{q}) + G(q) = T + F \tag{3.49}$$

In the case of the inelastic impact assumed here, the time of collision is infinitesimally short and the constraint force can be modeled as an impulse at the moment of collision. Let the generalized constraint force be denoted as:

$$\Gamma = {J_s}^{\top} \boldsymbol{\lambda}$$

Then, in the case of collision, (3.49) becomes:

$$D(q)\ddot{q} + H(q,\dot{q}) + G(q) = T + \Gamma \tag{3.50}$$

Assume collision happens at time t_0. Under the total inelastic assumption, impacts happen instantly, and it is logical to assume an infinitesimally short time interval Δt. During the infinitesimally short time interval of collisions, the joint positions of a robotic system remain unchanged since joint angular velocities are finite whose integrals over an infinitesimally short time interval are zero. Under this basic assumption, one may integrate both sides of (3.50) for an infinitesimally short time interval:

$$\begin{aligned} &\lim_{\Delta t \to 0} \int_{t_0}^{t_0+\Delta t} D(q)\ddot{q}dt \\ &+ \lim_{\Delta t \to 0} \int_{t_0}^{t_0+\Delta t} [H(q,\dot{q}) + G(q) - T]dt \\ &= \lim_{\Delta t \to 0} \int_{t_0}^{t_0+\Delta t} \Gamma dt \end{aligned} \tag{3.51}$$

As $\Delta t \to 0$ to satisfy the assumption, the second term on the left hand side vanishes, and (3.51) becomes:

$$D(q)[\dot{q}(t_0 + \Delta t) - \dot{q}(t_0)] = \int_{t_0}^{t_0+\Delta t} \Gamma dt \tag{3.52}$$

Magnitude of the impulse goes towards infinity as $\Delta t \to 0$, and the right side of (3.52) converges towards a finite value that we call the generalized impulsive force, denoted as:

$$\Gamma_\delta = \int_{t_0}^{t_0+\Delta t} \Gamma dt = {J_s}^\top \int_{t_0}^{t_0+\Delta t} \boldsymbol{\lambda}_\delta dt \tag{3.53}$$

Then from (3.52) one may have:

$$\dot{q}(t_0 + \Delta t) - \dot{q}(t_0) = D^{-1}(q)\Gamma_\delta \tag{3.54}$$

For simplicity, we assume that the collision point on the environment is stationary. Upon collision, (3.47) can be expressed as:

$$X_r(t_0) = f(q(t_0)) \tag{3.55}$$

and the velocity of the collision point on the robot can be expressed as:

$$\dot{X}_r(t_0) = J_s\dot{q}(t_0) \tag{3.56}$$

Equation (3.53), (3.54), and (3.56) can now be used to get:

$$\begin{aligned}\Delta\dot{X}_r &= \dot{X}_r(t_0 + \Delta t) - \dot{X}_r(t_0)\\ &= J_s(\dot{q}(t_0 + \Delta t) - \dot{q}(t_0))\\ &= J_s D^{-1}(q) {J_s}^\top \int_{t_0}^{t_0+\Delta t} \boldsymbol{\lambda}_\delta dt\end{aligned} \tag{3.57}$$

As long as J_s has a rank of three and $D^{-1}(q)$ is a positive definite square matrix, $J_s D^{-1}(q) {J_s}^T$ is invertible [24]. Consequently, Γ_δ can be expressed in terms of q and X_r:

$$\Gamma_\delta = J_s^\top (J_s D^{-1}(q) {J_s}^\top)^{-1} \Delta\dot{X}_r \tag{3.58}$$

3.3.2 Impact Mitigation

Impact mitigation behavior and capability of a robot system was never a concern before, when the majority of robotic systems were assumed to be working under quasi-static status. As robotic platforms nowadays get much more dynamic, especially in the cases of legged robotic systems, as the robots interact with the environment, other robots or even humans, frequent impacts become inherent to their motions and are never negligible. Impact mitigating capability becomes a feature of great importance. Most legged robots and robotic manipulators uses rigid linkages to ensure motion accuracy and minimize control uncertainty. Researchers from MIT came up with a new metric named the "impact mitigation factor" (IMF) to quantify mitigating capability at impact, which enables design comparison across a wide class of robots[64], and is reviewed here for reference, as the purpose of the Impact Transfer Factors theory is to complete the part of the loop of impact handling that IMF does not cover.

Continue to the derivation in Section.3.3.1, denote the total impact on the contact point felt by the robotic system as T, then from 3.74 we can find:

$$J_s{}^{\top} T = \Gamma_\delta \tag{3.59}$$

and further express T as:

$$\begin{aligned} T &= \Lambda \Delta \dot{X}_r \\ \Lambda &= (J_s D^{-1}(q) J_s{}^{\top})^{-1} \end{aligned} \tag{3.60}$$

where $\Lambda \in \mathbb{R}^{3\times3}$ is defined as the operational-space inertia matrix (OSIM) [32], [4] of the system felt at the contact.

Define the joint motor inertia matrix as:

$$d_{mot} = \begin{bmatrix} I_{m_1} & & & \\ & I_{m_2} & & \\ & & \ddots & \\ & & & I_{m_n} \end{bmatrix} \in \mathbb{R}^{n \times n} \tag{3.61}$$

where I_{m_i} is the inertia of the actuator for joint i. Further define D_{mot} such that:

$$D_{mot} = \begin{bmatrix} 0 & 0 \\ 0 & d_{mot} \end{bmatrix} \in \mathbb{R}^{(6+n) \times (6+n)}$$

Then the inertia matrix D can be partitioned as:

$$D = D_{mot} + D_{rb} \tag{3.62}$$

where D_{rb} is the portion of the inertia matrix that represents all the rigid-body links. Then the OSIM as defined in 3.60 can be expanded as:

$$\Lambda = [J_s (D_{mot} + D_{rb})^{-1} {J_s}^{\top}]^{-1} \tag{3.63}$$

To assist further development, rewrite 3.46 and partition the inertia matrix $D(q)$ such that:

$$\begin{bmatrix} D_{bb}(q) & D_{bj}(q) \\ D_{jb}(q) & D_{jj}(q) \end{bmatrix} \begin{bmatrix} \ddot{q}_b \\ \ddot{q}_j \end{bmatrix} + H(q, \dot{q}) + G(q) = T \tag{3.64}$$

Also partition the contact space Jacobian J_s:

$$J_s = [J_b, J_t] \tag{3.65}$$

where J_t is the joint space Jacobian:

$$J_t = \frac{\partial f_m}{\partial q_j}, \quad J_t \in \mathbb{R}^{3\times n} \tag{3.66}$$

In the worst case scenario, if reflected inertia become arbitrarily large on each joint, the system will roughly behave as if all the joints are locked. This worst case design can be used as a benchmark to evaluate the effects of reflected inertia in designs with the joints free to move. In this locked system, there is essentially no moving joints, and the system's inertia matrix is simply reduced to $D_{bb} \in \mathbb{R}^{6\times 6}$ and the generalized coordinates are reduced to just the base coordinates $q_b \in \mathbb{R}^6$. An impact velocity $v = \Delta\dot{X}_r$ would cause a contact impulse T_L to a locked system as:

$$T_L = (J_b D_{bb}^{-1} {J_b}^{\top})^{-1} v \tag{3.67}$$

With this insight, a locked contact inertia Λ_L is defined as:

$$\Lambda_L = (J_b D_{bb}^{-1} {J_b}^{\top})^{-1} \tag{3.68}$$

Given the locked impulse T_L , equal impact velocity v are achieved when the free system experiences an impulse T_0:

$$T_0 = \Lambda {\Lambda_L}^{-1} T_L \tag{3.69}$$

The term $\Lambda {\Lambda_L}^{-1}$ characterizes how much inertia is "felt" at a impact generated by the same impact velocity in comparison to the reference, which is the locked system inertia. The reduction in impulse is then given by

$$T_L - T_f = \underbrace{(I - \Lambda {\Lambda_L}^{-1})}_{:= \Xi} T_L \tag{3.70}$$

where the researchers (Patrick M. Wensing & etc.) at MIT introduce Xi as an impact mitigation matrix, and its determinant

$$\xi := det(\Xi) \tag{3.71}$$

as the impact mitigation factor (IMF).[64] IMF is stated to be used to quantify the effectiveness the free dynamics of a mechanism at mitigating impacts.

According to Wensing, this new factor has interesting properties that pertain to the backdrivability of a mechanism, which is the backdrivability of the actuators in rigid-body systems. An IMF $\xi = 1$ corresponds to a system with perfect inertial backdrivability that is capable of mitigating all impact, whereas $\xi \rightarrow 0$ as $\Lambda \rightarrow \Lambda_L$. Due to the normalization provided from the locked case (with roughly infinite reflected actuator inertia), the IMF is a nondimensional quantity that enables comparison across machines of different scale.

Furthermore, a directional IMF (DIMF) is defined to quantify the capability of a design to mitigate impact in a particular direction. Given a direction $\vec{x}$:

$$\xi_x = 1 - \frac{\frac{1}{2}\vec{x}^\top \Lambda \vec{x}}{\frac{1}{2}\vec{x}^\top \Lambda_L \vec{x}} \tag{3.72}$$

where ξ_x inherits the property that $0 \leq \xi_x \leq 1$ from the fact that $\Lambda_L \geq \Lambda$. This DIMF has a clear physical interpretation as well. The kinetic energy lost due to an impact with velocity v is:

$$\Delta E = \frac{1}{2} v \Lambda v \tag{3.73}$$

Thus, ξ_x quantifies the percent decrease in energetic losses afforded through the free dynamics of the mechanism when impacting in direction x.

3.3.3 Impact Transfer

By using IMF we can quatified the portion of a impact that is mitigated by the actuators, but the influence on the system from the unmitigated portion of the impact is still left unclear. In another word, the effects impacts and collisions can have on a robotic system is not quantified, and there is still a lack of metrics when it comes to quantifying the risk of damaging the robotic system upon collision or equally the sensitivity of a robotic system to impulsive contact. To address this issue, a pair of metrics called the Impact Force Transfer Factor (IFTF) and the Impact Velocity Transfer Factor (IVTF)—collectively called the Impact Transfer Factors (ITF)—is proposed as following.

3.3.3.1 Theory of Impact Transfer Factors

From 3.54 we have:

$$\Gamma_\delta = D\Delta\dot{q} \tag{3.74}$$

Now we introduce the Impact Transfer Factors, building off the notations introduced in Section 3.3.1 and Section 3.3.2.

The impact on the actuators can be expressed as:

$$\Gamma_{mot} = d_{mot}\Delta\dot{q}_j \tag{3.75}$$

This results in being able to define Γ_m using D_{mot}, Γ_{mot}, and $\Delta\dot{q}$ as:

$$\Gamma_m = \begin{bmatrix} 0 \\ \\ \Gamma_{mot} \end{bmatrix} = D_{mot}\Delta\dot{q} \tag{3.76}$$

Now, by using (3.76) and (3.54), we can get:

$$\Gamma_m = D_{mot} D^{-1} \Gamma_\delta \tag{3.77}$$

Now, defining the position of collision on the robot end-effector relative to its body as X_m, it can be expressed in terms of the generalized coordinates q_j:

$$X_m = f_m(q_j) \tag{3.78}$$

Using the joint space Jacobian J_t as in 3.66, the velocity of the collision contact point with respect to the robot body can be expressed as:

$$\dot{X}_m = J_t \dot{q}_j \tag{3.79}$$

Let us define the proprioceptive impact as the portion of T that is transferred to the motors. This impact, notated with P, is defined as:

$$P = J_t \Gamma_{mot} \tag{3.80}$$

Using (3.76), (3.77), and (3.59), the following relationship can be found:

$$D_{mot} D^{-1} {J_s}^\top T = \begin{bmatrix} 0 \\ \Gamma_{mot} \end{bmatrix} \tag{3.81}$$

Expanding D^{-1} as below:

$$D^{-1} = \begin{bmatrix} D_1 \\ D_2 \end{bmatrix} \tag{3.82}$$

where $D_2 \in \mathbb{R}^{n\times(n+6)}$, it can be found that:

$$D_{mot}D^{-1} = \begin{bmatrix} 0 \\ \\ d_{mot}D_2 \end{bmatrix} \tag{3.83}$$

Now by bringing (3.83) back into (3.81), we have the following results:

$$\begin{bmatrix} 0 \\ \\ d_{mot}D_2 \end{bmatrix} {J_s}^\top T = \begin{bmatrix} 0 \\ \\ \Gamma_{mot} \end{bmatrix}, \quad d_{mot}D_2{J_s}^\top T = \Gamma_{mot} \tag{3.84}$$

Further combining (3.84) and (3.80) results in:

$$P = \boldsymbol{K_F}T, \quad \boldsymbol{K_F} = J_t d_{mot} D_2 {J_s}^\top \tag{3.85}$$

where here, $\boldsymbol{K_F}$ is defined as the **impact force transfer matrix**.

Additionally, substituting (3.75) and (3.80) into (3.84), the following relationship can be found:

$$\Delta \dot{q}_{mot} = D_2 {J_s}^\top T \tag{3.86}$$

We can additionally use (3.79) to express the velocity change of the collision contact point relative to the robot body (i.e. the proprioceptive velocity change due to the impact) as:

$$\Delta V = \boldsymbol{K_V}T, \quad \boldsymbol{K_V} = J_t D_2 {J_s}^\top \tag{3.87}$$

where here, $\boldsymbol{K_V}$ is defined as the **impact velocity transfer matrix**.

Assume a 3 dimensional unit impact:

$$\vec{I} = \begin{bmatrix} I_x \\ I_y \\ I_z \end{bmatrix}, \quad {I_x}^2 + {I_y}^2 + {I_z}^2 = 1$$

Under impact $\vec{I}$, the magnitude of the corresponding proprioceptive impact and velocity change as felt by the system are:

$$\alpha = \left| K_F \vec{I} \right| \quad \beta = \left| K_V \vec{I} \right| \tag{3.88}$$

We define α and β as the **Impact Force Transfer Factor (IFTF)** and the **Impact Velocity Transfer Factor (IVTF)** respectively, and they are functions of the unit impact vector $\vec{I}$.

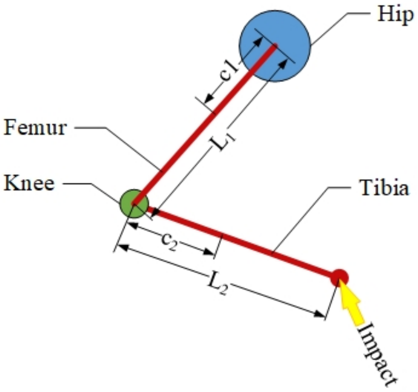

Figure 3.18: The 2DoF robot limb configuration used in the simulation. Impact is loaded onto the end of the tibia link, which is also called the end-effector.

These transfer matrices and factors can become useful primarily in the following two aspects: joint protection and impact detection. First, for joint protection, the structural components such as shafts, brackets, and bearings are assumed to be robust to the expected impacts and it is mainly to protect the impact sensitive components of the joint, such as gearboxes, ballscrews, and force-torque sensors. When the direction of the impact is known, the IFTF can be calculated and the risk of the sensitive components being damaged or destroyed under the impact can then be easily and methodologically evaluated.

Thus the optimal motion for a robotic limb to take impact and minimize potential damage can be chosen. Furthermore, if one or multiple specific joints out of all joints are to be independently evaluated, one can simply set the inertia of the uninterested joints in (3.61) as zero. Second, when it comes to impact detection, the derived transfer matrices and factors can help with choosing motions with the optimal sensitivity to an impact with known direction, or choosing the better signal source between velocity and torque for optimal impact detection when the limb motion and impact direction are known. These will be explained in further detail with examples in Section 3.3.3.2.

3.3.3.2 Simulation of ITF

The theory is applied onto a 2 degree-of-freedom (DoF) robotic limb in simulation, as shown in Fig. 3.18.

For simplicity, the hip of the robotic limb has no inertia therefore no shape or volume is considered for it. Actuators are collocated on the joint, with the running example having one on the hip joint and the other on the knee joint. Assume the impact from the environment happens at the tip of the tibia link. Parameters of this robotic limb are as shown in Table 3.1.

In the simulation, with the robot in different configurations, unit impulses from all directions are applied to the tip of the tibia link. The corresponding IFTF (α) and IVTF (β) are plotted. Two cases with different end-effector locations are simulated and in each case, three plots are generated to help with understanding and studying the results, as shown in

Table 3.1: Parameters of the 2-DoF robotic limb in simulation.

Parameter	Symbol	Unit	Value
Hip Mass	m_0	kg	10
Hip Motor Mass	m_{r1}	kg	1
Knee Motor Mass	m_{r2}	kg	0.5
Hip Motor Inertia	I_{r1}	$kg \cdot m^2$	5
Knee Motor Inertia	I_{r2}	$kg \cdot m^2$	0.3
Femur Mass	m_1	kg	0.3
Tibia Mass	m_2	kg	0.1
Femur Inertia	I_1	$kg \cdot m^2$	0.3
Tibia Inertia	I_2	$kg \cdot m^2$	0.1
Femur Length	L_1	m	0.5
Tibia Length	L_2	m	0.5
Femur CoM Location	c_1	m	0.35
Tibia CoM Location	c_2	m	0.1

Fig. 3.19.

In the first plot, the ITF and the unit impulses are plotted in polar coordinates, with the polar angle representing the direction of the impulse, and the radius representing the magnitudes of the ITF. The corresponding robot configuration is also drawn with the end-effector placed at the center of the plot. In the second and third plots, the ITF are plotted

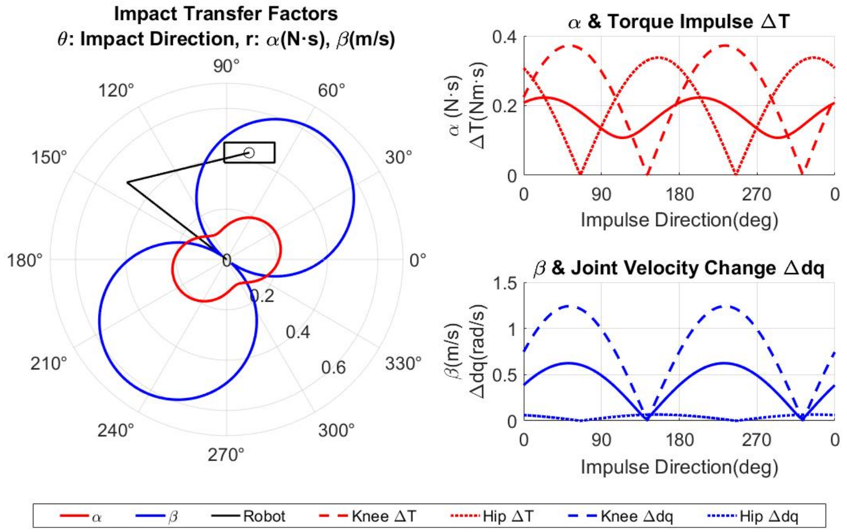

(a) Case 1 simulation results.

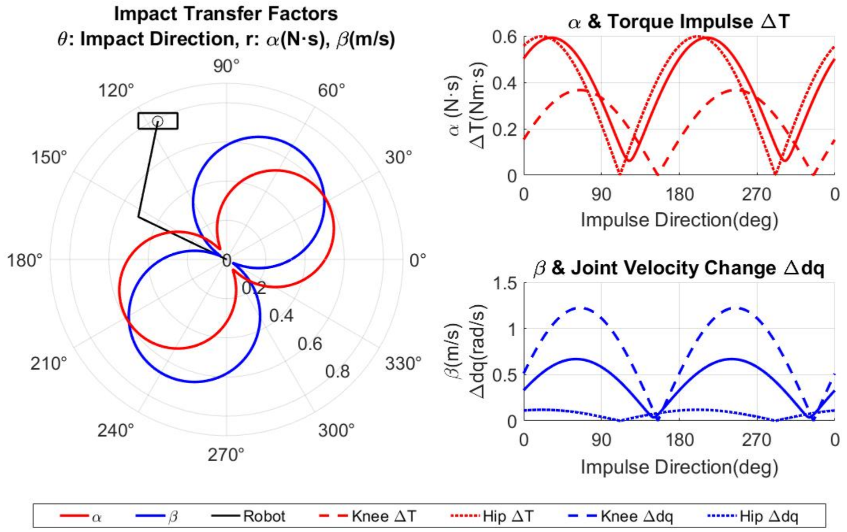

(b) Case 2 simulation results.

Figure 3.19: The plots of simulation results of a 2DoF robot limb with two different end-effector positions. A polar plot and two linear plots of ITF are generated for each case. Corresponding torque impulse and velocity changes on the joints are also plotted in the linear plots respectively.

in Cartesian coordinates, with the X-axis representing the direction of the unit impulses. In the second plot, the Y-axis represents the magnitudes of the corresponding IFTF and the torque impulses felt by the joints; in the third plot, the Y-axis represents the magnitudes of the corresponding IVTF and the velocity changes on the joints.

To better understand the meaning and application of the ITF we have introduced in this paper, we refer to the plots of the second simulated case as shown in Fig. 3.19b, and we assume the robot is capable of zero-latency sensing of instantaneous joint torque and velocity changes with identical sensing resolution. By observing the polar plot, we notice for this configuration, if the impact loaded on the tip of the tibia link is along the direction of 0° or 180°, the magnitude of α is significantly bigger than that of β, meaning that if impacts along the direction of 0° or 180° were to be detected, joint torque signal can more easily be sensed over a joint velocity signal. There are also intervals where the magnitude of β is significantly bigger than that of α, thus joint velocity signal is preferable over torque signal for impact detection, such as when the impact is loaded along the direction of 60° or 240°.

As aforementioned, these ITF can be used for robot joint protection as well. The components to be protected are gears in the actuators, force-torque sensors, and other impact sensitive components on the joints rather than the structural components. It is safe to assume that the bigger the impulsive torque loaded onto the impact sensitive components, the higher the risk of those components being damaged. The most direct evaluation reference for the risk of damaging the components under impacts is the impulsive torque loaded on each joints, however, deriving the impulsive load on each joint often times is not as straightforward, neither can one gain any overall evaluation for the whole robot limb.

However, the IFTF, as introduced in this paper, can be an easy to use metric to evaluate the risk of damaging the joints upon impacts from a holistic system point of view. For example, Fig. 3.19b shows how α can holistically represent the impacts being transferred to both joints. As can be seen in the linear plots, α is generally coincident with the hip torque impulse ΔT, which is generally the joint with significantly bigger torque impulse loading. When α is high, so is the loading on the hip joint. On the contrary, when no load is applied on the hip or when the load is less than that on the knee (e.g. directions 90~135° or 270~315°), α does not completely become zero, as it still captures the potential damage due to the loading on the knee. This behavior of α can be witnessed in other configurations as well. Thus, it is safe to claim that α can be a very reliable reference to evaluate the risk of breaking any joint on a robot limb under impacts with known direction.

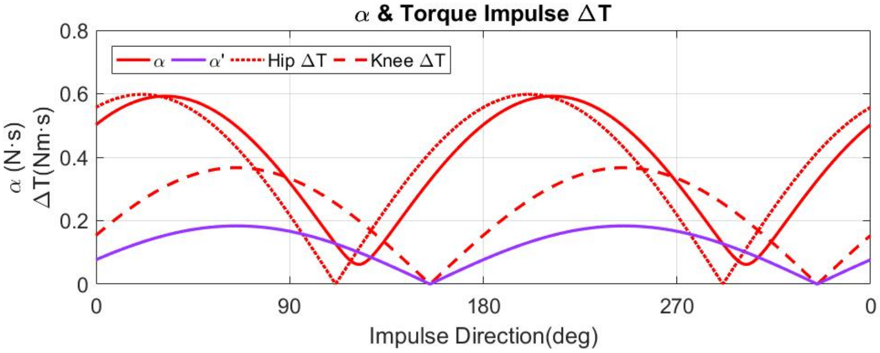

Figure 3.20: The linear plot of α' with the knee joint as the joint of interest. The robot configuration is same as Fig. 3.19b. Previous simulation results shown for comparison.

Additionally, if it is desirable to analyze specific joints rather than collectively, a useful and interesting feature with ITF is that one can simply set the motor inertia of the non-interested joints to zero to create a new joint motor inertia matrix ${d_{mot}}'$, and use ${K_F}'$ in

(3.89) to calculate the IFTF.

$$K_F{}' = J_t d_{mot}{}' D_2 J_s{}^T \tag{3.89}$$

For example, if we are only concerned about the knee joint in the running example, we can then calculate the new IFTF α' with the corresponding $K_F{}'$. α' is plotted in Fig. 3.20 for comparison with the previous plot of α and torque impulse ΔT in Fig. 3.19b. It is clear that α' is only coincident with knee joint torque impulse and can be used as a reliable reference to evaluate the risk of damaging the specific joint (in this case the knee joint) under impacts.

3.3.3.3 Experiments On Validating ITF

To verify our theoretical results, and more importantly the practicality of such an approach, we conduct a preliminary experiment on a physical robot. While it would be ideal to investigate both ITF, it is nearly impossible to measure force impulse caused by a collision, as the signal is instantaneous, which none of the commercially available force/torque sensors are capable of accurately capturing. Also since K_V and K_F are interconnected by d_{mot}, which is only dependant on the physical property of the system, if experimental results validate one of the two ITFs, the other one is simultaneously validated. Thus our investigation only focuses on verifying the IVTF.

The platform we test our theory on is NABi-2 [72]. It is a bipedal robot that has 6 degrees-of-freedom and uses proprioceptive actuators for current-based force control [76]. The actuator's on-board motor controller also allows precise position control based off a 14-bit absolute encoder. Because NABi-2 has two consecutive pitch joints located at the hip and the knee, with the actuation at the knee done through a belt by an actuator located at the hip, once the hip yaw joint is locked in position, the leg can be taken as a 2 DoF planar robot and is a good physical representation of the simulated system.

Consequently, our experimental setup is as follows. We lay NABi-2 on its side and initially command one leg to a desired position in the X-Y plane (refer to Fig. 3.21 for the convention). Then, aside from the hip yaw motor, the remaining two pitch motors are torqued off. This setup is different to simply vertically uplifting NABi-2 from its usual standing posture because it eliminates the torques that need to be applied to maintain the posture which would otherwise be disturbed by gravity. At this given end-effector position, a ball that is tied by a string to a pivot point directly vertical of the end-effector is released. This ensures that the ball will consistently hit the end-effector with a velocity vector pointing towards the center of the end-effector, causing a head-on collision. The release point (i.e. distance from the ground) is maintained a constant height to ensure consistency in the magnitude of impulse that is generated by the

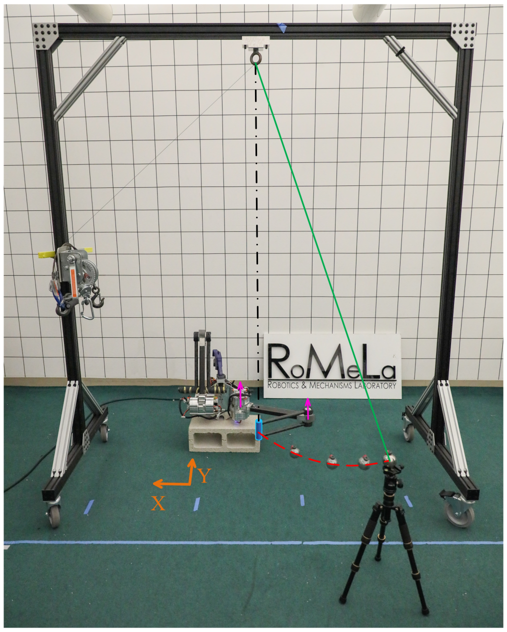

Figure 3.21: Experimental setup with NABi-2. A ball that is tied by a string to a pivot point located directly vertical of the end-effector is released from a constant height to generate constant collision on the end-effector. The end-effector is highlighted in blue, the string is highlighted in green, the trajectory of the ball is marked with a red dashed curve, and the joints on the robot are indicated with magenta arrows.

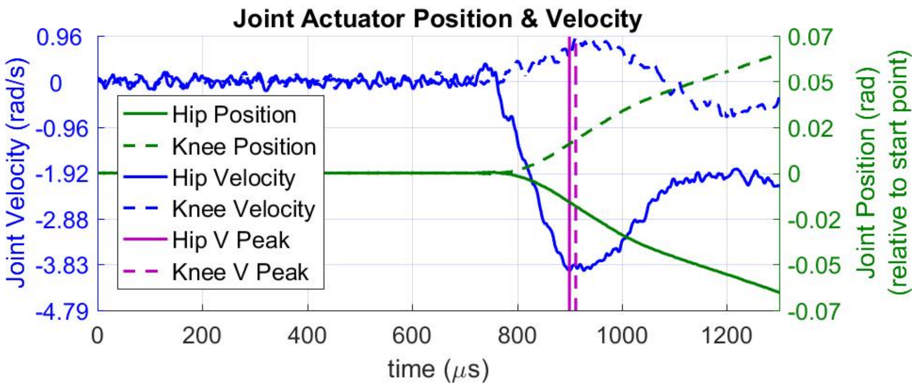

Figure 3.22: Sample position and velocity data recorded using LabVIEW. The magenta vertical lines indicate the peaks of the joint velocities.

collision, and impulse with this magnitude is defined to be a 'unit impulse.' The angle the ball hits the end-effector is distributed within the range that the ball can swing down and make a head-on contact without colliding into anything else on its way. The exact angle at impact is identified afterwards in image post-processing. From approximately the release of the ball from a given height to post-impact, a LabVIEW program records the encoder values as well as the joint velocity values calculated using finite differences with a low-pass filter at 22,000 Hz and 4,000 Hz respectively. A camera mounted adjacent to the pivot and facing towards the end-effector records the impact. These data are then saved for post-processing. Fig. 3.21 shows the experimental setup with annotations of the robot, the pivot point, and the ball, while Fig. 3.22 shows a sample encoder and velocity stream.

With the collected data, which includes the video stream of the impact and the encoder and velocity values recorded from LabVIEW, post-processing of the data is done as a pre-processing step for verifying the IVTF. To begin with, we assume that the body of our robot is in parallel with what is considered 0° and therefore, the angle the ball strikes the end-effector is found by measuring the angle difference between the body and the ball striking the end-effector angle.

The instantaneous velocity to calculate the IVTF is extrapolated from the recorded velocity data under some assumptions. Using the data shown in Fig. 3.22 as an example, we expect a change in both the actuator's position and velocity signals simultaneously. However, it is noticeable that the hip actuator moves before the knee motor, albeit a small amount. Our experience with the platform suggests that because the knee motor is belt-driven by an actuator located at the hip and due to the non-collocation of the encoder, such an offset is created. However, as observable in the graph, this delay is ~$100\mu s$, which we assume to be negligible. Also, the time it takes to reach peak velocity for the different configurations is ~$1ms$. This quick peaking can be sensed because of the type of actuators that are used in NABi-2 and since the time is small, we assume $\Delta\dot{q} = \text{sgn}(\dot{q})\text{max}(|\dot{q}|)$.

Additionally, because of the belt transmission, the actual impact at the knee is not fully captured by the actuator, as the belt absorbs a significant portion of the impact. According to [42] and [16], as well as from our experiences, the impulsive velocity change on the actuator for the knee joint should be adjusted with a correction factor. We found this value to be 2.

For the constants used to calculate the ITF, the values from the CAD model are used for the inertial properties of the robot limb as well as the reflective inertia of the actuators. While these could also be considered as estimates, they have been empirically proven to be trustworthy through our experience with controlling NABi-2 using these parameters. Regarding the magnitude of the impact, although the collisions during our experiments are controlled to be constant, the actual value of the 'unit impact' can never be accurately calculated. However, because the magnitude of the impact does not change the shape of the ITF plot, but only its scale, it is theoretically reasonable to find it through simulation and numerical analysis.

This is done in simulation by varying the impact magnitude applied at the planar NABi-2 leg. For each impact magnitude, a standard deviation is found using the simulated end-effector velocity change and the samples from the test results. The impact magnitude that yields the smallest standard deviation is taken as the actual impact magnitude. Using this impact magnitude as a constant along with the angles and their corresponding instantaneous change in velocities, the IVTF is found.

Plotting the simulated ITF alongside the experimental data as seen in Fig. 3.23 shows that the behavior the simulation predicts qualitatively resembles that of the experiment. To quantitatively assess the experimental data, we also plot the 65% Confidence Interval, which then, most of our data points fall inside. This gives us further belief that the theory behind ITF is valid and simply by simulation, we can obtain a good idea of the magnitude of the transferred impacts.

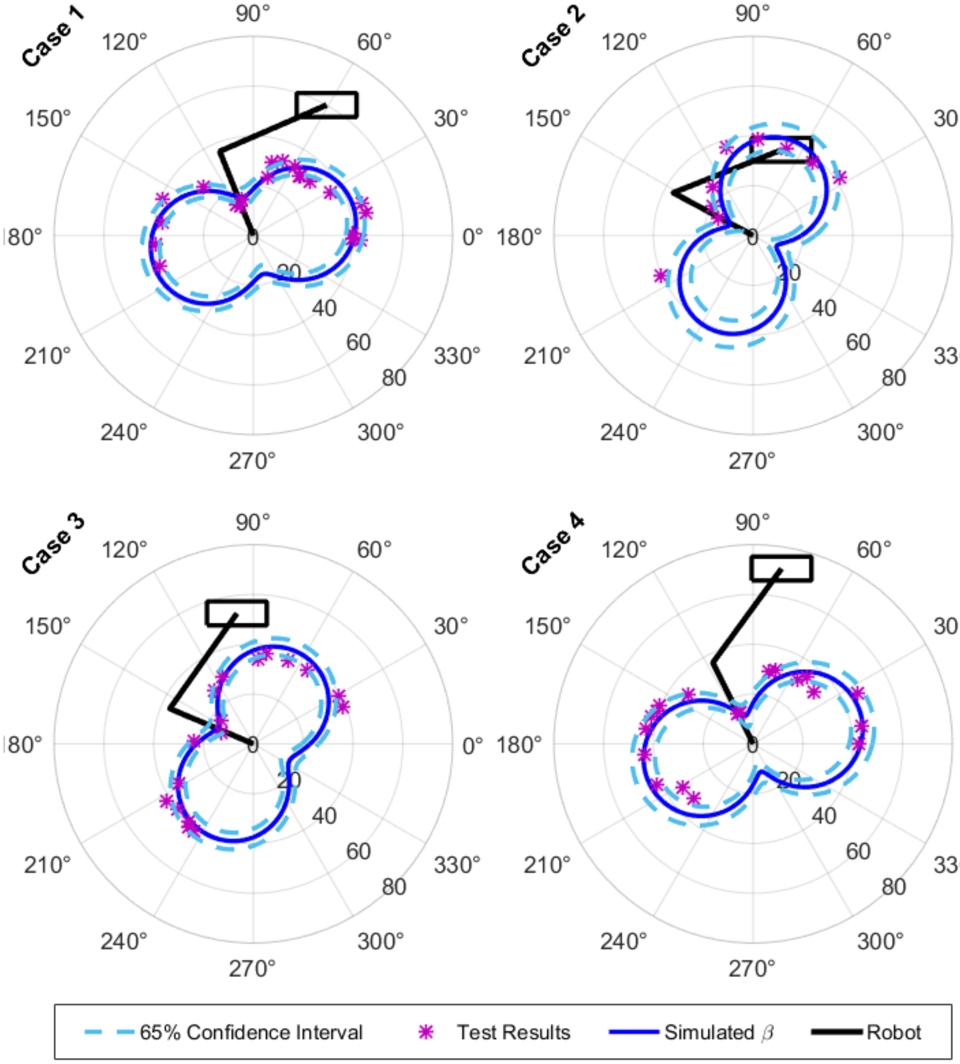

Figure 3.23: Most experimental data falls within the 65% Confidence Interval, which verifies the validity of using ITF on physical platforms. The unit for plot radius is m/s.

CHAPTER 4

Experimental Work And Results

4.1 Development of Prioproceptive Quasi-Direct Drive Actuators

The Proprioception Actuator modules developed in RoMeLa are called the BEAR modules, Back-drivable Electromagnetic Actuators for Robots. Currently there are two versions of BEAR developed and widely used in RoMeLa, a lite version called the Kola BEAR and a professional version called the Panda BEAR. There is also an ultimate version being developed, called the Kodiak BEAR. Both Panda and Koala feature liquid cooling for the motor windings to push the peak performance of the actuator to the maximum. Two sub-versions of Koala BEAR are developed, and the only difference is the gear reduction ratio: a low reduction ratio version called Koala-S for higher speed applications and a high reduction ratio version called Koala-T for higher torque applications. The performance data of PAnda and Koala BEAR modules are as shown in Table.4.1.

The Panda BEAR was the first module in the BEAR actuator family, it was designed and built by Taoyuanmin (”Tym”) Zhu at RoMeLa. Panda BEAR has balanced performance, weight and size. It is developed for relatively general applications, such as legged mobile robotic platforms and light robotic manipulator arms. The Kodiak BEAR is a scaled up

Table 4.1: BEAR modules Performance Specsheet.

Module	Size	Weight	Max Speed @24V	Peak Torque	Continuous Torque	
					Air Cool	Liquid Cool
Koala-S	94x94x48mm	0.275kg	570RPM	12Nm	8Nm	3.75Nm
Koala-T	94x94x48mm	0.275kg	380RPM	16Nm	10.7Nm	5Nm
Panda	100x100x45mm	0.75kg	240RPM	30Nm	20Nm	10Nm

version from Panda BEAR, and it is a proof of concept to seek the feasibility of using Proprioceptive Actuators on full-size humanoid robots. Improved version of Kodiak BEAR will be applied onto the amazing full-size humanoid robot ARTEMIS (Advanced Robotic Technology for Enhanced Mobility and Improved Stability).

The smaller version of the actuators, the Koala BEAR, is developed as part of the work covered in this dissertation. Koala BEAR is developed for applications where smaller and compact yet dynamic actuators with force sensing and control capability are needed, such as robotic hands, simple tabletop robotic arms and small legged robotic platforms. To seek for the optimal balance within torque, speed and impact mitigation capability, two sub-versions of Koala BEAR are developed, differentiating on the gear reduction ratio. The concept and feasibility of Koala BEAR was proven by a preliminary actuator design applied on DAnTE V1, which is presented in detail in Section.4.2.1. Prototypes of Koala BEAR are then designed and built, and are being tested on DAnTE V2 (Section.4.2.2) and a small humanoid robot BRUCE. (Section.4.3.3)

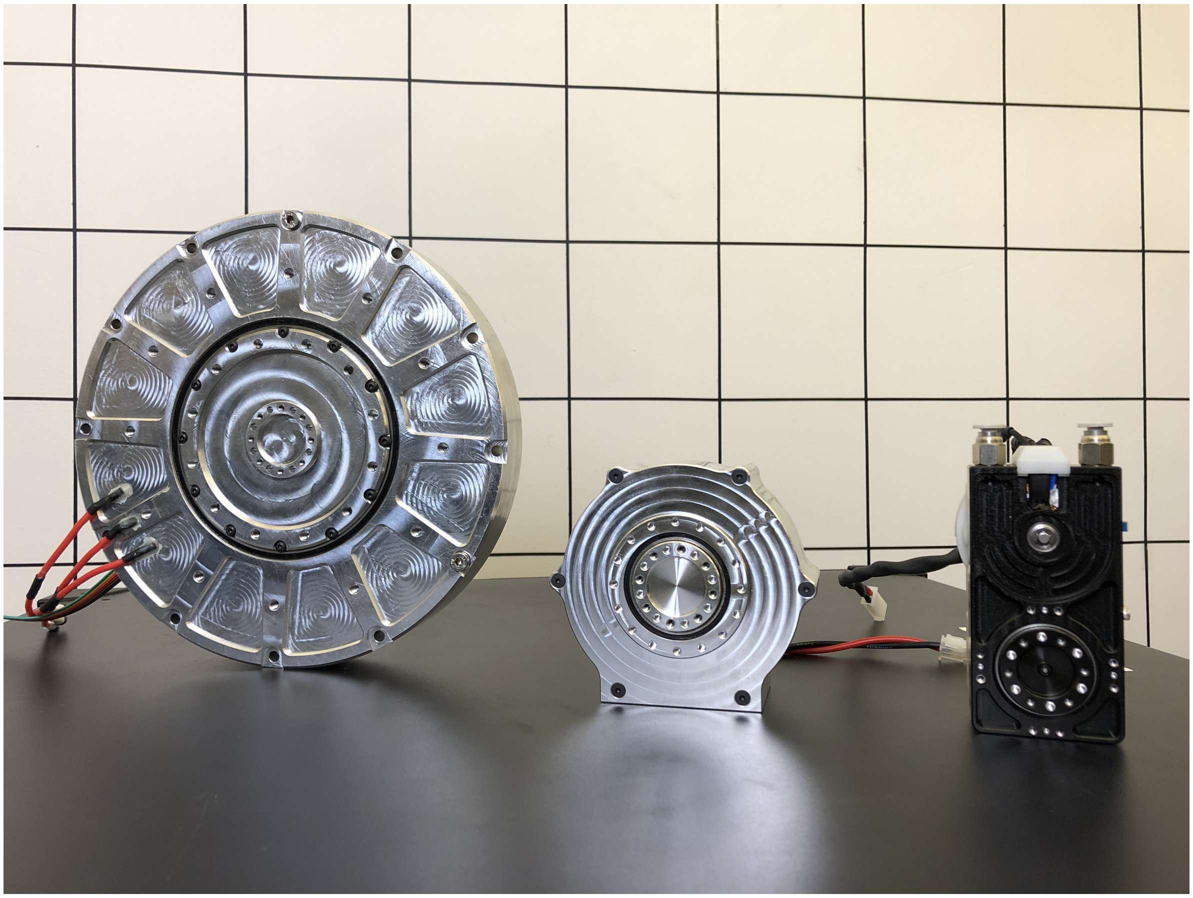

Figure 4.1: The BEAR modules

4.1.1 Panda BEAR

Panda BEAR(Fig.4.2a) is composed by a T-Motor U8 BLDC motor(Fig.4.2b) with motor speed constant $K_V = 100$ RPM/V, and a planetary gearbox with a gear reduction ratio of 10:1. Figure.4.3 is an exploded view of Panda BEAR.

The actuator has a very compact all-in-one packaging, featuring great balance of size, weight and power. To maximize the performance of the actuator under extreme condition, liquid cooling feature is added onto the motor housing and the effectiveness of liquid cooling has been studied in detail by Tym, etc. [] The liquid cooling feature enables the actuator to

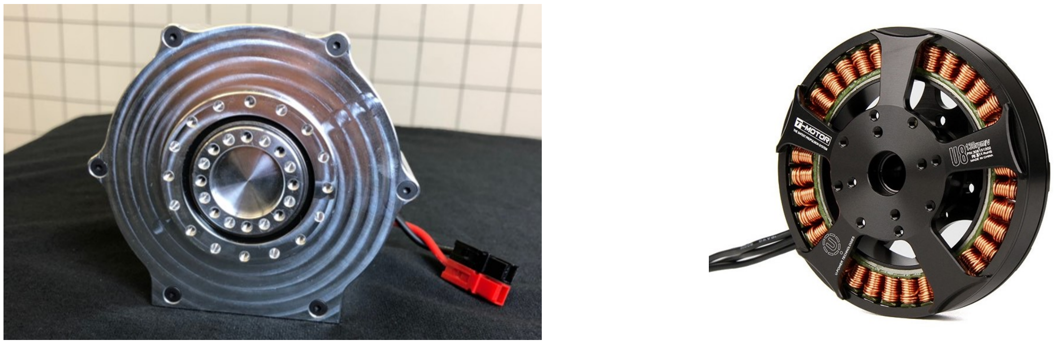

(a) Panda BEAR

(b) T-motor U8

Figure 4.2: Panda BEAR and T-motor U8

run cooler under continuous working condition and work at peak torque for longer time and more frequently.

Panda BEAR modules are applied to the dynamic legged robot platforms NABi-2 and ALPHRED-2, which are respectively presented in detail in Section.4.3.1 and Section.4.3.2.

4.1.2 Koala BEAR

After the success of applying Panda BEAR onto legged robots, there emerges a demand for a new design of Proprioceptive Actuator module that is suitable for smaller legged robot platforms such as a kid size biped robot, as well as other small robotic platforms such as end-effectors. This new design needs to be even more compact, being smaller in size and lighter in weight, yet significantly higher in torque density and at least equivalently dynamic as Panda BEAR presents. With all above requirements to satisfy, Koala BEAR (Fig.4.4) is developed.

Unlike most Proprioceptive Actuators as introduced in Section.2.3.2, Koala BEAR has a

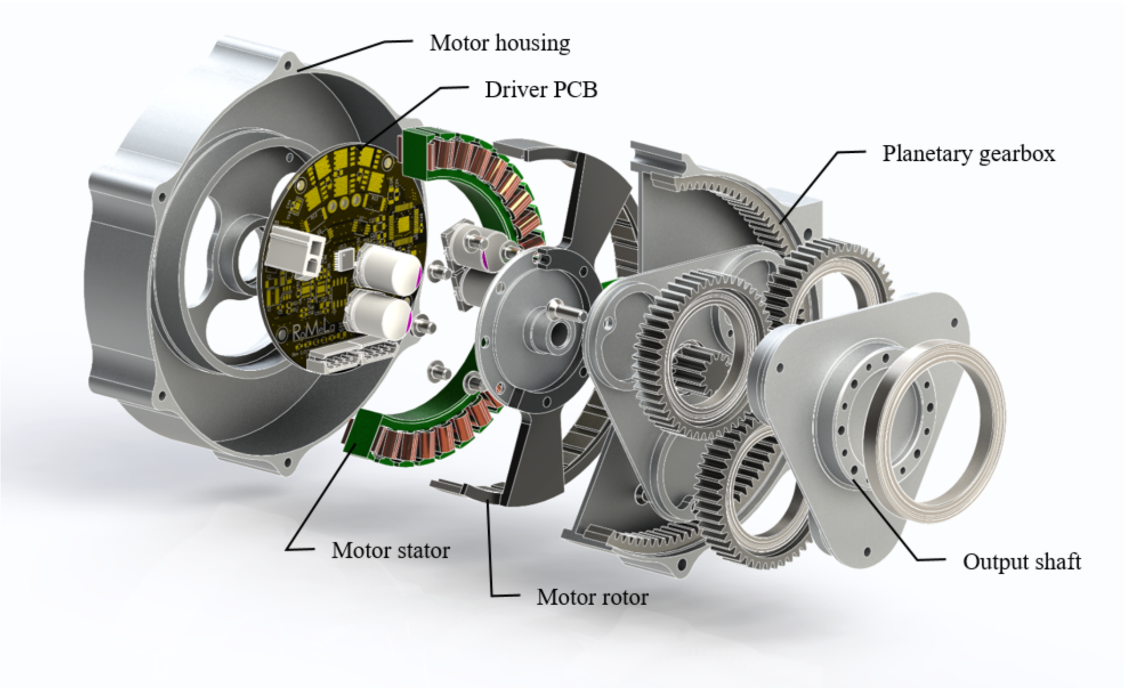

Figure 4.3: Exploded view of Panda BEAR.

Figure 4.4: Koala BEAR actuator module.

Figure 4.5: T-Motor brushless motor Untigravity 4006.

compact rectangular shape, instead of centro-symmetric shapes. This allows Koala BEAR to remain a slim figure in its axial direction, making it very friendly to the targeted applications.

To validate the feasibility of the idea behind Koala BEAR, its concept was first tested with a quick prototype fabricated with 3D printing, and the prototype was applied onto a 3-finger robotic end-effector called DAnTE-1 (Refer to Section.4.2.1 for more details).

Based on the experimental results of DAnTE-1, the BLDC motor in Koala BEAR is chosen to be T-motor 4006 (Fig.4.5) with motor speed constant $K_V = 380$ RPM/Volt among all commercially available BLDC motors. By combining this motor With a low reduction ration transmission, the actuator is estimated to possess the maximum torque and speed capability that fits the need of a broad range of small size robotic systems. To gain adequate output torque, the gear ration of Koala BEAR is designed to be higher than what a planetary gearing system can provide without increasing the diameter of the ring gear to be significantly bigger than that of the BLDC motor. Benefited by the rectangular housing, a low-cost 2-stage transmission becomes possible. As shown in the exploded view of Koala BEAR module in Figure.4.6, the transmission of Koala BEAR is composed by a planetary gear box at the output and a belt transmission with a set timing pulleys from the BLDC motor. The pulleys are plastic made by 3D printing, combined with aluminum inserts at the bore to increase their strength and transmission reliability. With this 2-stage transmission and especially the pulley set that can be rapidly fabricated, Koala BEAR is also a pioneer that can be used to search for an approximate boundary of speed reduction ratio for a transmission to qualify as transparent, or quasi-transparent regarding to the application of Proprioceptive Quasi-Direct Drive actuators. The reduction ratio of the Planetary gearbox on Koala is 9:1, and by combining pulleys with different number of teeth, the speed reduction ratio from the pulley set can vary from 1:1 to 3:1, resulting in a overall speed reduction ratio ranging from 9:1 to 27:1. However, from the experience of Panda BEAR and the prototype Koala BEAR on DAnTE 1, it is safe to claim that the boundary of speed reduction ratio for a transmission

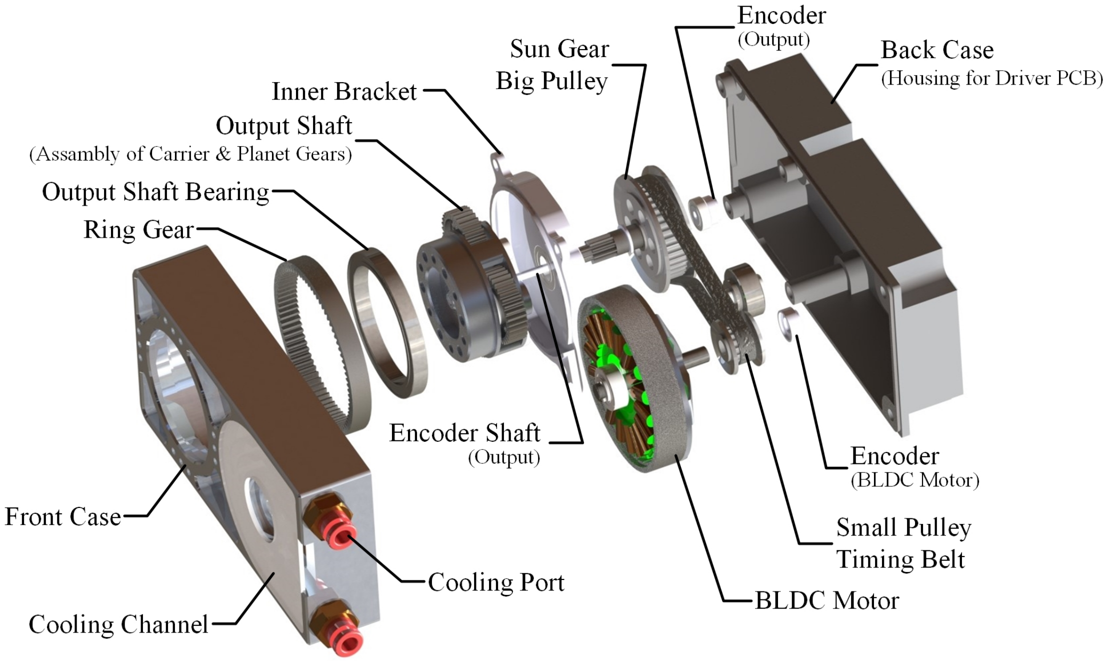

Figure 4.6: Exploded view of Koala BEAR module.

to qualify as transparent, or quasi-transparent is over 9:1.

Currently, two versions of Koala BEAR with distinguishing speed reduction ratio are being tested on various robotic systems: a speed version with a speed reduction ratio of 18:1 and a torque version with a speed reduction ratio of 24:1.

4.2 Experiments with End-effectors

Manipulators are an essential aspect of a robot's ability to interface with their working environments in order to finish their tasks. Often times these working environments are designed for human beings. Thus, for robots to finish the tasks they are designed for, robotic hands with biomimetic fingers are almost always the preferred design, such as the The DLR robotic hand[21] and the the ADROIT robotic hand[34]. These designs attempt to mimic human fingers using full actuation, where each joint is independently actuated and controlled, resulting in redundant actuation and very complicated, heavy, and bulky systems. However, many simple grasping and manipulation tasks don't require full actuation, meaning these complex hands are unnecessarily increasing the payload of the arm. As such, fully actuated robotic hands are conventionally not preferred, and robotic hands such as the tendon driven SDM hand by Dollar[15] and the four-bar linkage driven robotic grasping hand by Gosselin[35] which feature fewer fingers and under actuated finger designs have been developed. However, as mentioned in Section.3.2.1, these under-actuated systems all posses uncertainties in their fingers' trajectories. This problem can be solved by applying carefully designed mechanical intelligence following the theory of Potential Energy Flow in underactuated systems.

Further, implementing force control on robotic hands to perform dexterous grasping and manipulation has also been a difficult problem, especially for fragile objects. Many research groups have done remarkable research on force controlled manipulators by applying tactile sensors[61], artificial skin[69] or force/torque (FT) sensors on finger [36] or wrist [53] joints. However, even though these methods performed admirably for the tasks they were designed for, the sensor systems used were always difficult to fabricate or expensive, and required large computational resources to support a high control frequency that was essential for the success of these types of robotic hand systems. On top of that, these systems usually performed poorly when dealing with external impulses or when approaching a goal object at high speeds, since either the system itself or the goal object would likely be damaged. The BEAR modules developed in RoMeLa show the potential of addressing these problems by providing inherent compliance and proprioceptive force sensing.

DAnTE(Dynamic Anthropomorphic Tactile End-effector) is a brand new force controlled under actuated robotic hand with mechanical intelligence and proprioceptive compliant actuation developed to validate the effectiveness of the Potential Energy Flow theory and feasibility of improving the capability of robotic hands with Proprioceptive Actuators. DAnTE has fingers with simplified biomimetic design which take the advantages of the human finger tendon drive system while still being under actuated to reduce hardware and software complexities. The finger systems on DAnTE possess carefully designed mechanical intelligence such that the partition of the finger's trajectory from the under actuated DoF is controlled by the mechanical intelligence. By taking advantage of the high resolution current sensing and responsive control on the quasi-direct drive actuation system, we are able to achieve fast and dexterous force controlled grasping and manipulation without using any FT sensor. This actuation system also provides intrinsic compliance in the finger joints, providing the robotic hand system with excellent performance when it comes to fragile objects or impulses.

There have been two versions of DAnTE developed, and they are presented in detail in the following sections.

4.2.1 DAnTE-1

4.2.1.1 Design of DAnTE-1

DAnTE contains a hand assembly and an actuation assembly. The hand assembly is composed by a palm assembly and three fingers, while the actuation assembly is simply composed by three identical actuation assemblies, with each finger on the hand independently driven by an actuator. Fig.4.7 is an overview of the system, and the mechanical design is described in detail in the following sections.

The overall system specifications of DAnTE is as shown in table.4.2 Note that the maximum fingertip force is limited to 30N because this prototype is FDM 3D printed with ABS, and a force exceeding this maximum will damage the internal tendon structure.

Palm There are three fingers mounted axisymmetrically on the palm, with two of them able to rotate along their own central axis so that different relative positions of the three fingers can be achieved. These two fingers are coupled by gears and are driven by a single servo so that they always mirror each other. The palm also acts as the housing for a servo and the corresponding powertrain for finger orientation actuation. The finger orientation

Table 4.2: Specifications of DAnTE robotic hand platform.

Parameters	Value
Weight	1.5 kg
Overall Length w/o Finger	26 cm
Finger Length	90 mm
Object Diameter	0 120 mm
Max. Fingertip Force	30 N
Min. Retraction Time	300 ms

actuation powertrain is as shown in Fig.4.9. Both actuated fingers have a 90 degree range of motion along their own central axis, forming all grasping gestures as shown in Fig.4.10.

Simplified Biomimetic Finger To better illustrate the design of the biomimetic finger, it's necessary to briefly review the functional anatomy of the extensor and flexor mechanism of human finger. As shown in Fig.4.11[10], tendon movements marked by the black arrows (such as retraction of EDC & EIP tendon) cause the finger extension, while tendon movements marked by the red arrows (such as retraction of the FDS tendon) cause finger flexion. The retraction of FDP tendon causes the distal and middle phalanxes to bend, the retraction of FDS tendon causes the middle phalanx to bend, and the flexion of the proximal phalanx is done by the retraction of the extensor hood.

Clearly, a human finger is a complex fully actuated mechanism, and implementing a

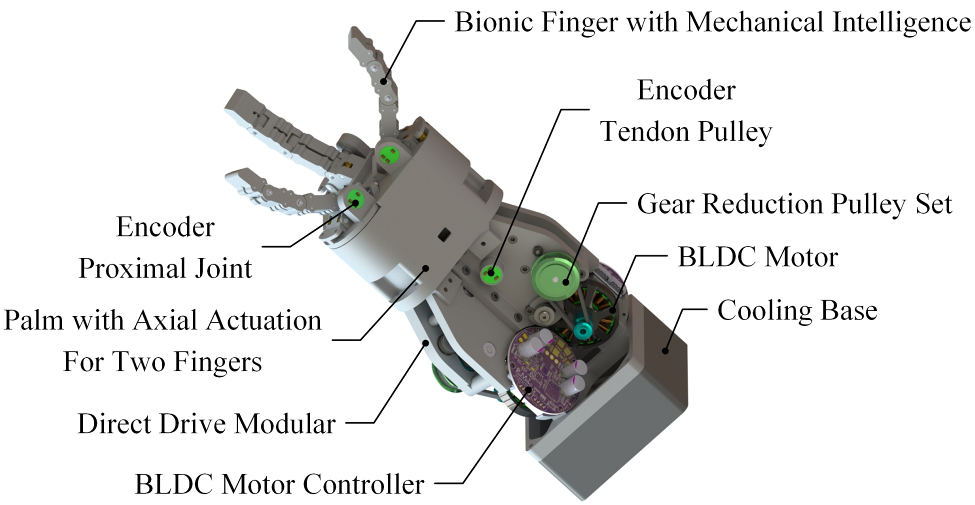

Figure 4.7: Structure of the end-effector system. The system contains a hand assembly and an actuation assembly. Details of the two assemblies are shown above.

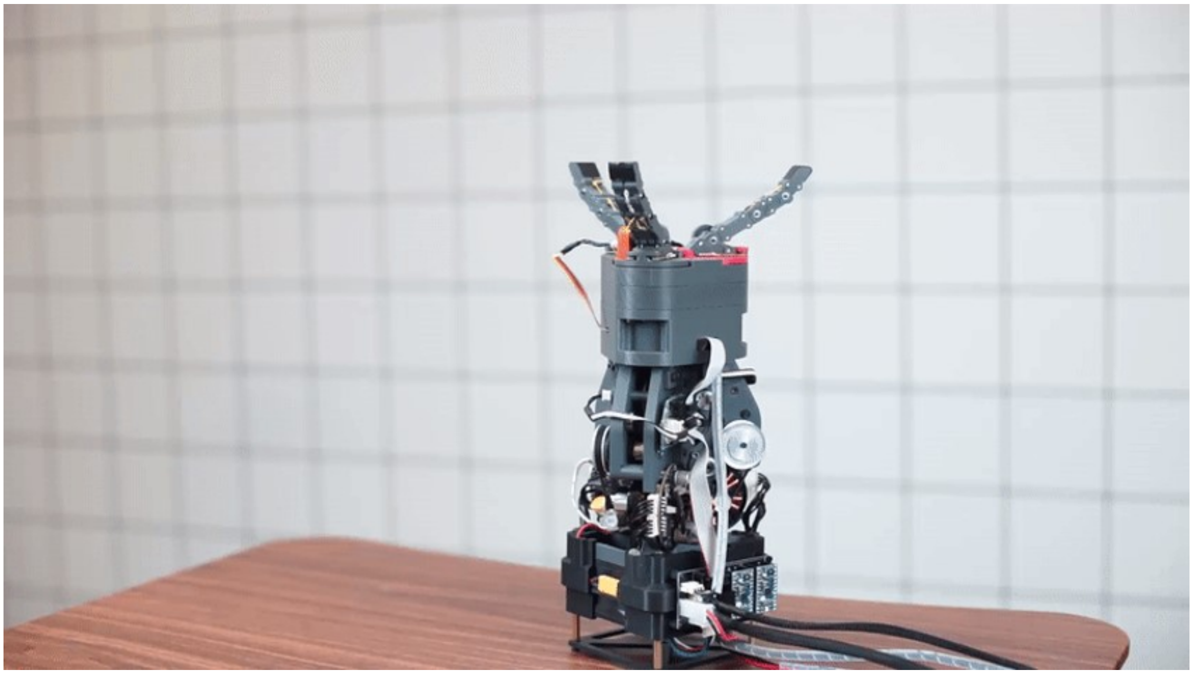

Figure 4.8: The DAnTE system

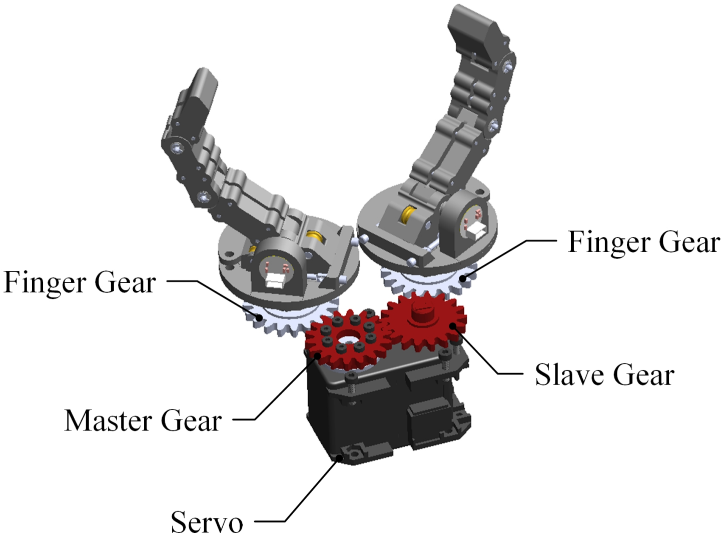

Figure 4.9: Finger axial rotation powertrain contained in the palm.

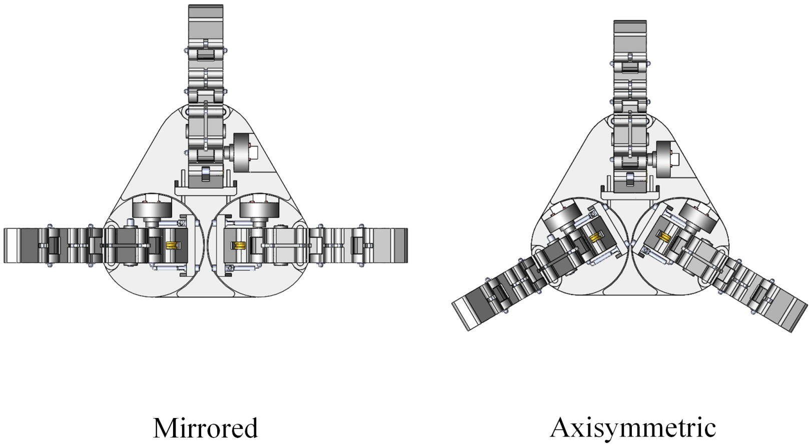

Figure 4.10: The three basic gestures DAnTE can form for grasping tasks. The gestures are formed by changing the angular position of the two actuated fingers. The parallel configuration is preferred for prismatic objects while the asymmetric (tripod) gesture is often used for circular objects. The mirrored gesture is good for pinching operations.

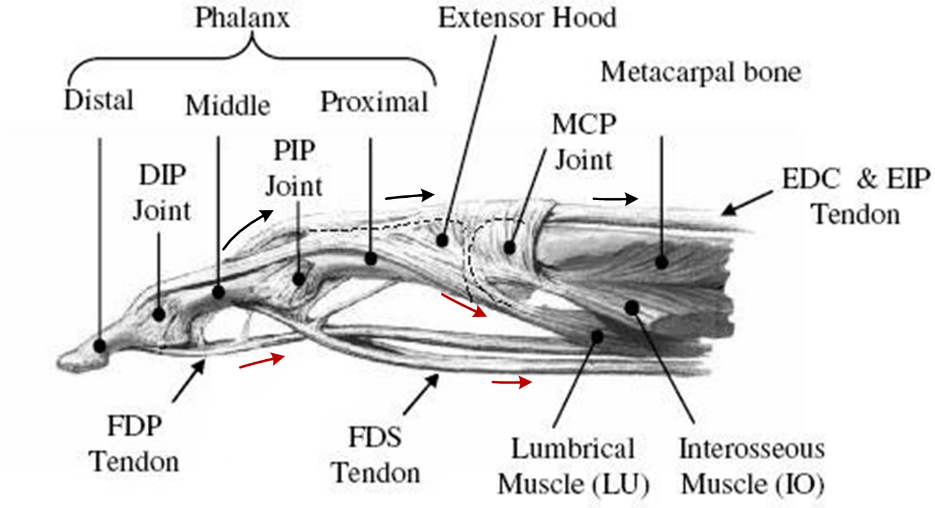

Figure 4.11: Human finger tendon system mechanical structure. tendon movements marked by the black arrows cause the finger extension, while tendon movements marked by the red arrows cause finger flexion.

robotic hand with the same finger design may not be the best approach as it would require numerous actuators, a complicated tendon system, and a complex controller. The resulting platform would likely be cumbersome and lack robustness. Instead, we would like to adopt a simplified version of a human finger for our robotic hand.

The objective of DAnTE is to mainly do gripping and some simple manipulation, thus high agility on the fingers which would require the finger to be fully actuated is not necessary. There are three rotational DoF in a human finger, respectively on the DIP, PIP and MCP joint. Due to the coupling between the FDP tendon and the middle phalanx, in most cases, the distal and middle phalanxes move correspondingly in free-load motions. In fact, in most grasping motions except fingertip grasping, corresponded bending on these two phalanxes is preferred for better grasping. Thus, we can simplify the coupling between the FDP tendon and the middle phalanx with a passive reaction coupling tendon, as the yellow tendon shown in Fig.4.12a. With this coupling tendon, the distal phalanx always bends together with the middle phalanx. The remaining two DoF are actuated by one actuated flexor tendon attached to the middle phalanx, as the red tendon shown in Fig.4.12a. The tendon goes under two tendon guide pins that are fixed on the proximal phalanx. The actuated flexor tendon drives both the middle phalanx and the proximal phalanx by directly pulling the middle phalanx and using the normal force on the tendon guide pins to drive the proximal phalanx. Since the main tasks of this grasper are about grasping and manipulation, it is not necessary for the extension motions of the fingers to be actuated, thus elastic members are used as extensor tendons. The extensor tendons are arranged to oppose the flexor tendons, with an elastic extensor tendon linking the distal and middle phalanx over the DIP joint to counteract the distal phalanx bending relative to the middle phalanx, keeping the passive reaction coupling tendon in tension. The other extensor tendon is the main extensor tendon, and is a rigid string attached to the back of the middle phalanx, going under a guide pin on the back of the proximal phalanx. It is then pulled by a tensile spring, as the red tendon shown in Fig.4.12b. The main extensor tendon recovers the middle and proximal phalanx from bending, keeping the actuated flexor tendon in tension.

Actuation Assembly As mentioned before, the actuation assembly contains three direct drive actuation modules, with each of them driving one finger. The concept of our direct drive actuation module is to combine a brushless torque motor with very low gear reduction ratio. Fig.4.13 shows the main components in the actuator sub-assembly with all the structural parts and bearings hidden. T-Motor Antigravity 4004 brushless DC motors are employed,

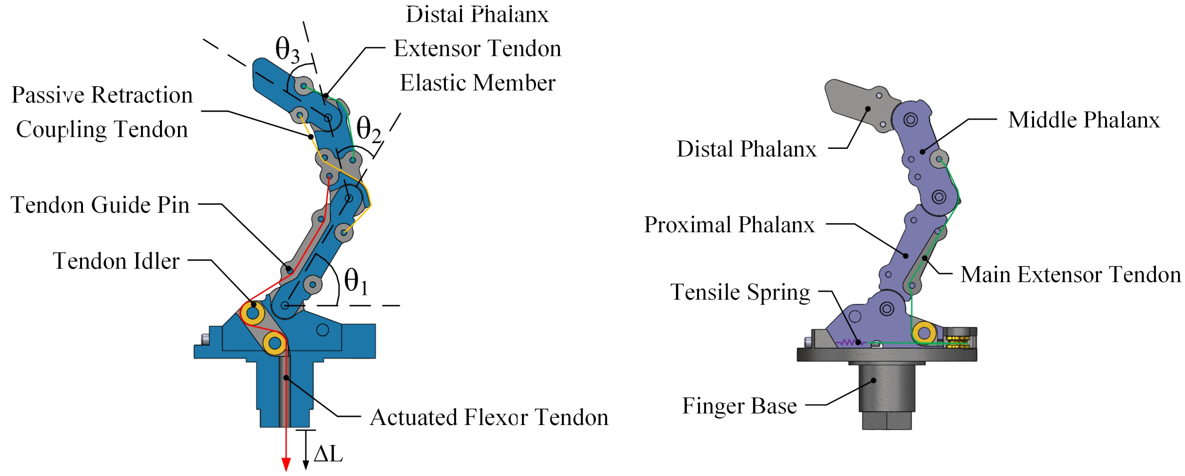

(a) Flexor (b) Extensor

Figure 4.12: Tendon system in the under actuated finger design. Figure(a) shows the mechanism of the flexor tendons (in red), while figure(b) shows the mechanism of the extensor tendons (in green).

driving a two-step speed reduction transmission composed of two sets of timing pulleys, providing a total reduction ratio of 8.6:1. Each timing belt is associated with an adjustable tensioner. A tendon pulley is attached at the end of the powertrain to drive the tendon, and a 12-bit absolute encoder is also attached to the shaft of this tendon pulley so that the length of pulled part on the tendon can be precisely acquired. The BLDC motor is controlled by a motor controller developed and fabricated in house.

4.2.1.2 Kinematics of DAnTE-1

The same system was first introduced in a previous paper[74], where the kinematics of the tendon system was not illustrated. In this section we will go over the derivation of the kinematics of the tendon driven finger system and this will make the introduction of the

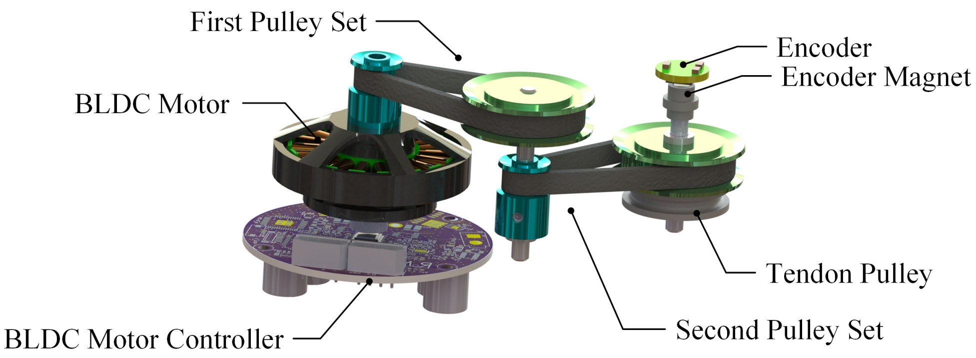

Figure 4.13: Structure of a actuation assembly. It is composed by a BLDC motor and a low reduction-ratio transmission that contains two stages of pulley sets.

system and the following illustration of the mechanical intelligence embedded in the system more comprehensive.

As mentioned in the previous sections, there is an encoder on the tendon pulley shaft reading the rotational position of the tendon pulley θ_0, which is directly related to the length of tendon being pulled out as:

$$L_p(\theta_0) = R_{pulley}\theta_0 \tag{4.1}$$

The same type of encoder is also attached to the proximal joint of the finger to get the position of the proximal phalanx on the MCP joint, θ_1. As mentioned before, The distal phalanx is rigidly linked to the proximal phalanx with a rigid tendon through the middle phalanx, so the positions of the distal and proximal phalanx can always be calculated from the data collected from the two encoders.

As marked in Fig. 4.12a, the length of tendon being pulled(L_p) and the angle of the proximal phalanx relative to the palm(θ_1) are needed to calculate the angle of the middle phalanx relative to the proximal phalanx(θ_2). We break up the tendon in the finger into three sections. The first section is the part of the actuated flexor tendon that is across the MCP joint, and it's length is denoted as L_1. The second section is the following part of the tendon that is in the proximal phalanx and it's length is denoted as L_2. The last section is the rest of the actuated flexor tendon which is across the PIP joint, with it's length denoted as L_3.

It's easy to see that L_2 never changes, so we only need to calculate L_1 and L_3. L_1 is solely dependent on θ_1, while L_3 is solely dependent on θ_2. Mark the total length of the tendon in the finger as a constant L_{total}, then we have this relationship:

$$L_{total} = L_p(\theta_0) + L_1(\theta_1) + L_2 + L_3(\theta_2) \tag{4.2}$$

Since L_{total} and L_2 are constants, one can have:

$$\theta_2 = L_3^{-1}(C_1 - L_p(\theta_0) - L_1(\theta_1)) \tag{4.3}$$

where C_1 is a constant.

To calculate θ_2,we begin with derivation of $L_1(\theta_1)$. The tendon geometry for section L_1 is as shown in Fig. 4.14a, and L_1 defines the length of the tendon from point S to point A. Although the result will be less accurate, the radius of the Tendon Guide Pin is so small that we can ignore the geometry of it and treat it as a point. The simplified tendon geometry is as shown in Fig. 4.14b. This simplification significantly reduce the calculation complexity while the error brought in is negligible.

The equation set used to derive L_1 is as follow:

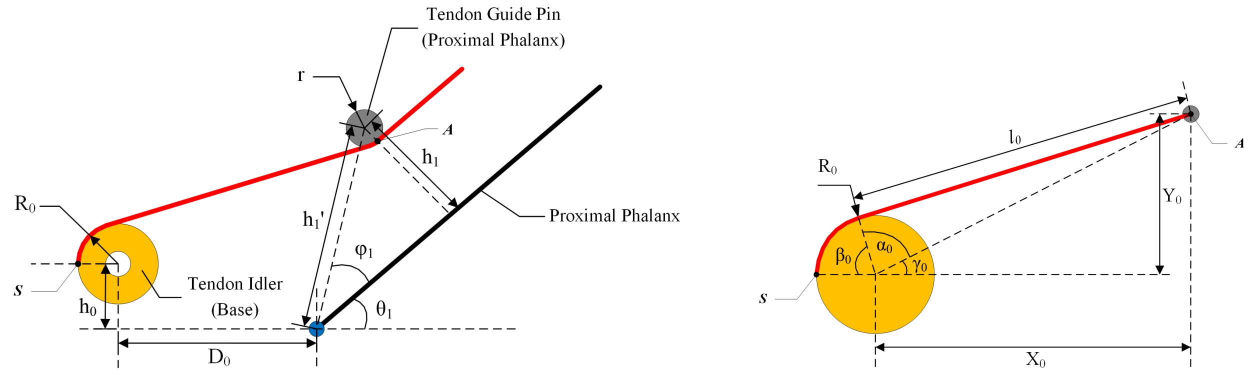

(a) The detailed geometry of the L_1 section of the actuated tendon.

(b) The simplified geometry of the L_1 section of the actuated tendon.

Figure 4.14: The detailed and simplified geometry of the L_1 section of the actuated tendon. This simplification makes the calculation significantly easier with a negligible error in the result as a trade-off.

$$
\begin{cases}
X_0 = D_0 + h_1' cos(\varphi_1 + \theta_1) & \text{(4.4a)} \\
Y_0 = h_1' sin(\varphi_1 + \theta_1) - h_0 & \text{(4.4b)} \\
d_0 = \sqrt{X_0^2 + Y_0^2} & \text{(4.4c)} \\
l_0 = \sqrt{d_0^2 - R_0^2} & \text{(4.4d)} \\
\gamma_0 = tan^{-1}(Y_0/X_0) & \text{(4.4e)} \\
\alpha_0 = cos^{-1}(R_0/d_0) & \text{(4.4f)} \\
\beta_0 = \pi - \alpha_0 - \gamma_0 & \text{(4.4g)} \\
L_1(\theta_1) = R_0\beta_0 + l_0 & \text{(4.4h)}
\end{cases}
$$

φ_1, R_0, h_0, h_1' and D_0 are design constants. The next step is to derive $L_3(\theta_2)$. The tendon geometry is as shown in Fig. 4.15a, and L_1 defines the length of the tendon from point B

to point E. Note that L_2 defines the length of the tendon from point A to point B, which is within the proximal phalanx and is constant. Again we carry the same simplification as previous and ignore the geometry of the pins, the tendon geometry then can be simplified as in Fig. 4.15b.

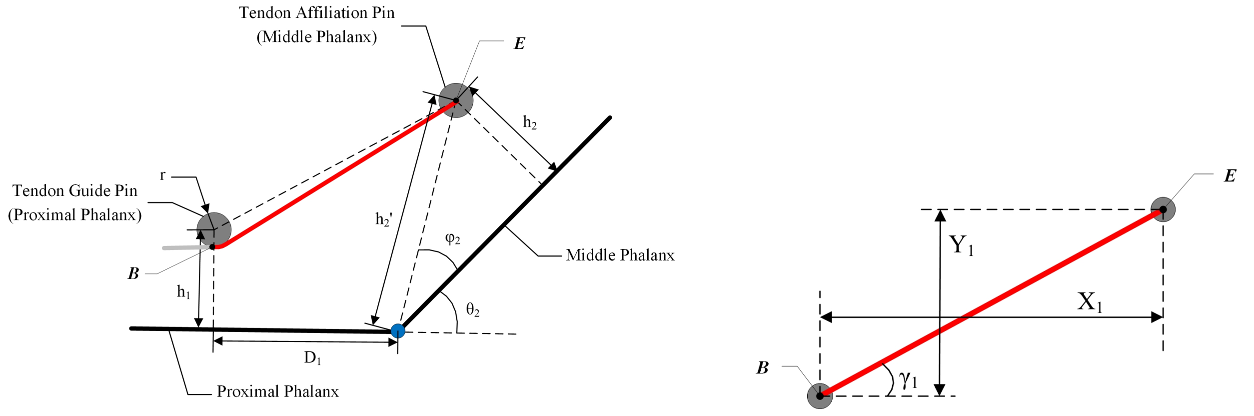

(a) The detailed geometry of the L_3 section of the actuated tendon.

(b) The simplified geometry of the L_3 section of the actuated tendon.

Figure 4.15: The detailed and simplified geometry of the L_3 section of the actuated tendon. This simplification makes the calculation significantly easier with a negligible error in the result as a trade-off.

And the developed set of equations for deriving L_3 are:

$$
\begin{cases}
X_1 = h_2' cos(\varphi_2 + \theta_2) + D_1 & \text{(4.5a)} \\
Y_1 = h_2' sin(\varphi_2 + \theta_2) - h_1 & \text{(4.5b)} \\
L_3(\theta_2) = \sqrt{Y_1 + X_1} & \text{(4.5c)}
\end{cases}
$$

φ_2, h_1, h_2' and D_1 are design constants.

One can now derive θ_2 by combining Eq. 4.1, Eq. 4.3, Eq. 4.4 and Eq. 4.5.

As mentioned in the mechanical design section, the PIP and DIP joints are hard coupled, thus the DIP joint angle θ_3 can be expressed as:

$$\theta_3 = f(\theta_2) \tag{4.6}$$

Though by looking at Fig. 4.12a the passive retraction coupling tendon which is the rigid flexor tendon for the PIP&DIP joint couple may appear to be complicated, Eq. 4.6 is fairly easy to derive. The tendon structure is as shown in Fig. 4.16, with Fig. 4.16a showing the actual tendon geometry and Fig. 4.16b showing the simplified tendon geometry. Again the simplification is same as previous: ignore the geometry of the tendon guide pins.

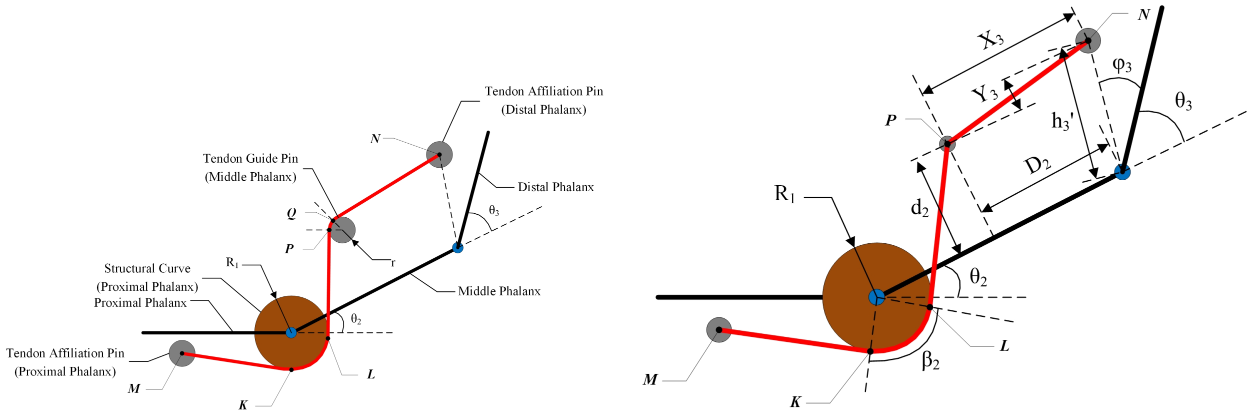

(a) The detailed geometry of the passive retraction coupling tendon.

(b) The simplified geometry of the passive retraction coupling tendon.

Figure 4.16: The detailed and simplified geometry of the passive retraction coupling tendon, which provides the hard coupling of the PIP and the DIP joints.

As shown in Fig. 4.16a, we divide the passive retraction coupling tendon into five sections. The tendon starts from point M, which is the tendon affiliation pin on the proximal phalanx, and ends at point N, which is the tendon affiliation pin on the distal phalanx.

After simplification, the section between point P and Q is ignored, and there now are four sections: section L_{MK}, section L_{KL}, section L_{LP} and section L_{PN}. Let the total length of the tendon be denoted as L_c, the following equation holds:

$$L_c = L_{MK} + L_{KL} + L_{LP} + L_{PN} \tag{4.7}$$

Note that the total length of the tendon is fixed and point K never moves in relative to point M, and point P never moves in relative to point L, thus L_c, L_{MK} and L_{LP} are constant. L_{KL} is solely dependant on θ_2 while L_{PN} is solely dependant on θ_3. One now may rewrite Eq. 4.7 as:

$$L_{PN}(\theta_3) = C_2 - L_{KL}(\theta_2) \tag{4.8}$$

where C_2 is a constant. Using Eq. 4.8 one can rewrite Eq. 4.6 as:

$$\theta_3 = L_{PN}^{-1}(C_2 - L_{KL}(\theta_2)) \tag{4.9}$$

$L_{KL}(\theta_2)$ can be expressed as:

$$L_{KL}(\theta_2) = \beta_2 R_1, \quad \beta_2 = B_2 + \theta_2 \tag{4.10}$$

where R_1 and B_2 are design constants. $\beta_2 = B_2$ holds when $\theta_2 = 0$.

$L_{PN}(\theta_3)$ can be expressed as:

$$\begin{cases} X_3 = h'_3 cos(\varphi_3 + \theta_3) + D_2 & (4.11a) \\ Y_3 = h'_3 sin(\varphi_3 + \theta_3) - d_2 & (4.11b) \\ L_{PN}(\theta_3) = \sqrt{X_3^2 + Y_3^2} & (4.11c) \end{cases}$$

where h'_3, φ_3, D_2 and d_2 are design constants. One can now derive θ_3 by combining Eq. 4.9, Eq. 4.10 and Eq. 4.11.

By following the kinematics above, the relationship between θ_0, θ_1 and θ_2 as well as the relationship between θ_2 and θ_3 can be acquired, and the results are as shown in Fig. 4.17.

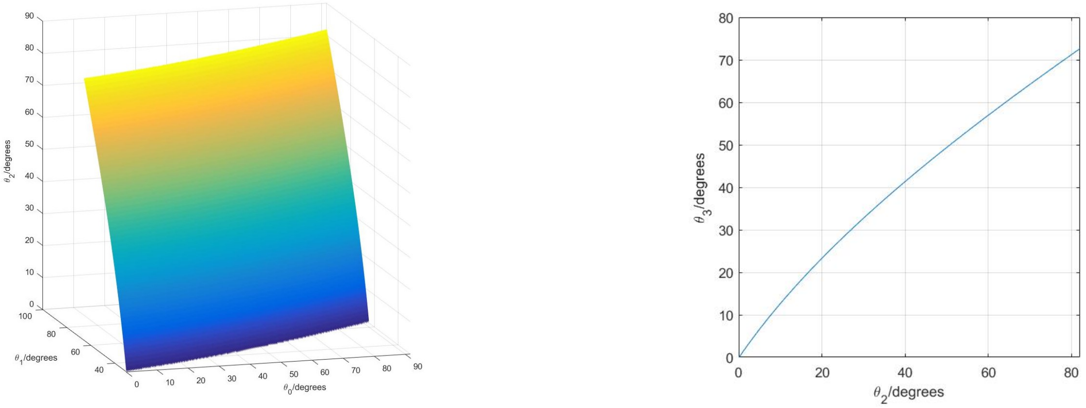

(a) The relationship between θ_0, θ_1 and θ_2.

(b) The relationship between θ_2 and θ_3.

Figure 4.17: The relationship between pulley position θ_0, MCP joint position θ_1, PIP joint position θ_2 and DIP joint position θ_3.

4.2.1.3 Applying Embedded Mechanical Intelligence with Underactuated Finger

The principle of Mechanical intelligence is adopted in this under actuated finger design for automatic object conforming and optimal trajectory following. We would like to illustrate the mechanical intelligence respectively in both the flexor and extensor aspect.

Even though the finger is under actuated, the two DoF on the finger are constrained and coupled with each other by the actuated flexor tendon. Fig. 4.18a shows a scenario in which the length of the tendon is fixed, and the finger's posture can only be along a certain trajectory depending on the loading condition on the finger. If the finger is mainly loaded on the tip, the finger will be straight, which is good for grasping with finger tips, while if the load is mainly on the middle of the finger, the finger will be bent, and it will automatically shape itself to the best fit on the surface of the objective.

The specific arrangement and design of the extensor tendons make the finger follow a desired trajectory under zero load condition. When grasping, it is preferred to keep the finger straight until the finger touches the objective or the proximal phalanx reaches its limit of rotation during a grasping motion, as shown in Fig. 4.18b, ensuring the largest workspace for each finger. Also, as discussed before, the finger shapes itself according to the loading condition, thus keeping the finger straight while approaching the objective helps the finger to shape itself to the best grasping shape upon contact when the grasper is going to grasp and hold the objective in hand, or reach its tip out for picking the objective with the fingertips when the objective is relatively small. This feature is achieved by implementing mechanical intelligence and will be explained in this section from the view of the flow of potential energy in and out the two extensor tendons. Note that other researchers have also managed to make an under actuated hand to follow a certain trajectory via mechanically realizable manifolds[11], but the trajectory is pre-determined and the workspace of the fingers are limited. By integrating mechanical intelligence into the design, the fingers on DAnTE can follow multiple trajectories according to the environment and the goal objects, resulting in a much bigger workspace.

The energy equality equation when flexing is as Eq. 4.12, where J is the kinematic energy

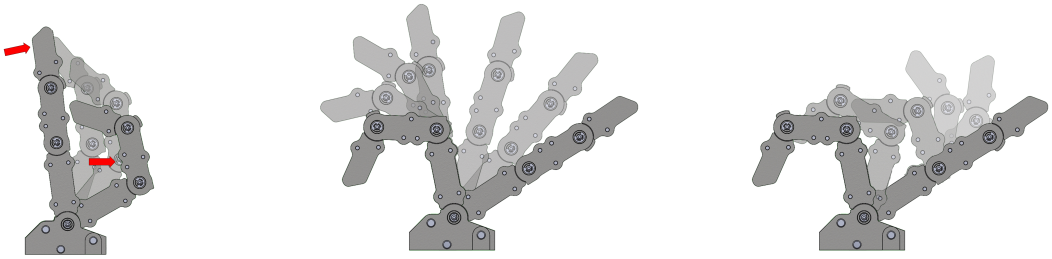

(a) Finger trajectory under different loading conditions. (b) Finger flexion trajectory under free loading conditions. (c) Finger extension trajectory under free loading conditions.

Figure 4.18: The specific arrangement and design of the extensor tendons make the finger follow a desired trajectory under zero load condition for gesture dexterity, while automatically change the gesture to adapt to loading.

in the system, E_p is the elastic potential energy, E_μ is the friction energy lost, W is the energy output to the environment, and M on the right side is the total energy from the actuator. E_g is the potential energy from gravity. E_μ is introduced by the tendon contacting and sliding against the finger inner structure.

$$J + E_p + E_g + W = M - E_\mu \tag{4.12}$$

E_p can be split into the potential energy stored in the springs, E_s and the potential energy stored in the elastic member between the distal and middle phalanx, E_k. E_s is associated with MCP joint and E_k is associated with PIP & DIP joints. Without loss of generality, we assume the finger moves quasi-statically under freeload condition, and now there is no kinematic energy in the system nor output to the environment, the fingers are relatively light so E_g is very small and it can be ignored. E_μ is compensated by the motor actuation input so it can be combined into W. Eq. 4.12 then can be rewrite as Eq. 4.13.

$$E_k + E_s = M \tag{4.13}$$

The distal phalanx extensor tendon elastic member and the tensile spring for the main extensor tendon are designed such that, without external forces and only by pulling the flexor tendon, it is significantly easier for the energy to flow into the tensile spring than the distal phalanx extensor tendon elastic member. This results in the proximal phalanx always bending prior to the middle and distal phalanxes, and only when the proximal phalanx is stopped by external force or the MCP joint reaches its limit will the middle and distal phalanxes then begin to bend.

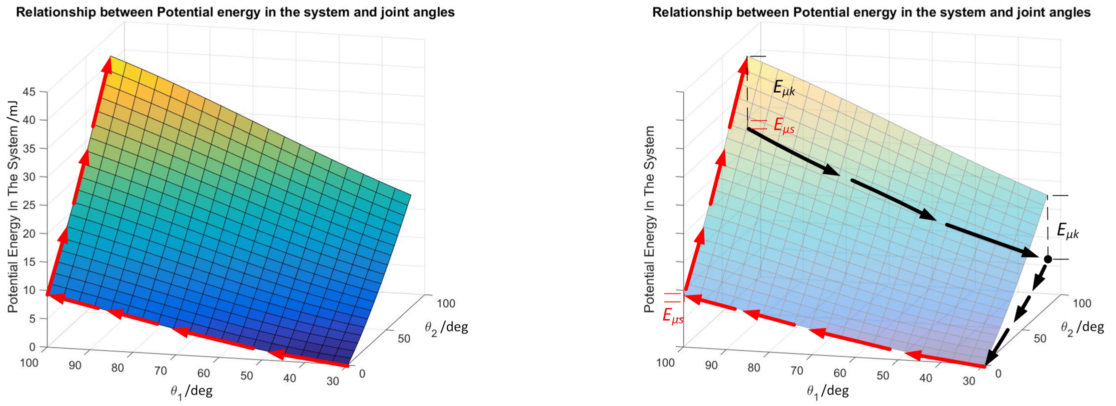

(a) Potential energy in the finger system regarding to the finger joint positions and system potential energy flow.

(b) Qualitative potential energy flow in the system when releasing the finger.

Figure 4.19: The system always looks for potential energy local minima and therefor accumulate potential energy via the slowest trajectory while release the potential energy via the fastest trajectory.

Shown in Fig. 4.19a is a plot of total potential energy in a finger as a function of θ_1 and

θ_2, which are the MCP joint angle and the PIP joint angle. This finger is a typical spring-mass-damping system, and for this kind of a mechanical system, the stable equilibrium in most cases are coincident with local minimum potential energy points. In our finger system, as the flexor tendon is being pulled, energy is pumped into the system and distributed among the values on the left side of Eq. 4.12.

Besides external influences from the environment, the trajectory of the finger is determined by its potential energy status, since the finger will always try to follow the trajectory that locally minimizes its energy state. In other words, when the flexor tendon is being pulled, the finger retracts along the trajectory in which the potential energy in the finger increases the slowest. Note that when the finger moves with a very high speed, the inertia of the finger itself then can't be ignored, and the inertial force from the finger acts like a external force. When the finger is moving with a relatively low speed and there is no external force from the environment on the finger, the retraction trajectory of the finger is exactly the trajectory marked with red arrows as shown in Fig. 4.19a, which is the slowest trajectory for the potential energy in the system to increase.

When the finger releases, it should also try to follow the trajectory that minimizes its energy state. Thus, ideally, with friction in the system ignored, the finger should follow the reversed trajectory of the red-arrow marked retraction trajectory. However, in reality, instead of releasing the finger in the reversed sequence of retracting, the finger is released with MCP joint first, and then PIP and DIP joints. Due to the complex nonlinear damping that is involved in the releasing process, it is very difficult to come up with an accurate theoretical model for this, but the phenomenon will be analyzed comprehensively with the support of experiment results.

As mentioned in the mechanical design section, DAnTE is designed for grasping tasks, thus the fingers are only actuated in flexing direction, and the recovery process is done by the elastic components in the system. The elastic components store potential energy for recovery process and consume the force provided by the actuator during flexion. For better gripping performance and power efficiency, the elastic components in our finger system are designed with relatively low spring constants. When the fingers are driven by the actuators for flexion, the friction forces are compensated by the actuation force. However, when the finger is recovering, the friction forces are no longer compensated and they are of the same order of magnitude as the recovery forces from the elastic components. In this case, the friction in the system increases the difficulty for the potential energy to release. The friction is mostly from the slipping contact between the tendons and the finger along the tendon routes. E_μ can be split into $E_{\mu s}$ which is associated with MCP joint movements and $E_{\mu k}$ which is associated with PIP&DIP joints movements, and the energy equality becomes:

$$E_k + E_s + M' = E_{\mu k} + E_{\mu s} \tag{4.14}$$

where M' is the energy input from the actuator and it is a negative term since the actuation tendon is being released.

From Fig. 4.12 we can tell that when only the MCP joint associated with θ_1 is rotating, there is almost no part of the tendons sliding against the finger inner structure, while releasing PIP and DIP joints associated with θ_2 and θ_3 will cause all the tendons to slide against the finger, generating significant friction forces. Thus, it turns out to be much easier and faster for the finger system to go to a lower potential energy state by releasing MCP joint prior to the coupled PIP and DIP joints. Again, since it is extremely difficult to model friction in the system, we will for now only look at this phenomenon qualitatively.

Fig. 4.19b is modified from Fig. 4.19a and since we are looking at this problem from a qualitative aspect, the unit and values for Z axis have been erased. $E_{\mu s}$ and $E_{\mu k}$ are qualitatively marked at the points associated with maximum finger joint angles, and the finger releasing routine has been marked with black arrows. As discussed previously, it would consume significantly more energy for the PIP joint to release than the MCP joint, which causes that the total energy in the system drops faster if it releases the PIP joint first.

Experiments were conducted to support the theoretical analysis on mechanical intelligent in the finger system, and the details and results of the experiments will be shown and discussed in later sections.

4.2.1.4 Control Methods

Two different controllers have been developed for DAnTE for different objectives. Velocity control is adopted for grasping tasks that requires high robustness and good tracking accuracy, while a compliance controller is developed for grasping tasks that require dedicated control of grasping force applied to the object. System controllers running at about 100Hz are developed in LabVIEW environment, as well as for serial communication to microcontrollers running FOC control on brushless motors, at a rate of 4kHz.

Velocity Control We are currently only tracking the angular position of the tendon pulley, while the position and speed information from the encoder on the MCP joint has not been implemented into our controllers. The error of the pulley position is fed into a PD controller which generates a motor speed command input for the motor controller. The motor speed is then fed through a PID controller for the BLDC motor, and current control commends are then sent to the FOC controller for the BLDC motor. The control block diagram is as shown in Fig.4.20.

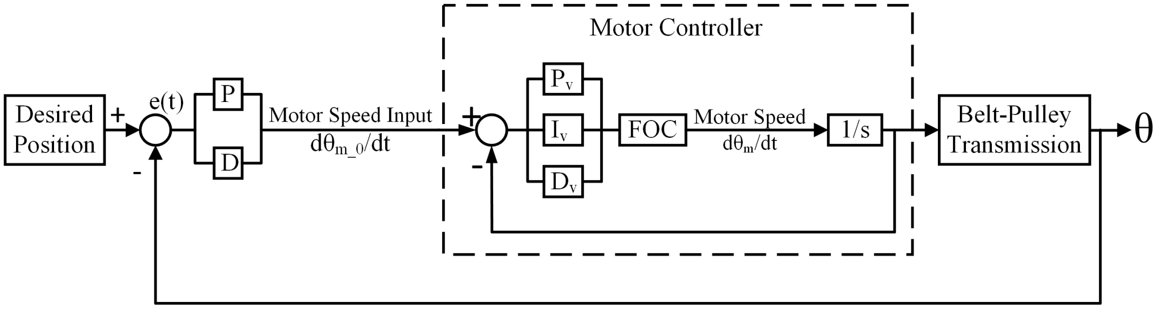

Figure 4.20: Velocity control block diagram.

The finger controlled in this method appears to be very robust and precise in position tracking.

Compliance Control In most of the grasping tasks that DAnTE is designed for, controlling the pulley position and the MCP joint position is not necessary, since the mechanical intelligence in the finger system will automatically shape the finger into the best posture for holding the goal objects. Even though the pulley position is the same, the positions of all the three joints on the finger can be different for different objects. However, the MCP joint position and velocity is still being tracked, meaning the position and velocity of the PIP and the DIP joints can be calculated through kinematics. Forces applied through the finger were not quantified, but determined empirically, and since we rely on the torque current in the motor winding to reflect the force applied, it is very important for us to know the velocity and position of all the three joints in our compliance control, such that the back driving force from the springs and the elastic components and forces generated from the moment of inertia of the three phalanges can be known and compensated for. The following equation of motion[60] applies to the finger system:

$$B(q)\ddot{q} + C(q,\dot{q})\dot{q} + F\dot{q} + g(q) = u - J^T(q)h_e \tag{4.15}$$

Where q is the column vector of joint angular positions.

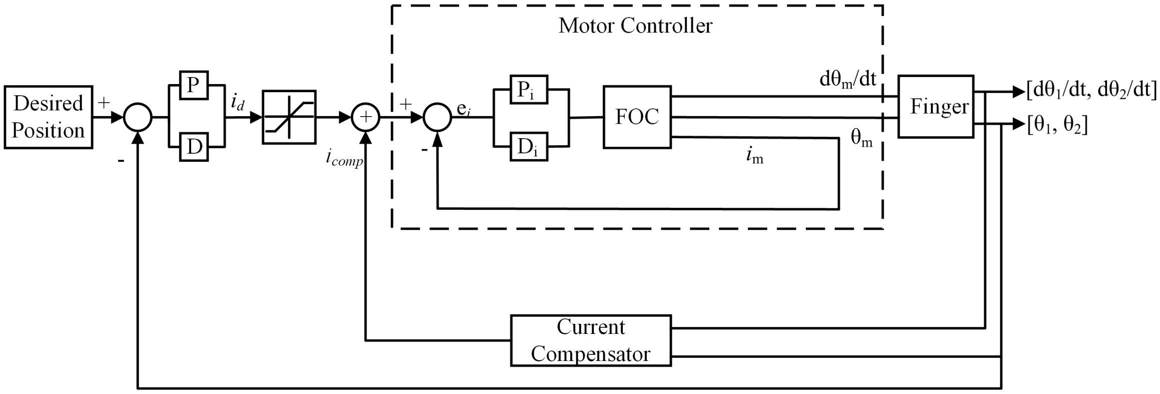

Figure 4.21: Compliance control block diagram.

The mechanical intelligence property within the fingers made it possible to perform grasping tasks where the object location is not necessarily known in the grasper workspace.

The compliance control block diagram is as shown in Fig.4.21. The error on the tendon pulley position between the reference and current position is fed into a PD controller to generate a current control reference i_d. This current control reference i_d is then fed into a saturation filter to get the actual current control signal $\hat{i_d}$. The saturation filter is set to limit the torque current in the motor according to required force output.

The speed and position information of the MCP joint and the pulley is used to calculate the forward kinematics of the finger system, and the position and speed of the joints are fed into a current compensator to calculate compensation for phalanges moment of inertia and elastic back driving force from the elastic member and the springs. Compensated current control signal is finally fed into the motor controller.

4.2.1.5 Experiments, Results and Discussion

Free Load Finger Retraction & Extension The free load finger retraction and extension experiments are done to collect experimental data to support the previous analysis on the mechanical intelligence property on the finger system. Both of finger retraction and extension experiments are done with a very low speed such that the moment of inertia can be ignored, and the torque current in the motor is recorded during the experiments. Since the motor torque is linear to the current in the winding, and the torque is linear to the tension in the actuation tendon, thus the motor torque is used in the experiments to represent the tension in the actuation tendon. The BLDC motor has a motor torque constant $K_T = 0.032$ Nm/A, and the speed reduction ratio of the transmission is 8.6:1 and the tendon pulley diameter is 20mm, thus the tension in the actuation tendon is 13.76 N/Amps.

Fig. 4.22a shows the experiment results for flexing and extending. The torque current in the motor refers to the Y-axis on the right while all the angular position displacement of the joints and pulley refer to the Y-axis on the left. The pulley position and MCP joint position displacements are as read from the encoder on the joint while the PIP joint position is calculated from forward kinematics. There is no need to show the DIP join position since

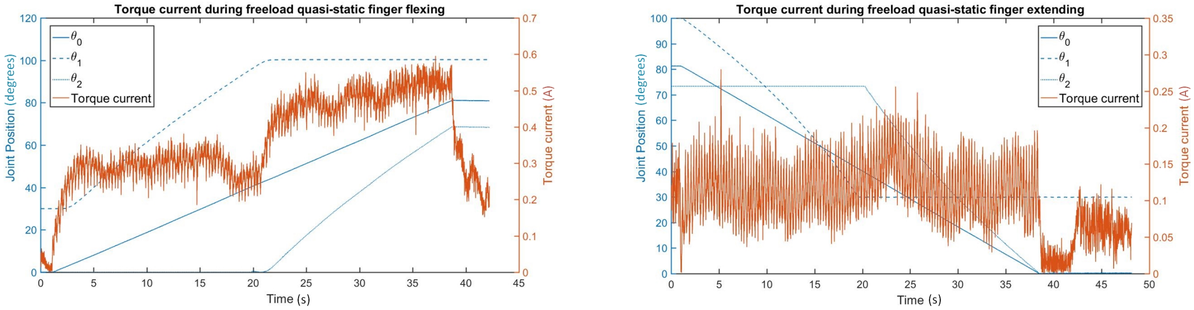
Torque current during freeload quasi-static finger flexing

Torque current during freeload quasi-static finger extending

(a) Flexing

(b) Extending

Figure 4.22: Torque reading from the actuator in amps during freeload quasi-static finger retraction and extension. The tension in the actuation tendon is 13.76 N/A.

it is coupled with PIP joint and those two joints always move together. By looking at the figure from finger flexing test, we can easily tell that during the whole flexing process, the MCP joint moved prior to the PIP & DIP joints, as the MCP joint started bending as soon as the pulley started pulling the tendon, while the PIP joint remained still until the MCP joint has reached its mechanical limit and stopped bending. The data also show that less current is required to drive the MCP joint than the PIP & DIP joints.

Experiment data of motor torque current during quasi-static releasing is as shown in Fig. 4.22b. The current varies very little regardless of where the joints are during the whole process. The magnitude of the motor torque is significantly smaller than that of when the finger is retracting, and it is doing constant minimal negative work while the finger is releasing. The rest of the potential energy in the springs and elastic member is consumed by the friction in the system. The PIP & DIP joint couple did not start extending until MCP joint was fully extended. This support and confirm our previous analysis on the energy flow theory behind the mechanical intelligence that the finger system presents.

Grasping Test The mechanical intelligence that is designed and embedded in the finger systems on DAnTE enables the finger to follow a desired trajectory under free-load condition while automatically configuring into the best posture for the goal object when preforming grabbing task.As the trajectory control function of the mechanical intelligence was discussed in the previous sections, the automatic object fitting ability and the general grasping ability of the system is tested and evaluated below.

As introduced in the design section earlier in this paper, DAnTE has two fingers that can rotate mirrored. This function provides DAnTE with three general finger postures: parallel posture with all fingers parallel with each other, mirrored posture with the two movable fingers mirrored with each other and perpendicular with the stationary finger, and axisymmetric posture with all the three fingers axisymmetric with each other. These three modes can cover almost all grasping cases, and though the movable fingers can move to any arbitrary position between the parallel posture and the mirrored posture, configurations other than the mentioned three are very rarely used.

Numerous grabbing tests are done, and several representative scientific grasping scenarios[13] used to fully evaluate the grasping capability of DAnTE are shown in Fig. 4.23. The fingers can automatically fit to the outline of the goal object very well, and for the same object, unique and optimized grasping configurations of the finger joints are applied automatically for different grasping methods. For instance, very different finger joints configurations are applied when grabbing a red ball firmly in hand or holding the same ball with finger tips. The configuration is also different when it comes to holding a smaller ball with a precision grasp or a screw driver with finger tips or heavy wrap. For these tasks, the axisymmetric posture is applied. When grabbing objects with a long profile, such as a screwdriver, a bottle or the handle of a power tool, the parallel posture comes handy. When it comes to objects with a flat and thin profile, such as a card, or small objects that is hard to be picked up with three fingers, two finger pinch will be applies. Note that Fig. 4.23 has been modified from the original figure in [13], since three-finger hand can act very differently to a human-like five-finger hand for some specific tasks. For instance, while there are not as many different ways of handling prismatic objects, there are also some configurations unique to the three-finger hand, such as using the thumb finger as axial support when holding a mug full of water or using the palm to provide axial support to firmly hold a small screwdriver. These two ways of handling prismatic objects precisely can also provide some in-hand manipulation that may be needed when using the object tool.

Dexterous Grasping The goal of this experiment is to test DAnTE's ability of dexterous force controlled grasping and evaluate the effectiveness of the inherent compliance on the fingers introduced by using quasi direct-drive actuators. Dexterous force controlled grasping over delicate objects is very challenging for all robotic hands. The compliance controller we have developed is used in this experiment and the challenging task we have chosen for DAnTE is to approach and grasp a fresh potato chip as shown in Fig. 4.24a with a high speed, while not breaking the potato chip.

Modify this following par so that it connects the next section natrually

In this experiment, the three fingers are asymmetric and play very similar roles, thus we only need to look at the experiment data from one finger to sufficiently know about the other

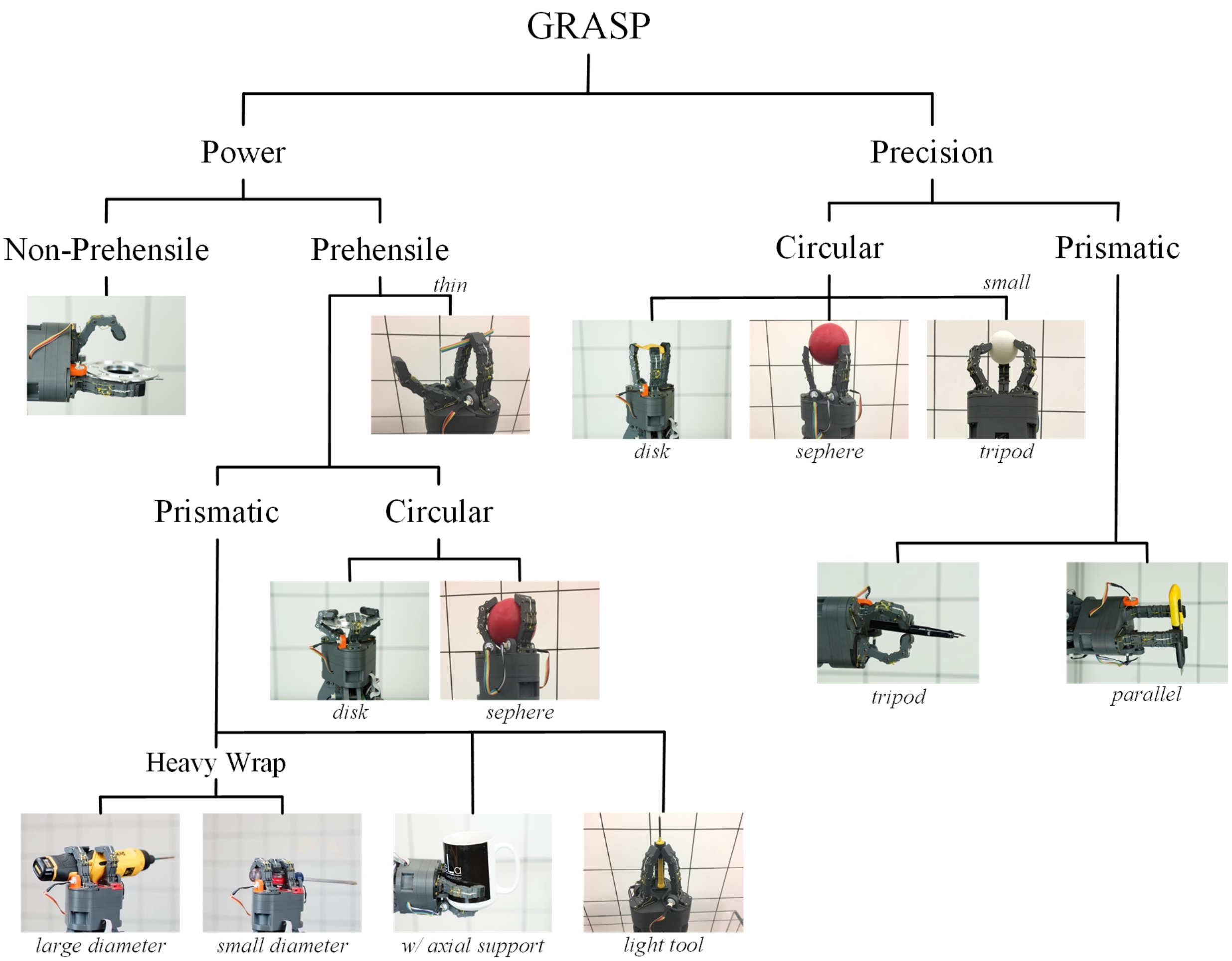

Figure 4.23: Evaluation of the grasping capability of DAnTE. The fingers can automatically fit to the outline of the goal object very well, and for the same object, unique and optimized grasping configurations of the finger joints are applied automatically for different grasping methods.

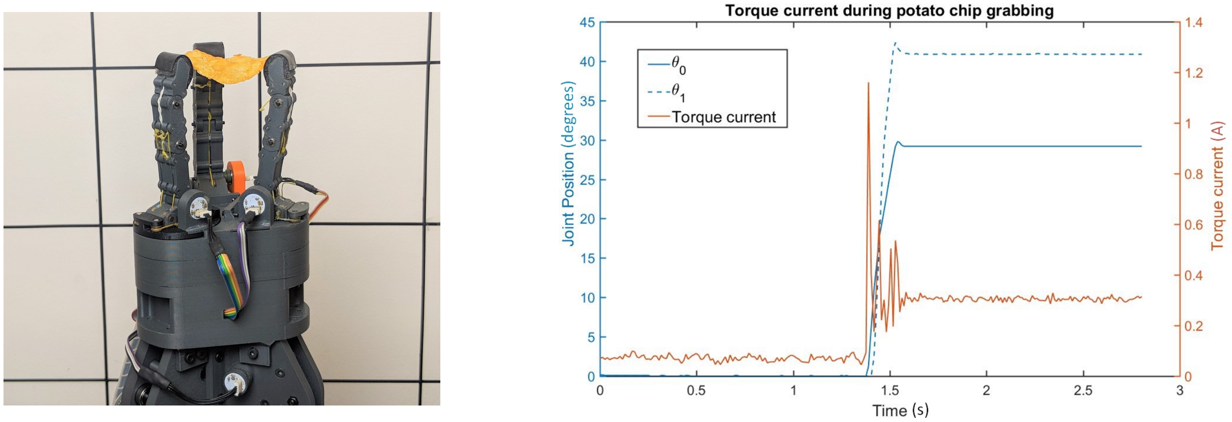

(a)

(b)

Figure 4.24: (a)DAnTE grasping a potato chip and (b)the corresponding torque current in one of the actuators during the potato chip grabbing manipulation. The tension in the actuation tendon is 13.76 N/A.

two fingers and the whole robotic hand. Shown in Fig. 4.24b is the recorded experiment data of one finger. The grasping task was finished within a quarter of a second. The peak of the torque current at the beginning is the sudden acceleration of the finger to a desired high speed, and the finger stopped moving once it made contact with the potato chip and kept a preset light grasping force. However, there is still a little overshoot in the system. It might be cause by that even though the motor controller runs at 4kHz, the system control loop can only run at about 100Hz thus there is a little latency for the control loop to detect and react to the signal generated upon contact. We hope to eliminate the overshoot by increasing the frequency of the system control loop in the future.

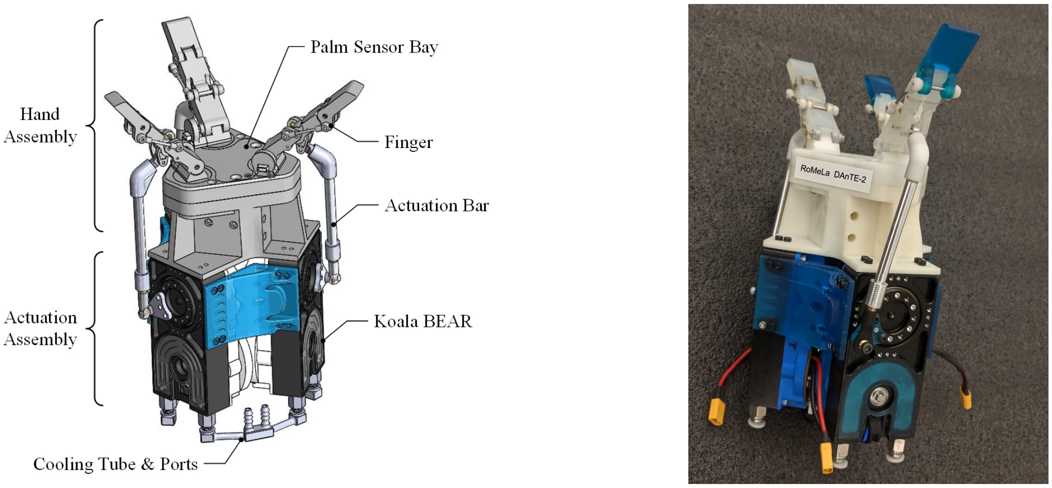

(a) The DAnTE-2 System CAD

(b) DAnTE-2 Physical System

Figure 4.25: The CAD model and actual physical system build of DAnTE-2

4.2.2 DAnTE-2

With the success and inadequacy of DAnTE 1 learned from experience, a series of optimization and updates have been carried out base on the design of the system, and the latest version DAnTE 2 is presented as follow.

4.2.2.1 System Overview of DAnTE 2

The mechanical architecture of DAnTE 2, as presented in Figure.4.25 is very similar with that of DAnTE 1. DAnTE 2 is composed by a three finger Hand Assembly and an Actuation Assembly that contains three Koala BEAR module, with each Koala BEAR driving a finger through an Actuation Bar. The Actuation assembly features liquid cooling connection and ports to keep Koala BEAR modules run at the maximum performance.

4.2.2.2 Upgrades From DAnTE 1

The purpose of developing DAnTE 2 is to turn DAnTE 1, which is a experimental prototype, into a much more reliable research platform. To accomplish this goal, the following updates have been integrated.

Finger The focus of finger update is the under actuated mechanism.With the help of mechanical intelligence in the under actuated mechanism of the fingers on DAnTE 1, the fingers can traverse almost the whole possible workspace without the influence of external loading or forces. This means that even though the fingers of DAnTE 1 are under actuated, they can controllably reach a equivalent workspace to that of a fully actuated finger with same DoF. This is very remarkable as it almost eliminated the uncertainty in the trajectory of such an under actuated mechanism and makes it fully controllable under load-free condition, as shown in Figure.4.18. It is of great value when DAnTE 1 is used for agile finger motions and gesture presentation. However, when using DAnTE 1 for grabbing tasks, this feature is of very little value, except for several very special cases where the fingers need to be pre-adjusted into certain gestures to approach the object. Thus, the mechanical intelligence of the finger is modified such that the finger's retraction starts with the MCP joint, then the coupled PIP & DIP joint, which is the same as before, covering the biggest grabbing area; but different from DAnTE 1, the fingers on DAnTE 2 simply extend in the totally opposite joint sequence to that of retraction. The designed free-load trajectory of the finger is as shown in Figure.4.26a. Not only does the design and realization of the desired mechanical intelligence become easier, it is also more practical as the major tasks of DAnTE 2 is to grab, secure and sense the goal objects.

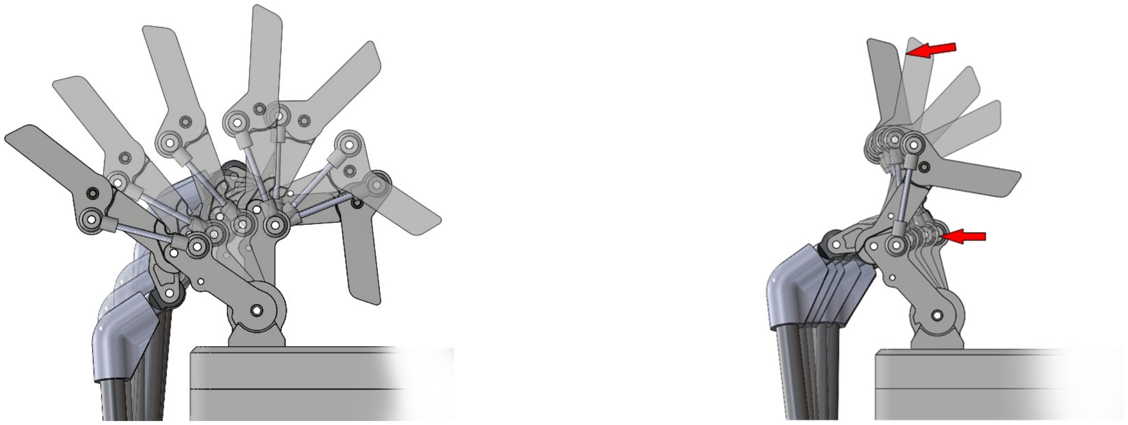

(a) DAnTE-2 finger trajectory under free different loading conditions.

(b) DAnTE-2 finger trajectory under different loading conditions.

Figure 4.26: Fingers on DAnTE-2 have slightly different trajectory from that of DAnTE-1 under free loading condition, but present same behavior under the same loading.

Other than the change in the free-load extension trajectory, the functionality of the finger remains the same as before. The architecture of the underactuated mechanism and its embedded mechanical intelligence in terms of automatic reshaping to bast fit the outline of the target object remains the same. (Fig.4.26b). Same as the previous version, the fingers are fully covered with high resolution encoder for each DoF, so that the gesture of each finger is fully known at all time.

Transmission & Actuation The change of finger transmission is one of the major update to DAnTE for better reliability. The fingers on DAnTE 1 are driven by a simplified anthropomorphic tendon system. The advantages of the design is the compactness and

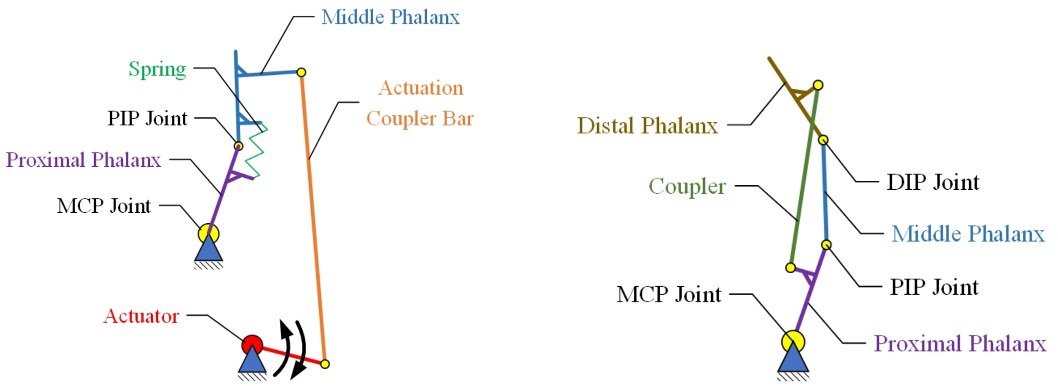

(a) Five-bar linkage for finger actuation. (b) Inverted 4-bar linkage for DIP&PIP coupling

Figure 4.28: Schematic drawings of the mechanisms in DAnTE-2 fingers.

low-weight of the system, and it is also easier to play around with the potential energy flow in the finger to realized interesting trajectories and mechanical intelligence profiles. The disadvantage is that the transmission efficiency is relatively low due to internal friction, and the finger is only actuated one way, with the extension of the finger realized with springs. Even though it is possible to have the finger actuated in both retraction and extension, the system complicity will likely be much higher. The tendon driven fingers are not reliable enough either, as the tendon lines and the channel structure on the finger phalanxes wear out rapidly under high load working conditions, resulting in a high maintenance demand.

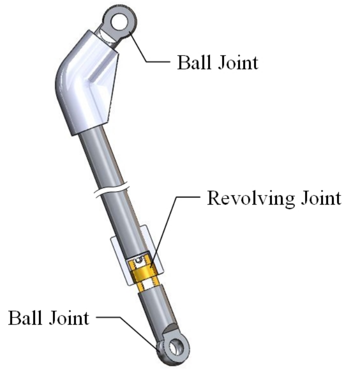

Figure 4.27: Actuation Bar

The fingers on DAnTE 2 are actuated via an actuation bar, and a 5-bar under actuated system is formed on each finger. The schematic drawing of the mechanism is as s4.28a. The fingers still have three joints among which the DIP&PIP joints are coupled, resulting in a finger with 2DoF. Instead of tendon, the DIP&PIP joints are coupled by a linkage, forming an inverted 4-bar linkage mechanism, schematic drawing as shown in Figure.4.28b.

To allow the axial rotation on two of the fingers, the Actuation Bar needs to cover an extremely wide swivel range (about 90°). The swivel range of each ball joint at the end of the actuation bar is 20°, thus to cover the extra 50°, another DoF has been added on to the Actuation Bar, which allows the Actuation Bar to rotate freely about the cylindrical axis on the bar, realized by three copper sliding bearings as shown in Figure.4.27.

The last major change update on DAnTE is the actuation assembly. The Koala BEAR modules are used in replace of the 3D printed actuator prototype. All three actuators are connected with customized tubing, making DAnTE 2 ready to be connected to any liquid cooling pump.

4.2.2.3 Current Status of DAnTE 2

The updates applied to DAnTE makes DAnTE 2 a much more completed version. It has inherited the motion and force control dexterity from DAnTE 1, and the improvement in integrity, modularity and robustness qualifies it to serve as a reliable research and education platform at RoMeLa. It is a capable robotic end-effector that is almost maintenance free. DAnTE 2 also features a Palm Sensor Bay, which is a structure that is reserved for the purpose of integrating various sensors onto the system, such as cameras and proximity sensors.

DAnTE 2 enables the researchers at RoMeLa to further explore grasping tasks with both motion and force control dexterity. Related topics includes handling of objects with wide range of materials, object shape and material sensing and estimation and tactile teleoperation, and its potential is beyond imagination.

4.3 Experiments with Legged Robots

4.3.1 NABi-2

4.3.1.1 Introduction to NABi-2

Humanoid robots that emulate the form and function of human beings have been a prevalent area of robotics research for several decades. Traditional humanoid robots are realized with fully actuated limbs, actuated by low speed, high torque and stiff actuators, amenable to classical position-based control approaches [26]. These systems see the most success in fairly structured environments, where the robot's movements and interactions are either dynamically conservative or determined in advance. However, the environment these robots are expected to function within are often quite unstructured and would necessitate the use of more active behaviors, meaning this type of approach may not be the most effective.

Recently, more capable legged systems have been developed that can operate over unregulated terrain through the use of dynamic running, hopping, trotting, and bounding behaviors enabled by hydraulics ([33], [52], [57]) or series elastic actuation ([54], [29]). These methods of actuation are customarily used for such gaits due to the fact that dynamic locomotion such as running and jumping requires high torques, and electric motor actuators typically achieve this through severe gearing that is easily damaged when confronted by the large impulses experienced during the ground impact following an aerial phase. These robotic systems with such added mechanical compliance usually have complex dynamics, making them difficult to control at best while restricted in their workspace and capabilities at worse.

The recent development of Proprioceptive Actuators provides a new solution. Compliance is inherent to these actuators and mechanical compliant elements are not longer needed, achieving high fidelity force control with sufficient power and torque for dynamic locomotion.

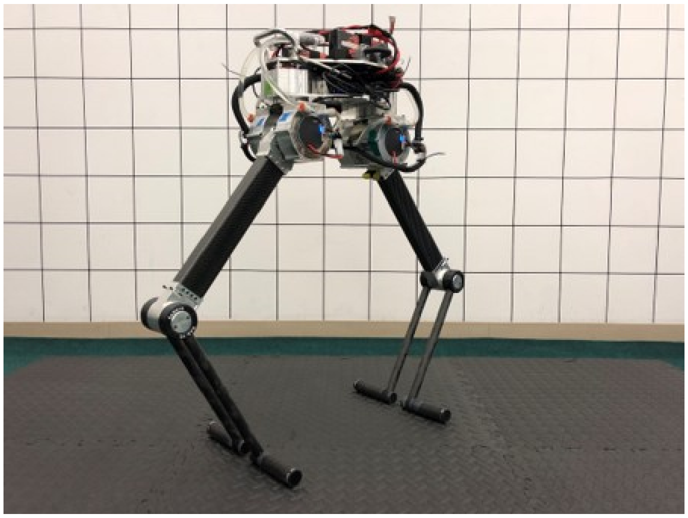

Figure 4.29: The Non-Anthropomorphic Biped Version 2 (NABi-V2) lower body utilizes high torque, back-drivable actuators that provide high fidelity force control capabilities.

This back-drivable, high-torque actuator technology is predominantly applied to legged robotics in the form of dynamic quadrupeds like [48] on a large scale and quadrupeds and bipeds like [31] and [55] on a smaller scale, but is not often used on a large scale to power humanoids or bipeds in general. To this end, we aimed to incorporate the potential of this actuation method into the Non-Anthropomorphic Bipedal Robotic System (NABiRoS), a bipedal robot that attempts to tackle some of the difficulties of biped locomotion and control by rethinking the fundamental design of a bipedal robot. The result of this development is the Non-Anthropomorphic Biped: Version 2 (NABi-V2) shown in Fig. 4.29, a biped with a unique leg morphology that can perform dynamic behaviors such

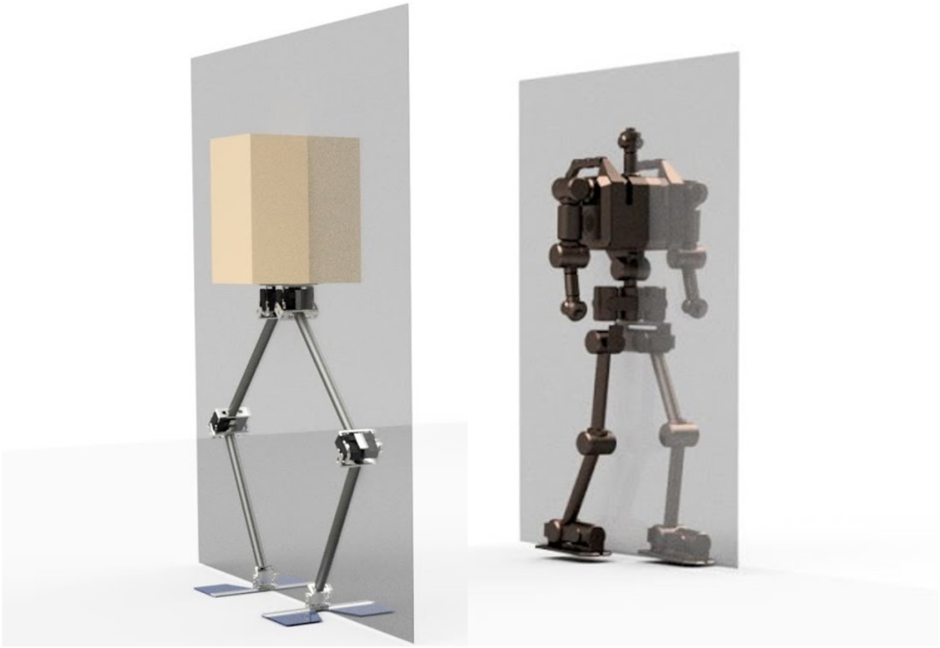

Figure 4.30: Comparison of the original NABiRoS (left) and a more traditional humanoid (right) that shows the sagittal plane of each, as seen in [71].

as two-legged pronking thanks to the use of proprioception and force control. The main contribution of this work is to present the new NABi-V2 platform and show how dynamic, event-based controllers can be implemented relatively simply on a biped with back-drivable electric actuation.

Conventional humanoid systems are designed to be highly versatile in function, but in implementation are often prohibitively slow, unsafe, or expensive due to the approach taken to perform bipedal locomotion. Traditional 'forward-walking' bipedal locomotion on a typical humanoid with 6DoF legs is a heavily underactuated problem that typically leverages some form of dynamics compensation algorithm with inertial and force feedback. This form of walking is inherently difficult due to the fact that there is an offset in the hip joints that is perpendicular to the walking direction, creating undesirable oscillatory moments that can only be accounted for through accurate system modeling combined with sophisticated closed-loop feedback algorithms and high fidelity sensors, or by taking smaller steps. However, these moments do not appear when taking steps side to side, because the hip offset is in the same plane as the direction of travel. If the main mode of locomotion is sideways walking, the forward-facing knees are not being used, and can be rotated by ninety degrees so that the legs are aligned in a plane. By aligning the legs in the sagittal plane, forward walking can be achieved using the sideways walking motion. With the legs aligned in a plane, the ankle can be removed and replaced with a much simpler foot element.

This simple, 2DoF leg configuration was first featured on NABiRoS, a prototype biped with high-gear ratio servo actuators at the joints and a mechanical spring foot element that can walk by mimicking a linearized inverted pendulum, and perform two-legged pronking thanks to its series-compliant leg and foot [71]. NABiRoS, illustrated in Fig. 4.30, demonstrated that bipedal robots do not need to share the morphology of a humanoid to be able perform simple locomotion, but the original platform was limited to locomotion in a plane. Further investigation into how the NABiRoS platform could be adapted to achieve turning was done in [70], with the results showing that adding a third, yaw DoF at the hip allow for the simplest and most effective turning strategy.

While NABi-V2 shares the morphology of the original NABiRoS with the additional hip DoF, it differs in how it is actuated. NABi-V2 uses Panda BEAR modules at each of its leg joints, while NABiRoS uses position controlled servos. Furthermore, NABi-V2 no longer needs a compliant foot element in series with the rest of the leg to perform more dynamic motions because compliance can be achieved through software in the BEAR modules.

4.3.1.2 NABi-2 System Presentation

Design NABi-V2 shares the same morphological characteristics as the original NABiRoS to continue to take advantage of the benefits that are inherent in the non-anthropomorphic design. However, it has a third yaw DoF at the hip, and its leg joints are all driven by the Panda BEAR back-drivable actuation modules that can provide significantly improved dynamic performance over most traditional position controlled servos. All actuation modules feature optional liquid cooling for actuator heat dissipation to maintain a high torque output. Additionally, NABi-V2 is planned to have a pair of 3-DoF arms with modular end-effectors that can mount assorted tools to enable NABi-V2 to perform various inspection and manipulation tasks. The arms can also be potentially used for locomotion and fall recovery, as was explored in [70]. The design and structure of NABi-V2 is shown in Fig. 4.31.

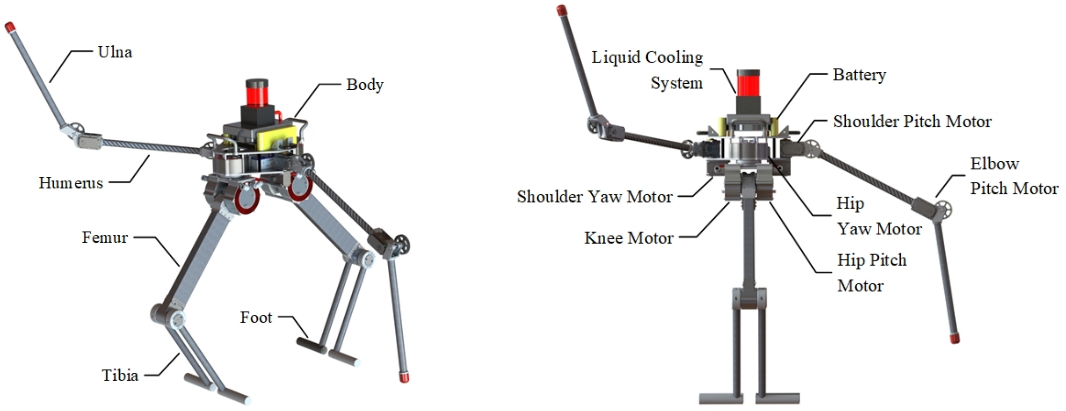

(a) (b)

Figure 4.31: NABi-V2 isometric view (a) showing key aspects of the non-anthropomorphic design, and a front view (b) detailing the layout of the actuation modules and associated subsystems.

To maximize dynamic performance of NABi-V2, its legs are designed with minimal mass and inertia. The femur and tibia links are composed by epoxying lightweight carbon fiber tubes to aluminum joints and comprise around 20% of the total robot mass. All leg actuators are located at the hip to minimize the inertia of the leg, with the help of a pair of 1:1 ratio pulleys with a timing belt as the transmission of the knee joint, as show in Fig. 4.32.

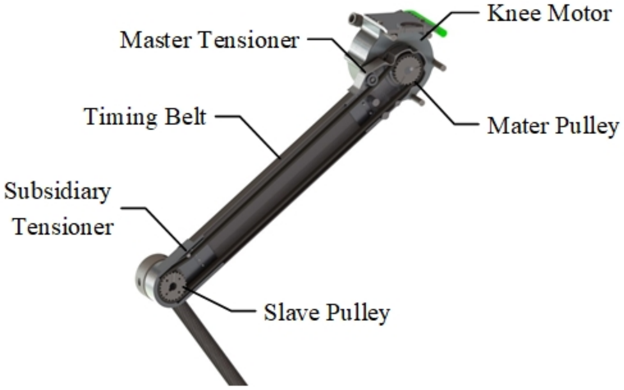

Figure 4.32: Section view of femur link with the pulley transmission mechanism inside enabling continuous knee rotation.

The carbon fiber tube on the femur links has a rectangular profile that covers the timing belt and shields the transmission from external contaminants and other external forces. A pair of tensioners located at each end of the femur link keep the belt under tension and prevent backlash. NABi-V2 also takes advantage of the belt-pulley transmission by adopting a double-shin design that allows the knee joint to rotate continuously, enabling some creative methods for locomotion across certain obstacles as investigated in [17]. The lightweight carbon fiber and aluminum structure of the legs are also applied to the arms, but the arm actuators are standard geared servos located directly at the joints for simplicity. Currently, the arms are not attached to the NABi-V2 to simplify and expedite the development of locomotion control.

NABi-V2 carries two 3250mah 4S LiPo batteries that power all of its subsystems: an Intel NUC computer, a liquid cooling system comprised of a reservoir-pump assembly and radiator-fan assembly (typically used in PC liquid cooling), a LORD MicroStrain 3DM-GX4-25 IMU, and its actuators. Nominal specifications of NABi-V2 are listed in table 4.3.

Table 4.3: Specifications of NABi-V2 platform.

Parameters	Value
Weight	11 kg
Height	85 cm
Max. Payload	1 kg
Max. Runtime	30 min

Software Architecture The original NABiRoS software architecture is structured with simplicity and modularity as its focus to promote rapid development. However, to achieve stable proprioceptive force control while retaining the aforementioned characteristics, the architecture is modified to maximize speed by restructuring the architecture layout such that it supports concurrency. The different modules are shown in Fig. 4.33, with concurrently run processes highlighted.

The computer used to run NABi-V2 is equipped with an Intel Core i5-7260U @ 2.2 GHz with 8 GB of RAM. NABi-V2's software is written in Python 2.7 under Ubuntu 16.04, utilizing open-source libraries and optimized in-house built modules. Unlike other setups that may require a significant time from the user to prepare the machine, NABi-V2 can be readily set up under a Python virtual environment. This allows the code base to remain simple for many people to quickly get involved with the development.

Modularity of the architecture also invites multiple people to work on the development with minimal merge conflicts. By abstracting the details of each controller in one or more states in a trampoline based finite state machine (FSM), multiple people can simultaneously work on multiple controllers. Operations in each state is standardized by passing between states a ‘virtual robot’ object that resides on the stack. Then, different controllers can independently calculate their respective inputs and command the virtual robot using standardized method calls. The robot object then spins once to update its attributes and execute necessary methods, which includes updating the shared memory segment which is imperative for a fast control loop.

Concurrently, a hardware manager that is a dedicated process for each chain of limbs is run. The manager indefinitely runs a while loop sequence of communication with the POSIX shared memory segments that: 1. Read the state of the hardware and, with the semaphore, update the shared memory block that the hardware manager is writing to, 2. If necessary, with the semaphore, read from the shared memory block that the virtual robot writes to and write to the hardware. POSIX shared memory and semaphores were chosen to stay safe for potential multithreading and to keep semaphore overhead low. The hardware manager communicates with the hardware at maximum speed, and processes can be assigned to dedicated cores to further increase the communication frequency as seen in Table 4.4, which shows an average frequency over 10,000 communications between the hardware manager and the two chains of limbs. Through this approach, we are able to achieve stable proprioceptive force control despite using a dynamically typed language with unpredictable delays.

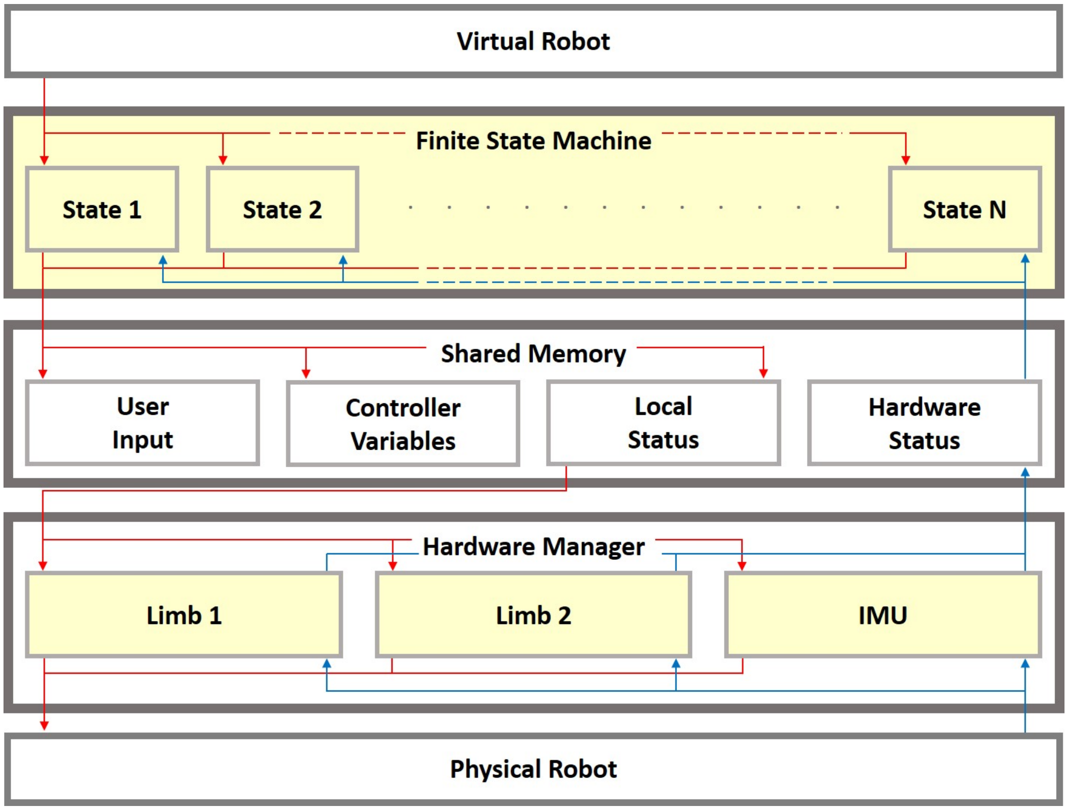

Figure 4.33: NABi-V2 software architecture layout, with concurrently running processes highlighted in yellow.

Table 4.4: Communication Frequency Comparison

Shared Core [Hz]		Dedicated Core [Hz]	
2026.99	2169.82	2289.47	2348.09

4.3.1.3 Control Implementation & Performance Presentation

Control Implementation The overall design of NABi-V2 makes it an ideal platform for pursuing force/torque based control approaches, though position control can be used if desired. For NABi-V2, force control simply involves defining some desired force to be exerted by the end effector, then converting these forces to joint torques by first rotating the forces into the robot frame and then multiplying by a Jacobian as shown in equation (4.16).

$$\boldsymbol{\tau} = J_c^T R_{BN} \boldsymbol{F} \tag{4.16}$$

Where $\boldsymbol{\tau}$ is a vector of joint torques, J_c is the contact Jacobian relating joint rates to end effector (foot) velocities, R_{BN} is the rotation matrix that rotates the inertial frame into the robot body frame, and $\boldsymbol{F}$ is the force exerted by the end effector. This relationship yields a fairly simple model of NABi-V2 as a floating rigid body with mass-less legs that transfer forces from the ground, as shown in Fig. 4.34. The lightweight leg design of NABi-V2 facilitates this mass-less leg model, which is computationally simple and does not require very accurate measurements of link mass and inertia. The systems presented in [48] and [51] also use the Jacobian relationship for similar reasons. Several controllers have been

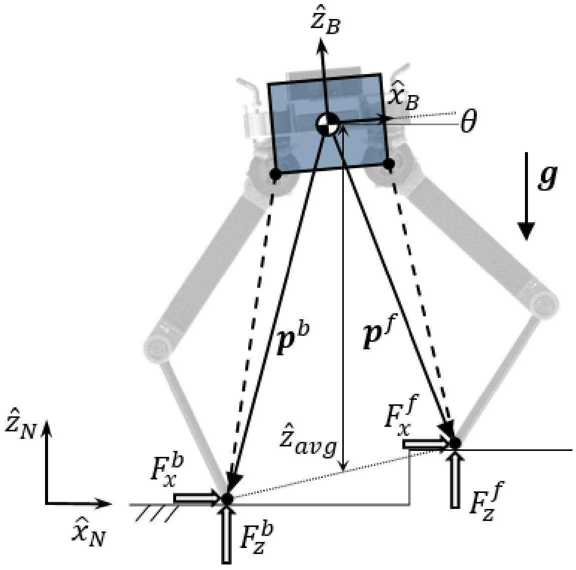

Figure 4.34: NABi-V2 modeled as a floating rigid body with mass-less legs that transfer ground reaction forces to the body.

implemented on NABi-2 to realize interesting locomotion such as pronking[72] its unique walking gait similar to that of NABi-1.[71]

Performance Presentation Similar to NABi-1, benefited from the unique non-anthropomorphic design, NABi-2 presents stable dynamic walking gait presented in Figure.4.35a

Taking advantage of the impact mitigation and high torque output capability of Panda BEAR modules, the robot is able to stably jump continuously at a height of approximately 15cm as illustrated in Fig. 4.35b.

While NABi-V2 demonstrates the effectiveness of high torque, low gear ratio actuation at performing dynamic motions that require compliant behavior, it is worth noting that this approach does sacrifice some of the benefits of using heavily geared electric actuators. Because the only way for NABi-V2 to counteract gravity is for the BEAR modules to contin-

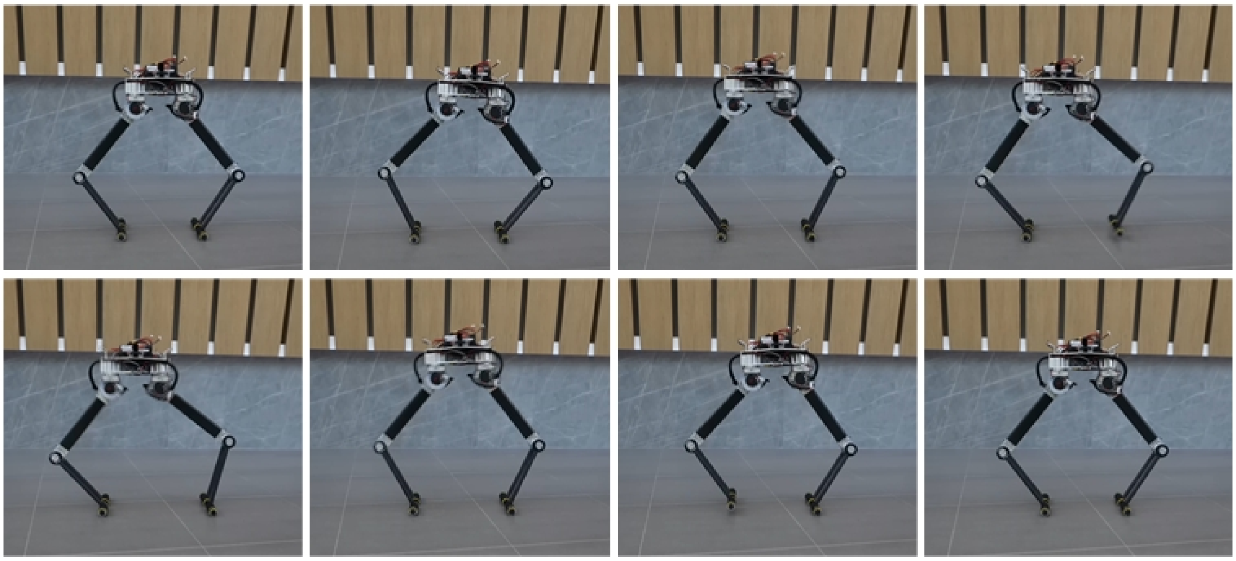

(a) NABi-2 walking.

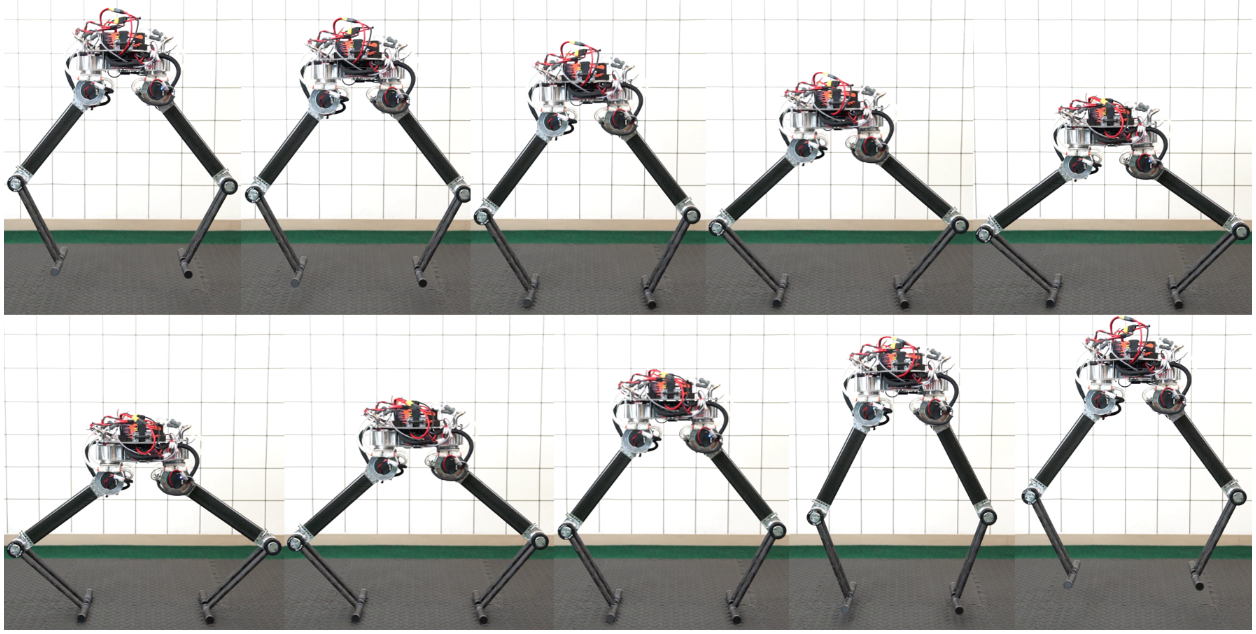

(b) NABi-2 pronking.

Figure 4.35: NABi-2 walking and jumping.

uously provide torque (and thus, current) at the joints, the nominal energy consumption of the system standing at idle is significantly higher than that of the similarly sized NABiRoS system, which uses conventional servos and can utilize the significant friction from the gearboxes in addition to the application of torque. Even though NABi-2 benefits a considerable amount in dynamic performance from the reduced leg inertia due to the application of parallel actuation, such configuration is not optimal compare to the serial configuration that NABiRoS adopted, as already compared and discussed in Section.3.2.2. And this factor significantly contributed the power consumption issue. However, when performing dynamic motions like pronking, it is possible for the BEAR module to actually regenerate significant amounts of current, something that is generally negligible on traditional servos. This means that NABi-V2 has the potential to be more efficient when in motion, while NABiRoS is more efficient when stationary. In any case, the benefits of the BEAR modules still outweigh the drawbacks, as NABiRoS was never able to fully realize proprioceptive force control as NABi-V2 is, despite it's series elastic leg design.

4.3.2 ALPHRED-2

4.3.2.1 Introduction to ALPHRED-2

In recent years, the legged robotics community has seen a large number of successful platforms capable of impressive dynamic locomotion. In particular, there have been a large number of quadrupedal platforms due to their favorable stability properties: ANYmal C from ANYbotics [3] employs IP67 rated hardware and custom SEA's in order to provide robust inspection and mobility in even the most extreme environments. Cheetah 3 from

MIT [6] demonstrates an impressive full 3D gallop at 3 m/s, popularizing the use of proprioceptive actuators [59] [31] for legged robotics. Lastly, Spot from Boston Dynamics [9] is capable of extremely robust walking in various terrains both indoors and out, and also can equip a single robotic arm to open doors and pick up small objects. With their ability to have robust mobility across different terrains, quadrupeds like these are starting to be deployed in surveillance and inspection applications that require such performance.

However, with out the help of an extra limb as a manipulator, these quadruped robots are typically in lack of the capability to handle applications that involve manipulation tasks, such as picking up a package or using tools. Because of this reason, most legged manipulation platforms are of the humanoid form factor. Boston Dynamic's Atlas [8] is one of the most capable humanoid robots, and has demonstrated robust walking/running, adept package manipulation, and even highly dynamic tumbling. Agility Robotics' Digit [56] is another human-like biped which is attempting to make autonomous package delivery a reality. In addition, there were a number of humanoid-like robots showcased at the DARPA Robotics Challenge (DRC) that demonstrated tasks such as driving a car, opening a door, using power tools, and going over extreme terrain. However, unlike quadrupeds, bipeds (e.g. humanoids) are not statically stable and require active balancing which makes their control much more difficult.

As presented in Section.4.3.1, NABi-2 is a unique bipedal robot platform that shins in locomotion stability and system simplicity. However, it is quite clear that NABi-2 is in lack of practicality. Meanwhile, as discussed above, it has been proven the mobility of quadruped robots and versatility of manipulator limbs on a mobile platform. Taking inspiration from these facts, the arms on NABi-2 is turned into the same limbs as its legs, and a omnidirectional quadruped called ALPHRED is born. APHRED stands for Autonomous Legged Personal Helper Robot with Enhanced Dynamics, and the concept was first test with a prototype actuated by traditional servo actuators called ALPHRED-1. The system developed during this work is the updated version called ALPHRED-2, powered by Panda BEAR modules at all joints. Succeeded from NABi, ALPHRED utilizes a non-traditional kinematic leg configuration by swapping lateral ab/adduction (typically achieved with a hip-roll DoF) with medial rotation (with a hip-yaw DoF) (Fig. 4.37). This modification sacrifices some of the dynamical benefits of the traditional configuration in order to provide a much greater range of motion. Combining the robot's large workspace with simple end-effectors allows the robot to have different operating modes to handle a multitude of tasks, providing ALPHRED with capabilities beyond those of current quadrupeds.

4.3.2.2 ALPHRED-2 System Presentation

Concept of Operation ALPHRED is a novel omnidirectional quadruped robotic system with multi-modal locomotion and various manipulation capabilities. As shown in Fig. 4.37, ALPHRED is composed of four identical limbs and a body structure, with details explained in the following subsections. To achieve highly dynamic locomotion and manipulation tasks, Panda BEAR modules are used at each joint for actuation.

ALPHRED's unique kinematics allow it to reconfigure into several different operational modes. Figure.4.38a shows ALPHRED in the very basic mode-the omnidirectional mode. In this mode the limbs of ALPHRED are asymmetrically spread out into a wide stance, pro-

Figure 4.36: ALPHRED crossing a cross walk with a package.

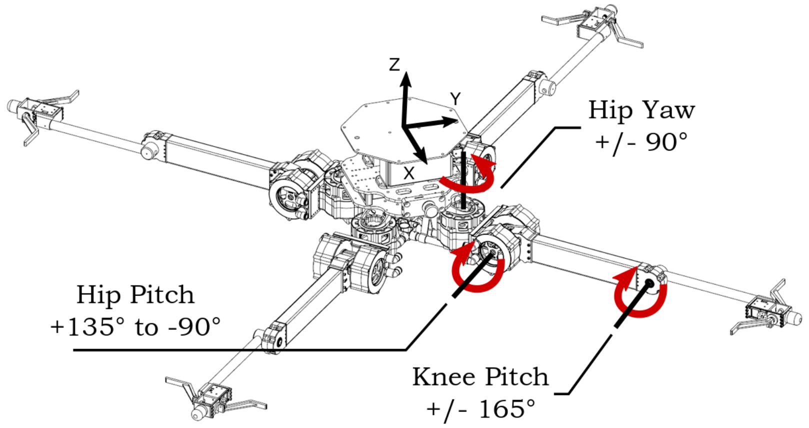

Figure 4.37: ALPHRED's unique kinematic configuration providing a large continous workspace.

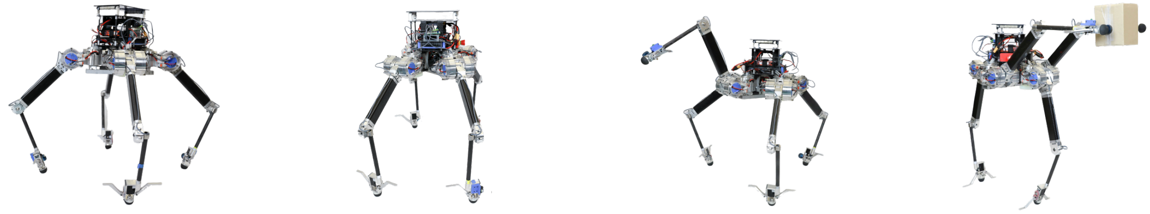

(a) Omnidirectional (b) Quadruped (c) Tripod (d) Biped

Figure 4.38: ALPHRED is a multi-modal locomotion quadruped mobile robot platform.

viding the robot a very big support polygon. ALPHRED can walk omnidirectionally in this mode, with various gaits, and it is very suitable for traveling over rough terrain and load bearing. Jumping and pronking is also performed under this mode. The omnidirectional mode is used to transition between modes and to accurately position the robot for manipulation tasks. The robot can switch into a more traditional quadrupedal mode, increasing the front-to-back and decreasing the left-to-right distance of the legs (Fig. 4.38b). In this mode the four limbs are grouped into two pairs, similar to other quadruped robots. With this setup, ALPHRED can move rapidly of a stable 1.5 m/s over real world terrain in its sagittal plane, utilizing dynamic gaits such as trot.

When comes to manipulation, ALPHRED can configure itself to the tripod mode or the bipedal mode, as shown respectively in Figure.4.38c and 4.38d. In scenarios that dual-arm manipulation is required, such as package pickup or delivery, ALPHRED can be put into the bipedal mode. ALPHRED's dual arm manipulation is capable of picking up and transporting boxes of various size and weight. This mode also has the potential to be used for bipedal walking as shown on the NABi-2 platform. The tripod mode can be used when only one limb is needed for the manipulation task, such as knocking on a door or pushing a button, or in other cases, enhanced stability is required during the manipulation, such as pushing a heavy object.

For improved efficiency on flat terrain, the robot can enter a wheeled mode by lowering itself onto passive caster wheels mounted on the bottom of its body as optional accessories. Once the robot is resting on the four wheels the robot uses its limbs to push itself, providing a Cost of Transport (CoT) of about 0.55 with 40% energy consumed by the computer, and it is far superior to that of most other legged robots.

Design ALPHRED is composed of four identical limbs that are attached to a central body in a radially symmetric distribution. The body of ALPHRED (Fig. 4.39) is comprised of an upper body which houses the electronics, and lower body frame which acts as the chassis. The lower body frame is the main structural piece to hold all other sub-assemblies together and provide the whole system with adequate rigidity. The lower body frame is a composite structure of carbon-fiber tubes and aluminum parts. All parts are joined together with epoxy such that

the whole lower body frame is one solid structure. The upper body is completely made out of carbon fiber, and is used to house the batteries, computer, and any additional sensors.

All parts on the ALPHRED body were designed to be lightweight while also ensuring that the structure does not interfere with the limbs' large kinematic workspace. The upper body structure without electronics and accessories weights only 0.63 kg and the lower body frame weights only 0.62 kg, resulting in a total weight of 1.25 kg, which is less than 7% of the total weight of ALPHRED.

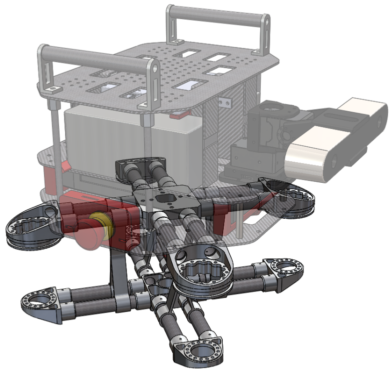

Figure 4.39: The transparent part is the upper body structure that houses the electronics and the solid part is the chassis of the robot.

ALPHRED's limbs have 3 DoF: hip yaw, hip pitch, and knee pitch (Fig. 4.37). These joints are actuated by proprioceptive BEAR modules [76] mounted at the hip to reduce limb inertia and mass. The knee and hip actuators use a parallel configuration, with the knee joint being driven by a belt transmission which runs through the carbon fiber leg structure and provides the joint with a range of motion that is nearly 360°, as shown in Fig. 4.40.

There is one extra actuated DoF at the foot of each limb. This DoF can be used to enhance ALPHRED's capabilities by attaching various accessory components. In the case shown in Fig. 4.40, a foot extension bar is attached to provide stability when in biped mode.

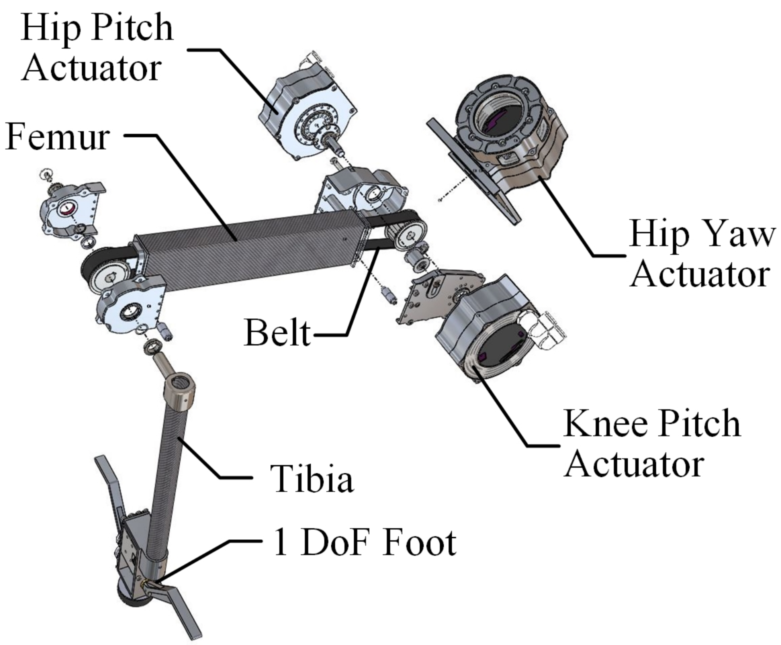

Figure 4.40: ALPHRED leg exploded view.

System Architecture The main computer is an off-the-shelf Intel NUC equipped with an Intel Core i7-6670HQ @ 2.60 GHz with 32 GB of RAM. ALPHRED's codebase is mostly written in Python, but utilizes external C/C++ libraries such as Eigen and Boost when applicable. ALPHRED runs an architecture tailored for simplicity and modularity to invite multiple developers to easily contribute to modular components that can be easily assembled, similar to the setup developed in [72].

ALPHRED has many concurrently running processes which include a motor communication thread, user input thread, finite state machine (FSM) thread, and a state estimation thread. All communication between threads is done using a custom shared memory library for the sharing of structured data. The motor communication process operates at 1000 Hz and is used as the interface between the controllers and actuators. The FSM process runs all of the high-level planners and controllers making it easy to integrate a new controller via a new state in the state machine. The user input process allows for tele-operation of the robot through a GPD (small handheld computer). Lastly, the state estimation process communicates with the VectorNav 200 IMU and uses the IMU-encoder sensor fusion approach described in [7] to provide full state estimation of the robot. This type of approach provides great flexibility in further developing ALPHRED as initially demonstrated in the past with incorporating vision and other sensor data into the architecture while minimally modifying the currently existing code [2].

4.3.2.3 Performance Presentation

Locomotion The primary gait used by ALPHRED is a trotting gait with swing and stance times ranging from 0.18-0.3 seconds. Using a 0.2 second swing and stance time ALPHRED can reliably walk at 1.0 m/s and achieve a turning rate of 0.5 rad/s.

From this experiment the cost of transport (CoT) was calculated to be 2.6, the CoT formula used is the same as the one presented in [5]. After lowering both the swing and stance time times to 0.18 seconds ALPHRED achieved a max velocity of 1.5 m/s.

Using the same trot gait, ALPHRED was able to successfully walk over an artificial obstacle course comprised of scattered blocks as obstacles ranging in height from 2-4 cm. In addition, the robot has also successfully walked around in the real world walking on side walks, streets, and dirt paths which also included terrain with slopes $> 15^\circ$

To demonstrate the speed and strength of the BEAR modules a single jump was performed by commanding all four limbs to go from the crouched to standing position in 0.05

seconds. The test resulted in a vertical jump of 0.7 m as measured from the top of the robot at its apex and the top of the robot in it's final standing pose. For controlled jumping, a pronking gait described in enabled the robot to move in the X and Y directions at 0.3 m/s.

The skating locomotion enabled ALPHRED to reach velocities of up to 2.1 m/s on smooth, flat ground using tele-operation. Interestingly, the limiting factor for skating seemed to be the low quality of the caster wheels, as the robot would experience significant deceleration during the swing/flight phase of the gait. However, a CoT as high as 0.55 (40% of power was used by the computer) was recorded, which is five times less than the one recorded during trotting.

Manipulation To test the robot's two limb manipulation we had the robot pick up and drop off packages that we continuously increased in size until failure. This resulted in the smallest package being 16 × 13.2 × 11 cm and the largest being 48 × 34.5 × 17.5 cm. A similar test was repeated with increasing weight, using a nominal package of size 31 × 21.5 × 14 cm. The weight test resulted in ALPHRED being able to pick up 3 Kg. Finally we tested what was the tallest height at which the robot could grab the nominal sized package from which resulted in a height of 1.02 m.

4.3.3 BRUCE

4.3.3.1 Introduction to BRUCE

The world is built by human and is meant to meet the needs and flavor of human beings. Although quadruped robots have shown promising potential of being great assistants for humans in the near future, it is still believed that humanoid robots have the ultimate privilege to be the best choice for daily life assistance. As coined by the architect Louis Sullivan, “form follows function”. For robots to best perform tasks within such an environment designed and built by human beings, a robot in the shape of a human should present the ultimate versatility.

However, the development of a humanoid robot system is one of the most complicated and difficult topics within the field of robotics. Despite the difficulty in the development of control algorithms, the availability of full-size humanoid robots is extremely limited. It can cost over $100k and take several years to develop a full-size humanoid robot even for labs well-equipped with all the fabrication and experimental equipment that is needed during the project, not to mention the complication and hardship of the project itself. Thus small-sized humanoid robots are the more viable choices for researchers in the related topics. Since these robots are scaled down to the size smaller than a kid, it is very easy to achieve adequate rigidity and robustness with the system, and the complicity and cost is manageable by most labs and research institutes. Even though they are actuated by low-speed high-torque servo actuators, their dynamic performance still outperform most existing full-size humanoid robots. Besides, the researchers are also relieved from safety concerns when working with such small robots.

Yet with the current quadruped robots presenting superior dynamic performance, the performance of those existing small humanoids are losing their qualification from the ever rising criteria. Based on the experiences from both legged systems NABi-2 and ALPHRED-2, it is reasonable to believe that the application of Proprioceptive Actuators can provide

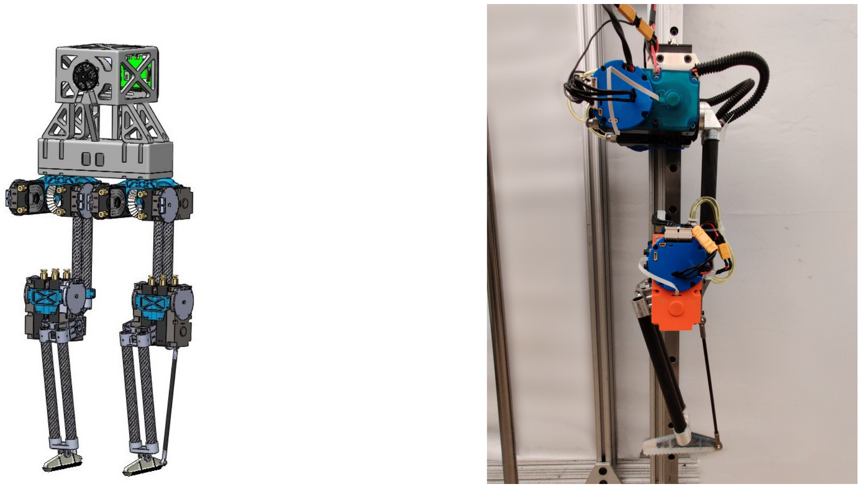

(a) CAD render of BRUCE lower body.

(b) Actual BRUCE leg built.

Figure 4.41: BRUCE rendering and actual build.

evolutionary changes to the dynamic performance of a small-sized humanoids robot. Thus BRUCE is as presented in the following section.

4.3.3.2 Design Presentation

BRUCE (Figure.4.41a) is a kid-size biped robot with 6 DoF in each leg. Currently one leg of BRUCE (Figure.4.41b) has been built for testing and experiments. The leg of BRUCE is in serial joint configuration with hybrid actuation configuration to take advantages of both choices, resulting in a compact and light weight leg design with very large range of motion that is similar to that of a human leg and optimal load distribution between the actuator for best efficiency.

The range of motion of BRUCE's leg is very close to, and in some joints better than, a human leg, as compared in Figure.4.42. The knee joint of BRUCE has a range of 130°, very similar to that of a human leg which is 140°. Different from the abduction joint of a

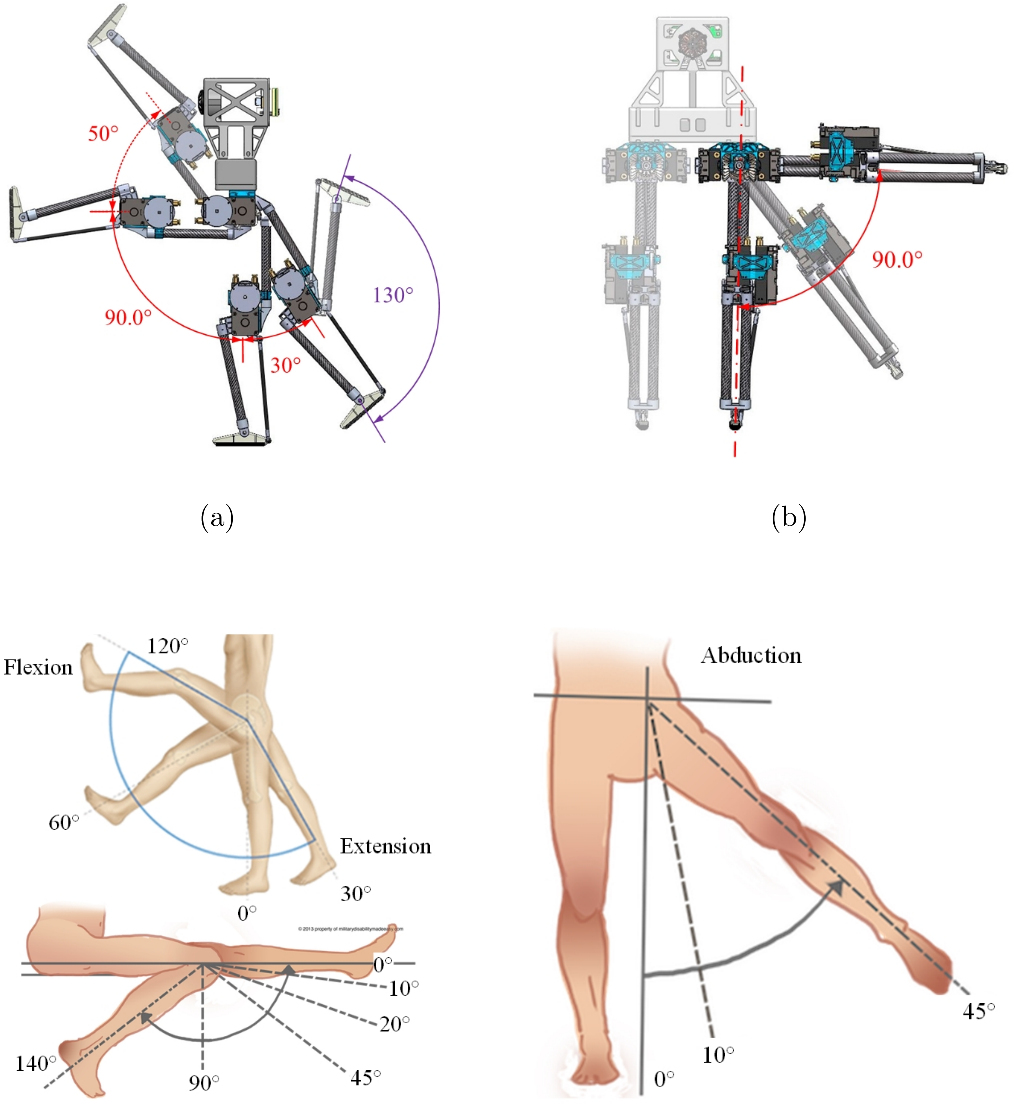

(a) (b)

(c) (d)

Figure 4.42: Comparison of the range of motion of BRUCE's leg with a human leg.

human which is mot symmetric to the sagittal plan, the abduction range of BRUCE's leg is symmetric regardless of collision with the other leg, with a super large range of 90° on each side, which is double of the 45° of a human leg. The BRUCE leg thigh has a extension range equal to a human leg, which is 30°, and a flexion of 140°, 20° beyond a human leg thigh flexion range. However due to interference constrains, the roll motion of the leg is very limited when its thigh is flexed into the last 50° range, but it can still be very useful for deep squads and high power jumps, as shown in Figure.4.43

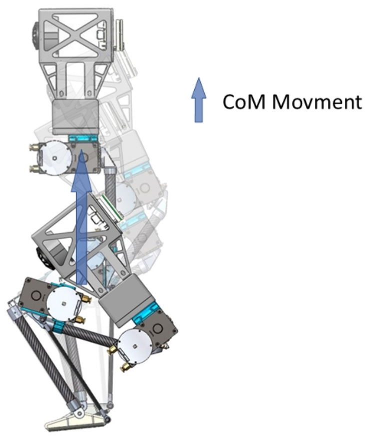

Figure 4.43: Large range of motion enables BRUCE to squad deep, and prepare for powerful jumps.

The mechanical design details of BRUCE's leg is presented in an exploded view (Figure.4.40). Except the yaw joint which is actuated by a traditional servo motor, all the other 5 DoF in the leg is actuated by Koala BEAR modules. The hip assembles into a 2 DoF parallel actuation, realized by a bevel gear differential mechanism. This design maximize the available torque on the hip pitch motion with up to twice of the torque a single Koala BEAR provides, while keep the flexibility of optimal load distribution between the pitch and roll motion. This is very important as the hip pitch motion is the most engaged during normal locomotion, while the parallel configuration enables a very compact design. The draw back is that singularity emerges at extreme positions such as when the pitch is 90° with the thigh being parallel to the transverse plane, which in fact is not a concerning factor as this is very far out of BRUCE's normal operation range. The knee actuator is located right at the knee joint, resulting in a serial actuation at the joint. This prevented the mechanical antagonism situation as in ALPHRED-2, and makes sure a relatively higher actuation efficiency. The last DoF of the leg is at the pitch of the ankle, providing an extra actuated DoF for stance balancing. The foot of BRUCE is designed such

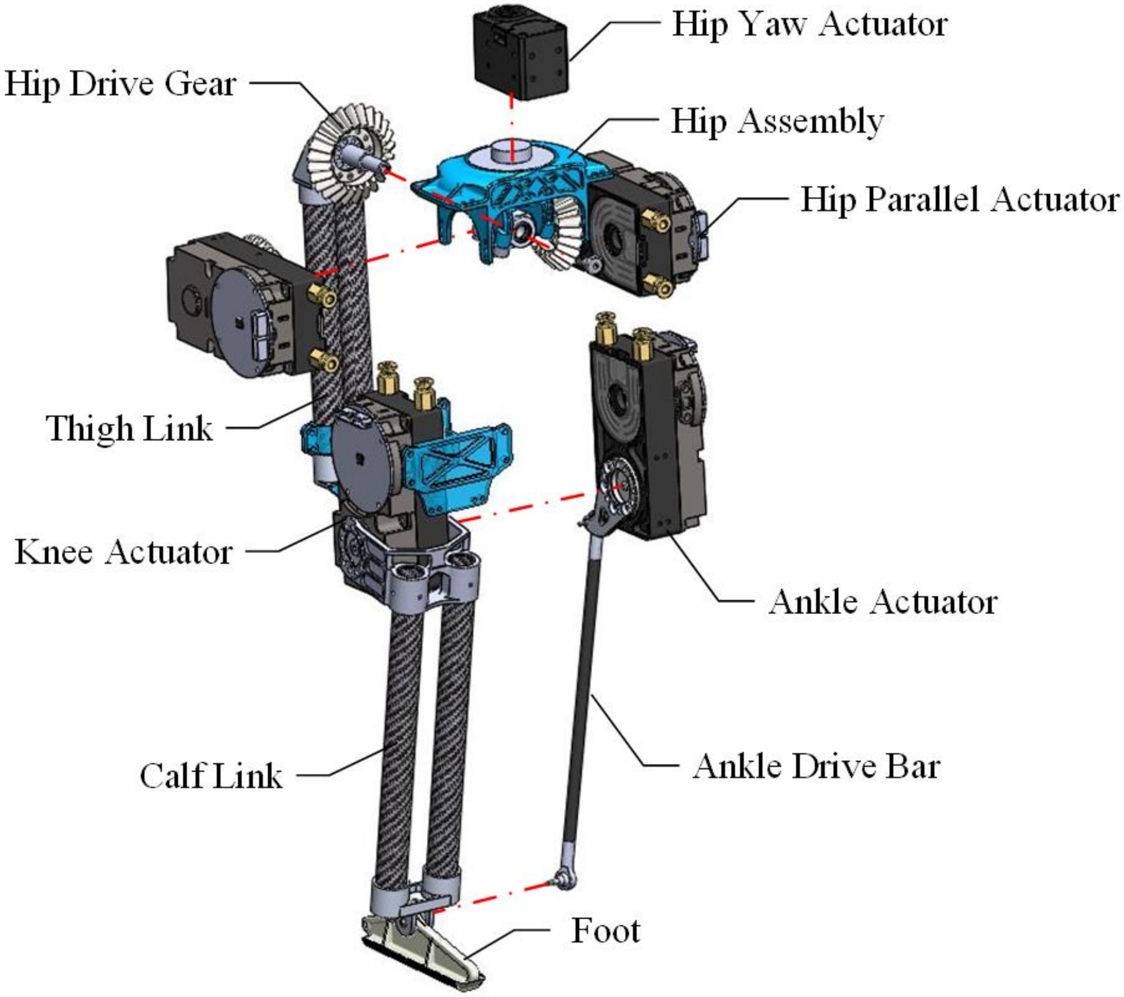

Figure 4.44: BRUCE leg exploded view.

that its contact with ground is a line, so that a roll actuation on the ankle can be omitted. The actuator of the ankle is mounted on the thigh link, driving the ankle joint with a four bar linkage mechanism. The actuation of the ankle joint is in parallel with the knee joint. By decoupling the ankle joint and its actuator and dismounting the actuator on the thigh link, the inertia of the calf link becomes very low, and the benefits being better dynamic performance and impact response.

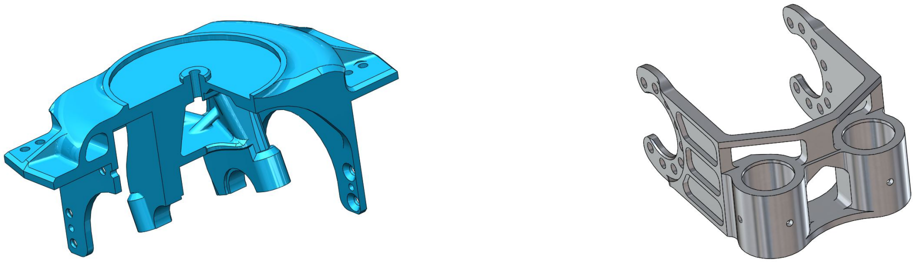

(a) Hip Assembly bracket

(b) Knee bracket

Figure 4.45: Multiple parts on BRUCE are optimized with topology study to seek design of low-weight strong parts.

To push the weight of BRUCE to the lowest extreme while maintain high rigidity, topology analysis is highly involved in the optimization of parts, such as the Hip Assembly bracket (Fig.4.45a) and the knee bracket (Fig.4.45b) on the calf link. Special material choices are also made for the same reason. The Hip Assembly bracket, Ankle Actuator bracket as well as the foot are plastic made with Form 2 SLS 3D printer. The Thigh Link and Calf Link are composed of aluminum parts on both ends and carbon fiber tubing in the middle. The major body of Ankle Drive Bar is a thin aluminum tube.

BRUCE will have a customized efficient high pressure regenerative turbine pump (Fig.4.46), which can output a theoretical maximum pressure at 6W. BRUCE is powered by two 4S Li-po battery connected in serial. The robot will be controlled by the newly release Raspberry Pi 4 with ROS system.

Figure 4.46: Mini high pressure regenerative turbine pump for small robotic system liquid cooling purposes.

4.3.3.3 Current Status & Future Development

Currently BRUCE is still at a preliminary development stage. The basic kinematics and dynamic motion capability has been tested and proven with experimental tests run on jigs. BRUCE is meant to serve as a replacement for DARwIn-OP with superior dynamic performance capabilities as a result of the application of Proprioceptive Quasi-Direct Drive actuators.

BRUCE is planned to be developed into an open-source platform for research, education, out-reach activities and more. BRUCE is supposed to present highly dynamic motion capabilities that are superior to any existing humanoid robot platform of similar size. This could open up many new possibilities and opportunities, such as much more evolved tasks for life assistance, human inter-activities, and entertainment, which could eventually lead to results that can bring robots closer to humans and their lives.

CHAPTER 5

Discussion And Conclusion

The research work done in this dissertation is to explore the implementation of Proprioceptive Quasi-Direct Drive Actuators in dynamic robotic systems. Several distinguishing different robotic systems covering both compact small robotic systems and practically sized robots are developed during the implementation. To better estimate, understand, assist, guide and evaluate the implementation results, a couple of theoretical innovations and contributions are generated.

In the theory development of this dissertation, the performance properties and characteristics of BLDC motors are reviewed, as well as the influence on actuation transparency from the reflective inertia of a transmission. Then the actuator characteristics and general design guidelines for Proprioceptive Quasi-Direct Drive Actuators are provided.

To contribute to the the systems that are developed within this work, theoretical contributions are also made in the topics of underactuated mechanism and actuation configuration of fully actuated systems. Underactuated mechanism with embedded mechanical intelligence is commonly employed to vastly reduce the actuated DoF and thus reduce the complexity, size and weight of a robotic system, especially for small size systems that being compact and light-weight is fairly important. Mechanical intelligence is studied form the angle of energy and a potential energy flow theory is provided to explain this feature. The theory is then proved with experiment on DAnTE system. The actuation configuration is one of the basics that significantly determine the performance of a robot. Thus a comprehensive review on joint configuration and actuation chain is done to discuss the mechanical antagonism and the most efficient choice in different cases.

As new actuation technologies are developed alongside better control approaches, we are witnessing the introduction of more dynamically moving robots. Since many of these robots also physically interact with their surroundings, but now at a higher velocity compared to the previously quasi-static systems, it is important to be able to quantitatively analyze the effects of these collisions. Such analysis can help prevent mechanical damage to the platform as well as be an integral factor in an algorithm.

Impact Transfer Factors are a beginning step in finding metrics to quantify and ultimately analyze physical impacts that occur on robots. We start from the very basic definition of an impact and mathematically derive two factors that represent the sensitivity to impacts at the joints, given a 'unit impact' applied at a given angle at the end-effector. A series of simulations were conducted for both the Impact Force Transfer Factor and the Impact Velocity Transfer Factor, and the latter's behavior was verified on an experiment conducted on a physical robot.

Going forward, the insights obtained and theory behind ITF can be integrated in current motion planning algorithms for our legged robots and manipulators, such as locomotion optimization algorithms [2] to find new swing leg trajectories and end-effector attack angles that prolong the life of the mechanical parts while having minimal performance drop in other criterion. With our proprioceptive manipulators and grippers, force sensing could be enhanced as ITF provides information on how an intentional collision should be created to be even more sensitive to the environment.

Various hardware pieces and systems have been developed during the worked covered by this dissertation. As a variation from the Proprioceptive Quasi-Direct Drive Actuator module, Panda BEAR, developed by another researcher at RoMeLa, a small size version called Koala BEAR is developed for applications like robotic hands, desktop manipulators and small legged robots. As of the application of these two actuators in the robots developed during this work, the Koala BEAR and its concept prototype is used on DAnTE 1, DAnTE 2 and BRUCE, while Panda BEAR is applied to actuate bigger systems which are NABi-2 and ALPHRED-2.

DAnTE 1 is a three-finger under actuated robotic hand. It is designed with embedded mechanical intelligence and current based live force sensing and inherent compliance. Each finger on DAnTE 1 is under actuated and driven by only one actuation module. The actuation module is the concept prototype of the Koala BEAR module developed within the scope of this dissertation, and comprises a high torque BLDC motor with a small speed reduction ratio of about only 1:8. The actuation module provides excellent inherent compliance to all the fingers, making it possible to directly sense and control the force on the finger by monitoring and controlling the torque current in the motor. The tendon driven fingers on DAnTE 1 are a simplified biomimetic design of human fingers. While being under actuated, the trajectory of the finger is controlled by the mechanical intelligence such that when approaching the goal object, the finger always follows a preferred trajectory that goes through most of its reachable area. The mechanical intelligence also provides the finger with automatic object fitting ability, which makes the finger to always use the best gesture for grabbing the object. The mechanical intelligence in the underactuated finger mechanism is achieved and analyzed under the guidance of a potential energy flow theory developed in with in the work of this dissertation. A velocity controller is designed and applied to achieve precise position tracking and a compliance controller is designed and applied on DAnTE 1 system for grabbing tasks with high requirement on force control ability. DAnTE 1 has also shown great performance on dexterous grasping.

DAnTE 2 is an upgraded version, successor to DAnTE 1. The tendon transmission system is replaced with multi-DoF rigid linkages, and the actuation modules are upgraded to Koala BEAR modules. The finger extension trajectory under free-load condition is also modified a little to increase mechanical efficiency and focus more on grabbing tasks at the sacrifice of gesture posing dexterity. The major contribution of the updates is to turn it into a robust and reliable system that is maintenance free and can be dedicated to further research development.

NABi-2 is a unique bipedal platform that deviates from traditional humanoid design in an attempt to provide a simple and robust platform for dynamic locomotion using proprioception and force control. The system's morphology, actuation, and software architecture are all designed around this premise, resulting in the adoption of things like non-anthropomorphic leg design, Panda BEAR modules, and concurrently run software processes. The outcome of this particular combination of features yielded a versatile legged platform that is capable of performing pronking using a Raibert-style compositional controller, a feat typically reserved for systems with mechanical springs or other forms of physical compliance. However, it was also found that the inherent compliance of NABi-2 made traditional time and position dependent walking difficult, suggesting the advantages of using event-based controllers with the BEAR modules. The back-drivable nature of the BEAR modules on NABi-V2 provide proprioceptive capabilities that are utilized when determining touchdown in the event-based locomotion algorithms. However, the current touchdown detection implementation is relatively simplistic, relying on the activation of a couple of binary conditions to determine the occurring of a touchdown event. With the help of ITF, it is prudent to develop an improved form of touchdown detection that fuses the motor current, encoder position, and time. In the future, NABi-2 will be equipped with conventionally driven arms as planned, and can be used to study full body controllers that combine the force control of the legs with the position control of the arms. Still, NABi-V2 represents a step towards the development of fully realized humanoids that have the potential to be used in a variety of unstructured environments and scenarios taking advantages of Proprioceptive Quasi-Direct Drive Actuation.

Inspired and encouraged by the success of NABi-2, the application of BEAR modules is then taken one step further into a quadruped robot called ALPHRED-2. This platform utilizes a unique kinematic design giving it the ability to operate in different modes for both transportation and manipulation. We believe that we have successfully shown that this configuration change coupled with high torque proprioceptive actuators keeps the benefits of quadrupedal robots, stability and reliability, while also providing capabilities that go beyond that of traditional quadrupeds.

ALPHRED-2 can travel in multiple modes using various gaits. ALPHRED is capable of continuously walking over real world terrain with a speed of 1 m/s and it can reach a maximum walking velocity of 1.5 m/s. When put in caster mode, ALPHRED-2 can travel along smooth terrain with CoT of 0.55 and a speed up to 2.1m/s. ALPHRED-2 is also capable of multiple manipulation tasks, which no other quadruped robot can achieve without the help of any extra manipulator. By utilizing the tripod and biped mode, one or two limbs can be transferred to manipulation limbs from locomotion limbs. In tripod mode, the manipulation limb can be used for inspection or heavy duty manipulation tasks, while in biped mode, the two manipulation limbs can work together to pickup boxes with a wide range of sizes. ALPHRED-2 is a reliable platform for many future topics, such as integrating a vision system on to the platform to incorporate high level path planning as well as fully automating the package pick up and drop off.

Finally, as an outlook of the work presented in this dissertation, in the interest of building some foundation for future exploration carried on by colleagues, an open-source kid-sized humanoid robot platform BRUCE is presented. The kinematics of BRUCE's leg is optimized with the integration of the actuation chain analysis in Section.3.2.2, resulting in a hybrid configuration for maximum efficiency with compact design and a large range of motion similar to that of a human. Koala BEAR modules are applied to 4 out of 5 DoF per leg and a customized miniature regenerative turbine pump is developed for actuator liquid cooling circulation.

The work presented in this dissertation contains contribution in both theoretical development and innovative hardware creation. The properties of Proprioceptive Quasi-Direct Drive Actuators are studies and compared to those of the traditional position controlled actuators as well as Series Elastic Actuators. The application of such actuators involves a large amount of hardware and system innovation, and several theories are developed to assist and analyze the hardware development. The results acquired from various experiments with the systems also validate the developed theories.

My understanding of one's Ph.D. career, especially in the field of engineering that often times not only creating general theories but also physical systems, shows its greatest value if it becomes part of the irritation of the subject. Thus I hope the completion of my Ph.D. degree is not purely the conclusion on the modest amount of new knowledge that I think I've contributed to the subject, but also a somewhat paved gateway to future exploration carried on by others, physically with the help of all the robots I've built during these amazingly enjoyable and unforgettable years I've spent in RoMeLa, a dreamland for robotics Ph.D. students.

Bibliography

[1] Andy Abate, Jonathan W Hurst, and Ross L Hatton. Mechanical antagonism in legged robots. In *Robotics: Science and Systems*, 2016.

[2] Min Sung Ahn, Hosik Chae, and Dennis W Hong. Stable, autonomous, unknown terrain locomotion for quadrupeds based on visual feedback and mixed-integer convex optimization. In *2018 IEEE/RSJ International Conference on Intelligent Robots and Systems (IROS)*, pages 3791–3798. IEEE, 2018.

[3] Anybotics. ANYmal C. http://www.anybotics.com/anymal-legged-robot/. Accessed: 2019-08-20.

[4] Haruhiko Asada. Dynamic analysis and design of robot manipulators using inertia ellipsoids. In *Proceedings. 1984 IEEE International Conference on Robotics and Automation*, volume 1, pages 94–102. IEEE, 1984.

[5] Pranav A Bhounsule, Jason Cortell, and Andy Ruina. Design and control of ranger: an energy-efficient, dynamic walking robot. In *Adaptive Mobile Robotics*, pages 441–448. World Scientific, 2012.

[6] G. Bledt, M. J. Powell, B. Katz, J. Di Carlo, P. M. Wensing, and S. Kim. Mit cheetah 3: Design and control of a robust, dynamic quadruped robot. In *2018 IEEE/RSJ International Conference on Intelligent Robots and Systems (IROS)*, pages 2245–2252, Oct 2018.

[7] Michael Bloesch, Marco Hutter, Mark A Hoepflinger, Stefan Leutenegger, Christian Gehring, C David Remy, and Roland Siegwart. State estimation for legged robots-consistent fusion of leg kinematics and imu. *Robotics*, 17:17–24, 2013.

[8] Boston Dynamics. Atlas: The Worlds Most Dynamic Humanoid. https://www.bostondynamics.com/atlas. Accessed: 2019-08-20.

[9] Boston Dynamics. Spot: Good Things Come in Small Packages. https://www.bostondynamics.com/spot. Accessed: 2019-08-20.

[10] Vishalini Bundhoo and Edward J Park. Design of an artificial muscle actuated finger towards biomimetic prosthetic hands. In *Advanced Robotics, 2005. ICAR'05. Proceedings., 12th International Conference on*, pages 368–375. IEEE, 2005.

[11] Tianjian Chen, Maximilian Haas-Heger, and Matei Ciocarlie. Underactuated hand design using mechanically realizable manifolds. In *2018 IEEE International Conference on Robotics and Automation (ICRA)*, pages 7392–7398. IEEE, 2018.

[12] Geckodrive Motor Controls. Stepper motor basics. https://www.geckodrive.com/support/step-motor-basics/speed-torque.html.

[13] Mark R Cutkosky. On grasp choice, grasp models, and the design of hands for manufacturing tasks. *IEEE Transactions on robotics and automation*, 5(3):269–279, 1989.

[14] Clarence W De Silva. *Modeling and control of engineering systems.* Crc Press, 2009.

[15] Aaron M Dollar and Robert D Howe. Simple, robust autonomous grasping in unstructured environments. In *Robotics and Automation, 2007 IEEE International Conference on*, pages 4693–4700. IEEE, 2007.

[16] Vladimir Eliseev and Yury Vetyukov. Effects of deformation in the dynamics of belt drive. *Acta Mechanica*, 223(8):1657–1667, 2012.

[17] Sepehr Ghassemi and Dennis Hong. Investigation of a novel continuously rotating knee mechanism for legged robots. In *2018 15th International Conference on Ubiquitous Robots (UR)*, pages 130–135. IEEE, 2018.

[18] Steven Giewont and Ferat Sahin. Delta-quad: an omnidirectional quadruped implementation using parallel jointed leg architecture. In *2017 12th System of Systems Engineering Conference (SoSE)*, pages 1–6. IEEE, 2017.

[19] Kevin G Gim, Joohyung Kim, and Katsu Yamane. Design and fabrication of a bipedal robot using serial-parallel hybrid leg mechanism. In *2018 IEEE/RSJ International Conference on Intelligent Robots and Systems (IROS)*, pages 5095–5100. IEEE, 2018.

[20] David Gouaillier, Vincent Hugel, Pierre Blazevic, Chris Kilner, Jérôme Monceaux, Pascal Lafourcade, Brice Marnier, Julien Serre, and Bruno Maisonnier. Mechatronic design of nao humanoid. In *2009 IEEE International Conference on Robotics and Automation*, pages 769–774. IEEE, 2009.

[21] Markus Grebenstein, Alin Albu-Schäffer, Thomas Bahls, Maxime Chalon, Oliver Eiberger, Werner Friedl, Robin Gruber, Sami Haddadin, Ulrich Hagn, Robert Haslinger, et al. The dlr hand arm system. In *Robotics and Automation (ICRA), 2011 IEEE International Conference on*, pages 3175–3182. IEEE, 2011.

[22] Inyong Ha, Yusuke Tamura, Hajime Asama, Jeakweon Han, and Dennis W Hong. Development of open humanoid platform darwin-op. In *SICE annual conference 2011*, pages 2178–2181. IEEE, 2011.

[23] HRNT Harrison and Trevor Nettleton. *Principles of engineering mechanics.* Butterworth-Heinemann, 1994.

[24] HOOSHANG Hemami. A state space model for interconnected rigid bodies. *IEEE Transactions on Automatic Control*, 27(2):376–382, 1982.

[25] Victor Albert Walter Hillier and Peter Coombes. *Hillier's fundamentals of motor vehicle technology.* Nelson Thornes, 2004.

[26] Kazuo Hirai, Masato Hirose, Yuji Haikawa, and Toru Takenaka. The development of honda humanoid robot. In *Proceedings. 1998 IEEE International Conference on Robotics and Automation (Cat. No. 98CH36146)*, volume 2, pages 1321–1326. IEEE, 1998.

[27] Joshua Hooks and Dennis Hong. Implementation of a versatile 3d zmp trajectory optimization algorithm on a multi-modal legged robotic platform. In *2018 IEEE/RSJ International Conference on Intelligent Robots and Systems (IROS)*, pages 3777–3782. IEEE, 2018.

[28] Marco Hutter, Christian Gehring, Michael Bloesch, Mark A Hoepflinger, C David Remy, and Roland Siegwart. Starleth: A compliant quadrupedal robot for fast, efficient, and versatile locomotion. In *Adaptive Mobile Robotics*, pages 483–490. World Scientific, 2012.

[29] Marco Hutter, Christian Gehring, Dominic Jud, Andreas Lauber, C Dario Bellicoso, Vassilios Tsounis, Jemin Hwangbo, Karen Bodie, Peter Fankhauser, Michael Bloesch, et al. Anymal-a highly mobile and dynamic quadrupedal robot. In *2016 IEEE/RSJ International Conference on Intelligent Robots and Systems (IROS)*, pages 38–44. IEEE, 2016.

[30] Jeffrey Yu Xiaoguang Zhang Taoyuanmin Zhu Hosik Chae Joshua Hooks, Min Sung Ahn and Dennis Hong. Alphred: A multi-modal operations quadruped robot for package delivery applications. Submitted to ICRA 2020.

[31] Gavin Kenneally, Avik De, and Daniel E Koditschek. Design principles for a family of direct-drive legged robots. *IEEE Robotics and Automation Letters*, 1(2):900–907, 2016.

[32] Oussama Khatib. A unified approach for motion and force control of robot manipulators: The operational space formulation. *IEEE Journal on Robotics and Automation*, 3(1):43–53, 1987.

[33] Scott Kuindersma, Robin Deits, Maurice Fallon, Andrés Valenzuela, Hongkai Dai, Frank Permenter, Twan Koolen, Pat Marion, and Russ Tedrake. Optimization-based locomotion planning, estimation, and control design for the atlas humanoid robot. *Autonomous Robots*, 40(3):429–455, 2016.

[34] Vikash Kumar, Zhe Xu, and Emanuel Todorov. Fast, strong and compliant pneumatic actuation for dexterous tendon-driven hands. In *Robotics and Automation (ICRA), 2013 IEEE International Conference on*, pages 1512–1519. IEEE, 2013.

[35] Thierry Laliberté, Lionel Birglen, and Clement Gosselin. Underactuation in robotic grasping hands. *Machine Intelligence & Robotic Control*, 4(3):1–11, 2002.

[36] Dong-Hyuk Lee, Uikyum Kim, Hosang Jung, and Hyouk Ryeol Choi. A capacitive-type novel six-axis force/torque sensor for robotic applications. *IEEE Sensors Journal*, 16(8):2290–2299, 2016.

[37] Touzhu Li and Gordon Slemon. Reduction of cogging torque in permanent magnet motors. *IEEE Transactions on magnetics*, 24(6):2901–2903, 1988.

[38] Xuan Lin, Hari Krishnan, Yao Su, and Dennis W. Hong. Multi-limbed robot vertical two wall climbing based on static indeterminacy modeling and feasibility region analysis. *2018 IEEE/RSJ International Conference on Intelligent Robots and Systems (IROS)*, pages 4355–4362, 2018.

[39] Sebastian Lohmeier, Thomas Buschmann, and Heinz Ulbrich. Humanoid robot lola. In *2009 IEEE International Conference on Robotics and Automation*, pages 775–780. IEEE, 2009.

[40] Kevin M.. Lynch and Frank Chongwoo Park. *Modern Robotics: Mechanics, Planning, and Control.* Cambridge University Press, 2017.

[41] Peter Lynwander. *Gear drive systems: Design and application.* CRC Press, 2019.

[42] Luis G Maqueda, Abdel-Nasser A Mohamed, and Ahmed A Shabana. Use of general nonlinear material models in beam problems: application to belts and rubber chains. *Journal of Computational and Nonlinear Dynamics*, 5(2):021003, 2010.

[43] Thomas H Massie, J Kenneth Salisbury, et al. The phantom haptic interface: A device for probing virtual objects. In *Proceedings of the ASME winter annual meeting, symposium on haptic interfaces for virtual environment and teleoperator systems*, volume 55, pages 295–300. Citeseer, 1994.

[44] Jouni Mattila, Janne Koivumäki, Darwin G Caldwell, and Claudio Semini. A survey on control of hydraulic robotic manipulators with projection to future trends. *IEEE/ASME Transactions on Mechatronics*, 22(2):669–680, 2017.

[45] Helmut Moczala, Jurgen Draeger, Hermann Krauß, Helmut Schock, and Siegfried Tillner. *Small electric motors.* IET, 1998.

[46] Andrew Yeh Ching Nee. *Handbook of manufacturing engineering and technology.* Springer, 2015.

[47] Shimon Y Nof. *Handbook of industrial robotics.* John Wiley & Sons, 1999.

[48] Hae-Won Park, Sangin Park, and Sangbae Kim. Variable-speed quadrupedal bounding using impulse planning: Untethered high-speed 3d running of mit cheetah 2. In *2015 IEEE International Conference on Robotics and Automation (ICRA)*, pages 5163–5170. IEEE, 2015.

[49] Jack Phillips. *Freedom in Machinery: Introducing Screw Theory; Jack Phillips.* Cambridge University Press, 1984.

[50] François Pierrot, C Reynaud, and Alain Fournier. Delta: a simple and efficient parallel robot. *Robotica*, 8(2):105–109, 1990.

[51] Jerry Pratt, Chee-Meng Chew, Ann Torres, Peter Dilworth, and Gill Pratt. Virtual model control: An intuitive approach for bipedal locomotion. *The International Journal of Robotics Research*, 20(2):129–143, 2001.

[52] Marc Raibert, Kevin Blankespoor, Gabriel Nelson, and Rob Playter. Bigdog, the rough-terrain quadruped robot. *IFAC Proceedings Volumes*, 41(2):10822–10825, 2008.

[53] Marc H Raibert and John J Craig. Hybrid position/force control of manipulators. *Journal of Dynamic Systems, Measurement, and Control*, 103(2):126–133, 1981.

[54] Alireza Ramezani, Jonathan W Hurst, Kaveh Akbari Hamed, and Jessy W Grizzle. Performance analysis and feedback control of atrias, a three-dimensional bipedal robot. *Journal of Dynamic Systems, Measurement, and Control*, 136(2), 2014.

[55] Joao Ramos, Benjamin Katz, Meng Yee Michael Chuah, and Sangbae Kim. Facilitating model-based control through software-hardware co-design. In *2018 IEEE International Conference on Robotics and Automation (ICRA)*, pages 566–572. IEEE, 2018.

[56] Agility Robotics. Meet digit: The newest robot from agility robotics. `https://www.agilityrobotics.com/meet-digit`.

[57] Claudio Semini, Nikos G Tsagarakis, Emanuele Guglielmino, Michele Focchi, Ferdinando Cannella, and Darwin G Caldwell. Design of hyq–a hydraulically and electrically actuated quadruped robot. *Proceedings of the Institution of Mechanical Engineers, Part I: Journal of Systems and Control Engineering*, 225(6):831–849, 2011.

[58] Sangok Seok, Albert Wang, Meng Yee Chuah, David Otten, Jeffrey Lang, and Sangbae Kim. Design principles for highly efficient quadrupeds and implementation on the mit cheetah robot. In *2013 IEEE International Conference on Robotics and Automation*, pages 3307–3312. IEEE, 2013.

[59] Sangok Seok, Albert Wang, David Otten, and Sangbae Kim. Actuator design for high force proprioceptive control in fast legged locomotion. In *2012 IEEE/RSJ International Conference on Intelligent Robots and Systems*, pages 1970–1975. IEEE, 2012.

[60] B Siciliano, L Sciavicco, L Villani, and G Oriolo. *Robotics–Modelling, Planning and Control. Advanced Textbooks in Control and Signal Processing Series.* London, UK: Springer-Verlag, 2009.

[61] Johan Tegin and Jan Wikander. Tactile sensing in intelligent robotic manipulation–a review. *Industrial Robot: An International Journal*, 32(1):64–70, 2005.

[62] Nikolaos G Tsagarakis, Darwin G Caldwell, Francesca Negrello, Wooseok Choi, Lorenzo Baccelliere, Vo-Gia Loc, J Noorden, Luca Muratore, Alessio Margan, Alberto Cardellino, et al. Walk-man: A high-performance humanoid platform for realistic environments. *Journal of Field Robotics*, 34(7):1225–1259, 2017.

[63] Nathan T Ulrich. Grasping with mechanical intelligence. *Technical Reports (CIS)*, page 846, 1989.

[64] Patrick M Wensing, Albert Wang, Sangok Seok, David Otten, Jeffrey Lang, and Sangbae Kim. Proprioceptive actuator design in the mit cheetah: Impact mitigation and high-bandwidth physical interaction for dynamic legged robots. *IEEE Transactions on Robotics*, 33(3):509–522, 2017.

[65] Jens Wittenburg. *Dynamics of systems of rigid bodies*, volume 33. Springer-Verlag, 2013.

[66] Chang-liang Xia. *Permanent magnet brushless DC motor drives and controls*. John Wiley & Sons, 2012.

[67] Taoyuanmin Zhu Xiaoguang Zhang, Min Sung Ahn and Dennis Hong. Impact transfer factors: An approach to quantitatively analyze impacts for dynamic robotic systems. Submitted to ICRA 2020.

[68] Seung-Joon Yi, Stephen McGill, Larry Vadakedathu, Qin He, Inyong Ha, Jeakwon Han, Hyunjong Song, Michael Rouleau, Dennis Hong, and Daniel D Lee. Thor-op humanoid robot for darpa robotics challenge trials 2013. In *2014 11th International Conference on Ubiquitous Robots and Ambient Intelligence (URAI)*, pages 359–363. IEEE, 2014.

[69] Hanna Yousef, Mehdi Boukallel, and Kaspar Althoefer. Tactile sensing for dexterous in-hand manipulation in robotics—a review. *Sensors and Actuators A: physical*, 167(2):171–187, 2011.

[70] Jeffrey Yu, Joshua Hooks, Sepehr Ghassemi, and Dennis Hong. Exploration of turning strategies for an unconventional non-anthropomorphic bipedal robot. In *ASME 2017 International Design Engineering Technical Conferences and Computers and Information in Engineering Conference*. American Society of Mechanical Engineers Digital Collection, 2017.

[71] Jeffrey Yu, Joshua Hooks, Sepehr Ghassemi, Alexandra Pogue, and Dennis Hong. Investigation of a non-anthropomorphic bipedal robot with stability, agility, and simplicity. In *2016 13th International Conference on Ubiquitous Robots and Ambient Intelligence (URAI)*, pages 11–15. IEEE, 2016.

[72] Jeffrey Yu, Joshua Hooks, Xiaoguang Zhang, Min Sung Ahn, and Dennis Hong. A proprioceptive, force-controlled, non-anthropomorphic biped for dynamic locomotion. In *2018 IEEE-RAS 18th International Conference on Humanoid Robots (Humanoids)*, pages 1–9. IEEE, 2018.

[73] Xiaoguang Zhang and Dennis W Hong. Micro power multiplexer, a compact device that controls mechanical power flow. In *ASME 2017 International Design Engineering Technical Conferences and Computers and Information in Engineering Conference*. American Society of Mechanical Engineers Digital Collection, 2017.

[74] Xiaoguang Zhang, Taoyuanmin Zhu, Itsui Yamayoshi, and Dennis Hong. A force controlled under actuated robotic hand with mechanical intelligence and proprioceptive compliant actuation. In *2018 IEEE-RAS 18th International Conference on Humanoid Robots (Humanoids)*, pages 1–8. IEEE, 2018.

[75] Yuan-Fang Zheng and Hooshang Hemami. Mathematical modeling of a robot collision with its environment. *Journal of Robotic Systems*, 2(3):289–307, 1985.

[76] Taoyuanmin Zhu, Joshua Hooks, and Dennis Hong. Design, modeling, and analysis of a liquid cooled proprioceptive actuator for legged robots. In *2019 IEEE/ASME International Conference on Advanced Intelligent Mechatronics (AIM)*. IEEE, 2019.